UNIVERSITEIT VAN PRETORIA
UNIVERSITY OF PRETORIA
YUNIBESITHI YA PRETORIA

Utilizing zero-valent iron for the remediation of sulfate-rich mine water

by

Philip Venter

Submitted in fulfilment of the requirements for the degree

M.Sc. Soil Science

In the Faculty of Natural & Agricultural Sciences

University of Pretoria

Pretoria

November 2022

© University of Pretoria

DECLARATION

I, Philip Venter, declare that the dissertation, which I hereby submit for the degree MSc. Soil Science at the University of Pretoria, is my own work and has not previously been submitted by me for a degree at this or any other tertiary institution.

SIGNATURE:

28/11/2022

DEDICATION

This master's dissertation is dedicated to my family, Philip Venter Snr., Marleyne Venter, Mauritz Venter and Derrick Venter. I give my deepest expression of appreciation for their encouragement and unweathering faith, and the sacrifices they made during my post graduate studies. Thank you for the support and company during the writing of this dissertation.

ACKNOWLEDGEMENTS

The generous financial assistance of the University of Pretoria is hereby acknowledged. I would also like to extend my thanks to Dr. Johan van der Waals and TerraSoil for the equipment that contributed to my study.

A warm and heartfelt thank you to the following people who helped me see this study to fruition:

My supervisor, Mr. P.C. de Jager, for his endless wisdom and guidance throughout my study. Thank you for your meticulous attention to detail and all your encouragement and support.

Dr. Johan van der Waals for his valuable advice and input as well as introducing me to the multi-disciplined metal called iron.

Professor John Annandale for welcoming me to the University of Pretoria.

Jeanette Dykstra and Wiebke Grote for the expertise in XRD and XRF respectively from the Geology department at UP.

The technical staff at the laboratory in the Department of Plant and Soil Science.

The academic staff at the Department of Plant and Soil Science for their support and guidance.

The departmental secretaries for their willingness to help with all administrative aspects of the project.

SUMMARY

Coal and gold mining in South Africa generates sulfate-rich mine water, where Ca and Mg are the dominant cations. Gypsum solubility controls Ca concentration and, to a certain degree, sulfate. Mg solubility is not controlled through precipitation and owing to charge balance principles, if Mg is high, sulfate will be high. Thus, to increase the quality of the mine water S, Ca and Mg must be removed. Various treatment options for the management of mine water exist, however, the passive treatment utilizing zero-valent iron (ZVI) was investigated. The aim was to determine if ZVI can be used to increase mine water quality.

To investigate this, sulfate solutions with concentrations of 300 mg l^{-1} (3.12 *mM*) and 1200 mg l^{-1} (12.5 *mM*) were prepared as a) $CaSO_4$ solution, b) $MgSO_4$ solution and, c) Ca-$MgSO_4$ solution. These solutions represent typical concentrations of coal mine water chosen for this study. Solutions were further divided into sub-samples (40 ml) and adjusted to a pH of 4 and 8. ZVI (1 g) was added to each sample and dissolved oxygen was purged from the samples using argon gas. Batch sorption experiments were conducted over a period of 145 days, where samples were collected and analysed after days 1, 20, 120 and 145. The concentrations of Fe, Ca, Mg and S were analysed with ICP-AES. Dissolved Fe^{2+} was measured using the 1,10-phenanthroline colorimetric method. Dissolved Fe^{3+} was calculated as the difference between total dissolved Fe and dissolved Fe^{2+}. The pH and EC for each sample was measured, as well.

Fisher's LSD tests showed that S, Ca and Mg in solution, in contact with ZVI, decreased significantly over time. The initially alkaline $CaSO_4$ solution, at 12.5 *mM* (ALK_$CaSO_4$), showed the greatest decrease of S (19.58 mmol kg^{-1} ZVI) and Ca (17.87 mmol kg^{-1} ZVI). Followed by the initially acidic Ca-$MgSO_4$ solution, at 12.5 *mM* (AC_Ca-$MgSO_4$), for S (15.37 mmol kg^{-1} ZVI), Ca (5.93 mmol kg^{-1} ZVI) and Mg (10.68 mmol kg^{-1} ZVI). Lastly, the initially acidic $MgSO_4$ solution, at 12.5 *mM* (AC_$MgSO_4$), showed the third greatest decrease in S (14.57 mmol kg^{-1} ZVI) and Mg (14.76 mmol kg^{-1} ZVI), where the highest removal of Mg occurred.

Oxidation of Fe^0 to surface Fe^{2+} was enhanced by the increased SO_4^{2-} concentration. The combination of Ca and Mg in solution, initially acidic, produced the highest concentration of dissolved Fe. Solutions containing Mg also showed lower ratios of Fe^{3+}/Fe_{Tot} compared to the $CaSO_4$ solutions. Selected XRD analyses showed that in 145 days pyrite, along with goethite and magnetite precipitated on the ZVI's surface in both the $CaSO_4$ and Ca-$MgSO_4$ solution. For the $MgSO_4$ solution, however, only pyrite was detected.

Practical simulations indicated that removing 20% S, Ca and Mg in 1 m^3 of water, in 20 days, from the Ca-$MgSO_4$ solutions required more ZVI, compared to 145 days. ZVI also showed efficacy over the long term. Allowing longer reaction time with simulated mine water (e.g., 145 day) resulted in less ZVI needed per m^3 of water.

TABLE OF CONTENTS

DECLARATION i
DEDICATION ii
ACKNOWLEDGEMENTS iii
SUMMARY iv
TABLE OF CONTENTS vi
LIST OF FIGURES ix
LIST OF TABLES xiii
CHAPTER 1: GENERAL INTRODUCTION 1
CHAPTER 2: LITERATURE REVIEW 4
2.1 Introduction 4
2.2 Sulfate 4
2.2.1 Sulfate in the Olifants River catchment 4
2.2.2 Options for sulfate removal 5
2.2.3 Conditions for sulfate reduction 6
2.3 Calcium and magnesium 7
2.3.1 Calcium and magnesium in the Olifants River catchment 7
2.3.2 Options for calcium and magnesium removal 7
2.3.3 Conditions for calcium and magnesium removal 9
2.4 Zero-valent iron (ZVI) 10
2.4.1 ZVI: Basic fundamentals of iron 10
2.4.2 ZVI: Challenges and possibilities 11
2.4.3 ZVI: Physico-chemical characteristics of nano ZVI (nZVI), micro ZVI (mZVI) and granular ZVI (gZVI) 14
2.4.4 ZVI: Fe^0 corrosion and iron (oxy)hydroxide formation 15
2.4.5 ZVI: Contaminant sequestration by an Fe^0/Fe-oxide/H_2O system 18
2.4.6 ZVI: Sulfate and ZVI 19
2.5 Approach in selecting sulfate concentrations and pH values for the experimental section 21
2.5.1 Selecting River monitoring points 21
2.5.2 Selecting sulfate concentrations 22
2.5.3 Selecting pH values 23

CHAPTER 3: PURGING DISSOLVED OXYGEN (DO) 24
3.1 Introduction 24
3.2 The process of degassing a solution 24
3.3 Materials and Methodology 26
3.3.1 Purging material, reagents and measuring equipment 26
3.3.2 Purging dissolved oxygen (DO) 27
3.4 Results and Discussion 28
3.4.1 Dissolved oxygen (DO) in solution before purging 28
3.4.2 Dissolved oxygen (DO) after purging 30
3.3.3 Redox potential, pH and EC of solutions before and after purging 31
3.5 Conclusion 32
CHAPTER 4: EVOLUTION OF mZVI REDOX POTENTIALS IN ACIDIC AND ALKALINE SOLUTIONS 34
4.1 Introduction 34
4.2 Materials and Methodology 34
4.2.1 Reagents 34
4.2.2 Preparation of acidic (pH = 4) and alkaline (pH = 8) sulfate solutions 34
4.3 Results and Discussion 36
4.3.1 Redox potential changes of mZVI-de-ionized water systems 36
4.3.2 Redox potential changes of ZVI-sulfate systems 39
4.3.3 Statistical inference of the effect of purging on redox potentials 44
4.3.4 Statistical inference of the effect of initial acidity and alkalinity on redox potentials 45
4.3.5 The effect of Ca^{2+}, Mg^{2+} and SO_4^{2-} in sulfate solutions on redox potentials 46
4.4 Conclusion 47
CHAPTER 5: SULFATE, CALCIUM AND MAGNESIUM REMOVAL BY MICRO ZERO-VALENT IRON 48
5.1 Introduction 48
5.2 Materials and Methodology 48
5.2.1 The batch sorption procedure 48
5.2.2 Colorometric determination of Fe(II) 51
5.2.3 Calculating the chemical equilibria of solutions 51
5.2.4 X-ray powder diffraction (XRD) on selected mZVI samples after mZVI sorption 51
5.3 Results and Discussion 52

5.3.1 Changes in aqueous sulfur, calcium and magnesium over time 52
5.3.1.1 The $CaSO_4$ solution at 3.12 mM 52
5.3.1.2 The $CaSO_4$ solution at 12.5 mM 60
5.3.1.3 The $MgSO_4$ solution at 3.12 mM 67
5.3.1.4 The $MgSO_4$ solution at 12.5 mM 74
5.3.1.5 The Ca-$MgSO_4$ solution at 12.5 mM 81
5.4 Conclusion 88
CHAPTER 6: SYNTHESIS 90
6.1 Summary 90
6.2 Practical Simulation 94
6.3 Conclusions and Recommendations 96
REFERENCES 97
APPENDIX A: SUPPLEMENTARY DATA FOR CHAPTER 3 108
APPENDIX B: SUPPLEMENTARY DATA FOR CHAPTER 4 113
APPENDIX C: SUPPLEMENTARY DATA FOR CHAPTER 5 118
APPENDIX D: DATA FROM PHREEQCi FOR CHAPTER 5 122

LIST OF FIGURES

Figure 2.1: Simplified illustration of a) ZVI and b) the basic crystal structure of ZVI (Guan et al, 2015) 11
Figure 2.2: Simplified Fe^0/Fe(II)/(III)-oxide/H_2O system adapted from Noubactep, (2015) 17
Figure 2.3: Simplified illustration of the corrosion of a ZVI particle submersed in solution (Guan et al., 2015) 19
Figure 2.4: Locality of selected river monitoring points: 1997 – 2012 (DWS, 2013 & Google Earth) 21
Figure 2.5: Histogram of sulfate concentration levels from borehole data of selected river monitoring points: 1997-2012 (DWS, 2013) 22
Figure 2.6: Histogram of pH ranges from borehole data of selected river monitoring points: 1997-2012 (DWS, 2013) 23
Figure 3.1: Simplified representation of argon purging oxygen 25
Figure 4.1: Experimental design for the $CaSO_4$, $MgSO_4$ and Ca-$MgSO_4$ solutions 36
Figure 4.2: The change in redox potentials for the ZVI-DW systems 39
Figure 4.3: The change in redox potentials for $CaSO_4$-ZVI systems 42
Figure 4.4: The change in redox potentials for ZVI-$MgSO_4$ systems 43
Figure 4.5: The change in reduction potentials of ZVI-Ca-$MgSO_4$ systems 44
Figure 5.1: Experimental design illustrating the sulfate solutions with their controls and the experiments carried out 50
Figure 5.2: Decrease in aqueous S & Ca in the (a) ac_$CaSO_4$ and (b) alk_$CaSO_4$ solutions. The least significant difference of S & Ca for (a) are 0.03 & 0.02 and for (b) are 0.02 & 0.03 at a confidence level of 95% (α = 0.05) 53
Figure 5.3: The redox and pH data, (green and red points represent data of day 1, 20, 120 & 145), of the ac_$CaSO_4$ and alk_$CaSO_4$ superimposed on a E_h-pH (Pourbaix) diagram for the Fe-Ca-S system 54
Figure 5.4: Correlation of S and Ca sorption as a function of (a) pH and (b) redox potential for the ac_$CaSO_4$ solution 56

Figure 5.5: Correlation between S and Ca sorption for the ac_$CaSO_4$ and alk_$CaSO_4$ solution 57
Figure 5.6: Correlation of S and Ca sorption as a function of (a) pH (b) redox potential for the alk_$CaSO_4$ solution 58
Figure 5.7: Sorption of S or Ca vs dissolved Fe^{2+} and Fe^{3+} for the (a) ac_$CaSO_4$ and (b) alk_$CaSO_4$ solution 60
Figure 5.8: Decrease in aqueous S & Ca in the (a) AC_$CaSO_4$ and (b) ALK_$CaSO_4$ solutions. The least significant difference of S & Ca for (a) are 0.04 & 0.02 and in (b) are 0.03 & 0.04 at a confidence level of 95% (α = 0.05) 61
Figure 5.9: The redox and pH data, (green and red points represent data for day 1, 20, 120 & 145), of the AC_$CaSO_4$ and ALK_$CaSO_4$ superimposed on a E_h-pH (Pourbaix) diagram for the Fe-Ca-S system 62
Figure 5.10: Correlation of S and Ca sorption as a function of (a) pH and (b) redox potential for the AC_$CaSO_4$ solution 63
Figure 5.11: Correlation between S and Ca sorption for the AC_$CaSO_4$ and ALK_$CaSO_4$ solutions 63
Figure 5.12: XRD of mZVI powder, taken from the ALK_$CaSO_4$ solution after 145 days 64
Figure 5.13: Correlation of S and Ca sorption as a function of (a) pH and (b) redox potential for the ALK_$CaSO_4$ solution 65
Figure 5.14: Sorption of S & Ca vs dissolved Fe^{2+} and Fe^{3+} for the (a) AC_$CaSO_4$ and (b) ALK_$CaSO_4$ solution 67
Figure 5.15: Change in aqueous S & Mg in the (a) ac_$MgSO_4$ and (b) alk_$MgSO_4$ solutions. The least significant difference of S & Mg for (a) are 0.02 & 0.004 and in (b) are 0.008 & 0.02 at a confidence level of 95% (α = 0.05) 68
Figure 5.16: The redox and pH data, (green and red points represent data for day 1, 20, 120 & 145), of the ac_$MgSO_4$ and alk_$MgSO_4$ superimposed on a E_h-pH (Pourbaix) diagram for the Fe-Mg-S system 69
Figure 5.17: Correlation of S and Mg sorption as a function of (a) pH and (b) redox potential for the ac_$MgSO_4$ solution 71

Figure 5.18: Correlation between S and Mg sorption for the ac_$MgSO_4$ and alk_$MgSO_4$ solutions 71
Figure 5.19: Correlation of S and Mg sorption as a function of (a) pH and (b) redox potential for the alk_$MgSO_4$ solution 72
Figure 5.20: Sorption of S & Mg vs dissolved Fe^{2+} and Fe^{3+} for the (a) ac_$MgSO_4$ and (b) alk_$MgSO_4$ solution 74
Figure 5.21: Change in aqueous S & Mg in the (a) AC_$MgSO_4$ and (b) ALK_$MgSO_4$ solutions. The least significant difference of S & Mg for (a) are 0.02 & 0.04 and in (b) are 0.04 & 0.04 at a confidence level of 95% (α = 0.05) 74
Figure 5.22: The redox and pH data, (green and red points represent data for day 1, 20, 120 & 145), of the AC_$MgSO_4$ and ALK_$MgSO_4$ superimposed on a E_h-pH (Pourbaix) diagram for the Fe-Mg-S system 76
Figure 5.23: Correlation between S and Mg sorption for the AC_$MgSO_4$ and ALK_$MgSO_4$ solutions 76
Figure 5.24: XRD of mZVI powder, taken from the AC_$MgSO_4$ solution after 145 days 77
Figure 5.25: Correlation of S and Mg sorption as a function of (a) pH and (b) redox potential for the AC_$MgSO_4$ solution 78
Figure 5.26: Correlation of S and Mg sorption as a function of (a) pH and (b) redox potential for the ALK_$MgSO_4$ solution 79
Figure 5.27: Sorption of S & Mg vs dissolved Fe^{2+} and Fe^{3+} for the (a) AC_$MgSO_4$ and (b) ALK_$MgSO_4$ solution 81
Figure 5.28: Change in aqueous S, Ca & Mg in the AC_Ca-$MgSO_4$ solutions. The least significant difference of S, Ca & Mg for (a) are 0.02, 0.02 & 0.02 and for (b) are 0.04, 0.003 & 0.004 at a confidence level of 95% (α = 0.05) 82
Figure 5.29: The redox and pH data, (green and red points represent data for day 1, 20, 120 & 145), of the AC_Ca-$MgSO_4$ and ALK_Ca-$MgSO_4$ superimposed on a E_h-pH (Pourbaix) diagram for the Fe-Ca-Mg-S system 84
Figure 5.30: Correlation of S, Ca and Mg sorption as a function of (a) pH and (b) redox potential for the AC_Ca-$MgSO_4$ solution 84
Figure 5.31: The correlation between S, Ca and Mg sorption for the AC_Ca-$MgSO_4$ and ALK_Ca-$MgSO_4$ solutions 85

Figure 5.32: Correlation of S, Ca and Mg sorption as a function of (a) pH and (b) redox potential for the ALK_Ca-$MgSO_4$ solution 86
Figure 5.33: Sorption of S, Ca & Mg vs dissolved Fe^{2+} in solution of the (a) AC_Ca-$MgSO_4$ and (b) ALK_Ca-$MgSO_4$ solution..... 87
Figure 5.34: XRD of mZVI powder, taken from the AC_Ca-$MgSO_4$ solution after 145 days 88

LIST OF TABLES

Table 2.1: Basic properties of the chemical element iron (Chang, 2008) 10
Table 2.2: The progress of ZVI technology according to Guan et al., (2015) 12
Table 2.3: Physical properties of nZVI, mZVI & gZVI (Velimirovic et al., 2014) 15
Table 3.1: Purging equipment 26
Table 3.2: The influence of the various solutions on $O_{2(g)}$ solubility (in µM) 29
Table 3.3: Effect of Ar purging on DO concentrations of solutions (in *µM*) 30
Table 3.4: The influence of Ar purging on the redox potential of DW and sulfate solutions 31
Table 3.5: The influence of Ar purging on the pH and EC of DW and sulfate solutions 32
Table 4.1: Redox potentials of acidic & alkaline FeDWs 37
Table 4.2: Redox potentials of sulfate solutions 41
Table 4.3: Significance of differences in redox potentials between unpurged and purged sulfate solutions[a] 45
Table 4.4: Significance of differences in redox potentials between acidic and alkaline sulfate solutions[a] 46
Table 4.5: Significance of differences in redox potentials between samples containing Ca^{2+} and/or Mg^{2+}, after 16 days[a] 46
Table 5.1: Sorption of S and Ca for the 3.12 *mM* $CaSO_4$ solutions 53
Table 5.2: Dissolved Fe in the 3.12 *mM* $CaSO_4$ solutions 59
Table 5.3: Sorption of S and Ca for the 12.5 *mM* $CaSO_4$ solutions 61
Table 5.4: Dissolved Fe in the 12.5 *mM* $CaSO_4$ solutions 66
Table 5.5: Sorption of S and Mg for the 3.12 *mM* $MgSO_4$ solutions 68
Table 5.6: Dissolved Fe in the 3.12 *mM* $MgSO_4$ solutions 73
Table 5.7: Sorption of S and Mg for the 12.5 *mM* $MgSO_4$ solutions 75
Table 5.8: Dissolved Fe in the 12.5 *mM* $MgSO_4$ solutions 80
Table 5.9: Sorption of S, Ca and Mg for the 12.5 *mM* Ca-$MgSO_4$ solutions 82
Table 5.10: Dissolved Fe in the 12.5 *mM* Ca-$MgSO_4$ solutions 87
Table 6.1: Sorption behaviour of S, Ca, and Mg in the different solutions investigated 93
Table 6.2: Zero-valent iron (tonnes m^{-3}) required to remove S, Ca, and Mg per m^{-3} 95

CHAPTER 1: GENERAL INTRODUCTION

Mining coal and metal is important for the economic growth of South Africa, creating jobs as well as generating the country's electricity, however, their mining generates sulfate-rich saline mine water. In South Africa 70% of the coal reserves are hosted by the Waterberg, Highveld and Witbank coalfields (Jeffrey, 2005) where the Highveld and Witbank coalfields are both located in Mpumalanga, translating to intensive mining concentrated in small areas. The problem at hand is water of high salinity is produced from mining in these coalfields which is discharged into water bodies such as the Vaal River, Olifants River and Crocodile River. One of the constituents that, at times, exceed levels that are toxic to the fauna and flora inhabiting these water bodies is dissolved sulfate (Mkwelo & de Villiers, 2009). According to van Zyl et al. (2001) mine water from Kriel Colliery discharging into the Upper Olifants River catchment contained concentrations in the range of 800 - 3000 mg l^{-1} sulfate. These sulfate levels exceed the domestic (<200 mg l^{-1} SO_4^{2-}) and industrial (500 - 600 mg l^{-1} SO_4^{2-}) safety regulatory levels (McCarthy & Pretorius, 2009; van Zyl et al., 2001; WHO, 2004b). Lancaster & Candy (2012) reported that the dominant cations observed were Ca, Mg & Na and to a lesser extent K, Fe, Al & Mn. Fe, Al & Mn are a concern in acid mine water but was not in the focus of this study.

It is therefore clear that overall water quality needs to be improved by removing dissolved constituents, consequently reducing the salinity in mine water. Various utilization, containment and treatment options have been proposed and researched in the management of mine water such as; 1) beneficiation of mine water where Annandale et al. (2006) discussed that gypsiferous mine water from the coalfields can be used for irrigation; 2) prevention of acid mine drainage from exposed sediment and gange material reacting with groundwater or surface water through diversions or permeable wall reactors; 3) containment of mine waste through capping or covering mine tailings with vegetation and 4) mine water treatment through active mine treatment (reverse osmosis or the application of bactericides) or passive mine treatment (Coleman et al., 2011).

Passive mine treatment was described by Coleman et al. (2011) as engineered treatment amenities requiring little to no maintenance after their construction and activation. Such an amenity can be created to remove contaminants from saline mine water by incorporating zero-valent iron (ZVI). ZVI can remove elements that precipitate with Fe(0), Fe(II) and/or Fe(III) and Karri et al., (2005) stated that ZVI (Fe^{II}/Fe^{0}, E^{0} = -0.414 V) can reduce SO_4^{2-} (S^{VI}/S^{II-}, E^{0} = -0.245 V) and precipitate S^{2-}. ZVI is also readily available and requires minimal maintenance.

Zero-valent iron in acidic conditions is capable of removing sulfate but in neutral water contaminant removal becomes restricted. The aim of this study is to investigate the viability of using ZVI in improving water quality of saline mine water that is not acidic. Zero-valent iron reduces inorganic material and is used for groundwater remediation in permeable reactive barriers (PRB), and as reactors to remove heavy metals and organic pollutants (Guan et al., 2015). However, there is a knowledge gap regarding ZVI reduction capabilities and sulfate removal, and the role of alkali and alkaline earth metals which are usually the dominant cations in waters which are not extremely acid.

The expectation is that this study will shed light on above-mentioned and the impact of gradual pacification on the Fe^{0} surfaces on their chemical reactivity when oxidation of ZVI (the formation of rust) which limits its ability to reduce (and remove) sulfate. The results can also shed light on the sensitivity of the ZVI surfaces to oxidation as this will influence the practical use of ZVI in treating mine water systems by; obscuring reaction mechanisms of ZVI oxidation and sulfate reduction as well as the influence of Ca and Mg in sulfate-rich water on ZVI's reactivity, oxidation rate and sulfate sorption and reduction.

The hypothesis of this study is that ZVI will reduce SO_4^{2-} to S^{2-} in saline solutions until Fe^{0}'s surface is completely covered by ferrous/ferric oxy(hydroxides) and FeS_2. It is further hypothesized that the cation composition of the mine water will play a crucial role as Mg^{2+} and Ca^{2+}, for example, might have antagonistic and/or synergistic effects on sulfate reduction.

The objectives of this study are to; Evaluate the reduction potential of ZVI in acidic and alkaline saline solutions over time; Gain insight into the sorption and reduction of sulfate on ZVI surfaces and; Understand and quantify the impact that calcium and magnesium ions in saline water will have on above mentioned capacity and determine the extent of co-sorption of these cations during sulfate sorption and reduction.

Chapter 1 is the general introduction and provides a background to the study. Chapter 2 is the literature review. The third chapter investigates the effectiveness of the experimental set-up in removing dissolved oxygen from saline solutions, as well as the need of DO removal in order to create sufficiently reduced conditions for Chapter 4. Chapter 4 evaluates the reduction potentials induced by ZVI in acidic and alkaline saline solutions, when DO is initially purged from solution with Ar compared to experimental conditions where this did not occur. Chapter 5 investigates the interaction between Fe^0, SO_4^{2-}, Ca^{2+} & Mg^{2+} in acidic and alkaline ZVI-saline systems in order to quantify sulfate, Ca and Mg removal. Chapter 5 is the main working chapter. The last chapter is a summation of the study followed by references. Appendix A to D provides supplementary data for the relevant chapters.

CHAPTER 2: LITERATURE REVIEW

2.1 Introduction

Sulfate is the major anion reported in saline mine water (Jansen & Lancaster, 2012; Lancaster & Candy, 2012) when pyrite (FeS_2), the most common sulfide bearing mineral, is exposed to water and oxygen, oxidizing sulfide to sulfate (S^{-1}/S^{6+}) presented by the reaction in Equation 2.1 (Akcil & Koldas, 2006);

$$FeS_{2(s)} + 3O_{2(g)} + 2H_2O_{(l)} \leftrightarrows Fe^{2+}_{(aq)} + 2SO_4^{2-}{}_{(aq)} + 4H^+_{(aq)} \quad (2.1)$$

Equation 2.1 shows that for every 1 mole of sulphite (S^{-1}) oxidized (from the mineral pyrite) 1 mole of sulfate (S^{6+}) is produced and discharged into rivers annually leading to sulfate -rich water. The major cations calcium, magnesium and sodium (sodium not being in the focus of this study) are generally associated with the sulfate-rich mine water, from acidic to alkaline, and is in far higher concentrations than any other cation present (DWS, 2013) due to the homogenous geology that the mines and rivers share (Johnson et al., 1996; van Zyl et al., 2001).

2.2 Sulfate

2.2.1 Sulfate in the Olifants River catchment

The majority of Gauteng and Mpumalanga's principal metropolitan areas are situated on the watersheds of river catchments. The rivers that drain away from these watersheds provide drinking water, water for irrigation and water for transporting sewerage and mine waste. Bowell (2004) stated that discharging mine water into public rivers and streams is legally permissible if the sulfate concentration is below 600 mg l^{-1} but as the rivers flow downstream to water storage reservoirs, these reservoirs are annually enriched with saline mine water high in dissolved salt concentrations (that contain sulfate), deteriorating these storage reservoirs as well as the rivers (Oberholster & Ashton, 2008).

Biggs et al. (2017) reported the Olifants River as the most deteriorated river in South Africa, with a strong sulfate signature mainly in the Upper Olifants River and was

determined by evaluating its dissolved salt levels, which is also an indicator for salinity (Mhlongo et al., 2018). The Olifants River originates between Bethal and Breyten, Mpumalanga and flows north through the Witbank Dam (Upper Olifants River catchment) and then through the Loskop Dam (Middle Olifants River catchment) ultimately joining the Limpopo River that flows out in Xai Xai, Mozambique. This means that the sulfate levels, that increase downstream, has far reaching effects as it is transported by the Olifants River and the majority of mining activities such as coal mining occurs in the Upper Olifants River catchment (Mkwelo & de Villiers, 2009).

McCarthy & Pretorius (2009); van Zyl et al. (2001) reported sulfate concentrations from the Middelburg Dam and Witbank Dam, located in the Upper Olifants River catchment, as 1524 mg l^{-1} and 1645 mg l^{-1} respectively. A monitoring station in Wolwekrans, also in the Upper Olifants river catchment, reported sulfate concentrations of 1500 mg l^{-1} and more as the Upper Olifants River catchment contains the most mining activities with coal mines being the major threat. van Zyl et al. (2001) also presented data stating that the water quality of the Olifants River was far more deteriorated than the Vaal River, but it was further reported that the Vaal River was following the same trend as the Olifants River in the degradation of its water quality.

Although various successful methods of mine rehabilitation have been implemented, previously discussed in Chapter 1, sulfate removal from mine water is less understood, with fewer case studies, than metal and acid toxicity as it was considered not as important. There is, however, an ever-growing necessity to specifically lower the salinity observed in the Olifants River or any other river or tributary (Bowell, 2004; McCarthy & Pretorius, 2009; van Zyl et al., 2001) as the focus on sulfate only in literature is partly flawed and skewing chemical insight.

2.2.2 Options for sulfate removal

Chapter 1 briefly mentioned methods in treating sulfate in mine water but Bowell, (2004) reviewed various methods to increase mine water quality. The options included; 1) Membrane removal through reverse osmosis, electrical dialysis or filtration; 2)

Precipitation and removal of sulfate, and other ions, through ion-exchange resins or chemical saturation and sulfate precipitation by adding lime or barium carbonate; and 3) Biological sulfate reduction achieved through permeable reactive barriers (PRBs) and constructed bioreactors or wetlands.

Option 1 has the advantage of producing clean drinking water but the scale of a reverse osmosis plant, for instance, increased with increasing sulfate concentration that leads to exponential costs. Another drawback was the short membrane life as sulfate quickly corrodes the membrane wall and frequent maintenance was required. A combination of options 1 and 2 are commonly used together with option 2 as a pre-cleaning step before option 1, in order to extend the membranes lifetime. Option 2 is the most cost effective and required little maintenance, but the production of sludge was high. Biological sulfate reduction (option 3) is the most adaptable and widely applicable approach to remove sulfate (Bowell, 2004) but this option also produced sludge, had a limited life span and the long-term performance of PRBs are unknown.

2.2.3 Conditions for sulfate reduction

Essington (2004) presented a reduction sequence for species in pH 6.5 to 7 soil, where SO_4^{2-} (S^{6+}) is reduced to H_2S (S^{2-}) at a pe below -2 (-120 mV) and Kadlec & Wallace (2009) discussed wetlands in treating contaminants and also stated that SO_4^{2-} (S^{6+}) was reduced to H_2S (S^{2-}) in highly reduced, anoxic environments at reduction potentials between -100 mV to -200 mV ($-1.71 > pe > -3.43$). Among the important electron donors or reductants recognized in wetlands are organic matter and ferrous iron (Fe^{2+}). Organic matter reduces sulfate, as sulfate reducing bacteria (SRB) oxidizes organic carbon (electron donor) into bicarbonate (C^{4+}) that reduces sulfate (electron acceptor) (DeLuane & Reddy, 2005; Zagury et al., 2006).

DeLuane & Reddy (2005) stated that ferrous iron (Fe^{2+}) is a critical component in reducing sulfate, where Fe^{2+} is the electron donor and sulfate is the electron acceptor. Low redox potential (E_h) conditions can be created by zero-valent iron (ZVI). Liu et al. (2015) stated that ZVI is a reducing agent, inducing and enhancing anoxic environments, but did not

report on the oxidation-reduction potential (ORP) values (most ZVI orientated journals do not report measured ORP values). Fortunately, in a study conducted by Waclawek et al. (2015) micro-ZVI (mZVI) produced ORP values between -200 mV and -450 mV (-3.43 > pe > -7.72), between fluctuating pH values of 6 and 9, measured over 25 days.

Magnetite is also reportedly found on ZVI's surface and studies conducted by Mansour et al. (2009) explained that sulfate was not reduced but only adsorbed onto magnetite as neutral monodentate outer-sphere complexes at a pH range of 5 - 6.1, and at pH below 5, sulfate was adsorbed as neutral bidentate inner-sphere complexes.

2.3 Calcium and magnesium

2.3.1 Calcium and magnesium in the Olifants River catchment

Calcium, magnesium and, to a lesser extent, sodium (sodium not in the scope of this study) are the major cations that predominantly form soluble salts of calcium sulfate and magnesium sulfate (Ströhmenger, 2001). Ströhmenger (2001) reported that the mine water from the Kleinkopje Colliery contained calcium concentrations of 707.41 mg l^{-1} (17.65) *mM* and magnesium concentrations of 392.85 mg l^{-1} (16.16 *mM*). The Kleinkopje Colliery is located on the Upper Olifants River, Mpumalanga and daily generates 14 Ml of saline mine water that is discharged into the Olifants River.

Selected river monitoring points from 1997 – 2012 (DWS, 2013) also reported calcium and magnesium concentrations up to 738.67 mg l^{-1} (18.43 *mM*) and 748.51 mg l^{-1} (30.79 *mM*) respectively. Higher concentrations of Ca^{2+} and Mg^{2+} decrease the ion activity of other nutrient ions and disrupt translocation of other nutrient ions through competition (Ströhmenger, 2001). Furthermore, if magnesium is at higher concentrations than calcium, magnesium will also cause a Ca^{2+} deficiency in the system.

2.3.2 Options for calcium and magnesium removal

A study by Pelser (2003) explained that calcium and magnesium toxicity, just as sulfate toxicity, is not as environmentally dangerous as the acidity and metal toxicity produced from mine-effluent, but their contribution will be to salinity. Options for removing calcium

and magnesium concentrations, in sulfate-rich mine water, comes down to three methods proposed by Pelser, (2003) that include; 1) Precipitation of calcium and magnesium; 2) Ion exchange; and 3) Solvent extraction of calcium and magnesium.

The first method is the most practically used option and removing calcium and magnesium by precipitating with fluoride is ideal as fluoride has a high selectivity for calcium and magnesium, forming an environmentally stable product. Fluoride, however, should not be directly added to soil as this will lead to fluoride dissolving clay minerals in said soil due to its strong complexation properties. Precipitation with fluoride has drawbacks however, such as gel formation in solution, unwanted cations reacting with fluoride and fluoride is still potentially dangerous, if it exceeds 1.5 mg l^{-1} in solution, and needs to be removed after precipitation (WHO, 2004a).

The addition of lime ($Ca(OH)_2$) to a solution leads to the precipitation of calcium sulfate and also magnesium hydroxide but only under conditions discussed in section 2.3.3. The option of adding lime is highly selective to calcium and there was no need for additional chemicals, however magnesium cannot be controlled as much as calcium and the process requires a residence time of more than 6 hours (Pelser, 2003).

The second method involved the removal or control of calcium and magnesium by ion exchange with macroreticular cation resins bonded to styrene or divinylbenzene. Although the method is highly selective of calcium and magnesium, transition metals are selectively preferred by the resin above calcium and magnesium.

The third method involved solvent extraction of calcium and magnesium whereby common extractants such as di-(2-ethylhexyl)phosphoric acid (D2EHPA), which is an organophosphorus compound with the formula ($(C_8H_{17}O)_2PO_2H$), or purified 2-ethylexyl hydrogen 2-ethylhexyl phosphonate (PC 88A) are used to extract calcium and magnesium. This method however requires additional reaction steps to remove calcium and magnesium, is limited by gypsum solubility and different extractants are needed for calcium and magnesium respectively.

2.3.3 Conditions for calcium and magnesium removal

Although section 2.3.2 stated that precipitation of calcium and magnesium was the most common and favoured control method, Pelser (2003) did not specifically look at the conditions required to precipitate and remove calcium and magnesium. Calcium sulfate precipitates in solution above 2100 mg l^{-1} at 25 ºC and the addition of lime leads to the precipitation of gypsum ($CaSO_4.2H_2O$) at cooler temperatures (>20 ºC) and anhydrite ($CaSO_4$) at warmer temperatures (>100 ºC) irrespective of pH. Dou et al. (2017), however, stated that with a pH value above 11, absence of magnesium and presence of aluminium, and a calcium-to-sulfate ratio of 3:2, ettringite ($Ca_6Al_2(SO_4)_3(OH)_{12}\cdot 26H_2O$) can precipitate in solution.

In a study conducted by Ineich et al. (2017) it was determined that brucite ($Mg(OH)_2$) precipitated above a pH of 10 and further explained that the precipitation of brucite is only possible if magnesium concentrations in solution exceeded 200 mg l^{-1} (4.86 *mM*). It is obvious that precipitating and removing magnesium is more complicated than calcium and relies on a solution of high alkalinity and magnesium can only precipitate above the 200 mg l^{-1} concentration meaning that below this concentration removal of magnesium is not possible and new methods need to be investigated.

2.4 Zero-valent iron (ZVI)

2.4.1 ZVI: Basic fundamentals of iron

Zero-valent iron (ZVI) or elemental iron (Fe^0) has a valence state of zero and is a transition metal with the symbol Fe, derived from the Latin name *ferrum* (Chang, 2008). It is dense metal that commonly forms non-stoichiometric compounds referred to as berthollides (Xie, 1994). Table 2.1 lists the basic fundamental properties of iron (ZVI).

Table 2.1: Basic properties of the chemical element iron (Chang, 2008)

Chemical symbol	Fe
Atomic number	26
Atomic mass	55.85 u
Atomic radius	0.126 nm
Electrons per shell	2, 8, 14, 2
Electron configuration	[Ar] $3d^6 4s^2$
Melting point	1535 °C
Boiling point	2750 °C
Ionization energy	759 kJ/mol
Electronegativity	1.8 (Pauling scale)
Common oxidation states	+2, +3 (-2 to +7)[a]
Density	7.874 g/cm^3 (6.98)[b]

a = Iron has oxidation states of -2 to +7 but the oxidation states +2 & +3 are the most common in nature.

b = When in liquid form.

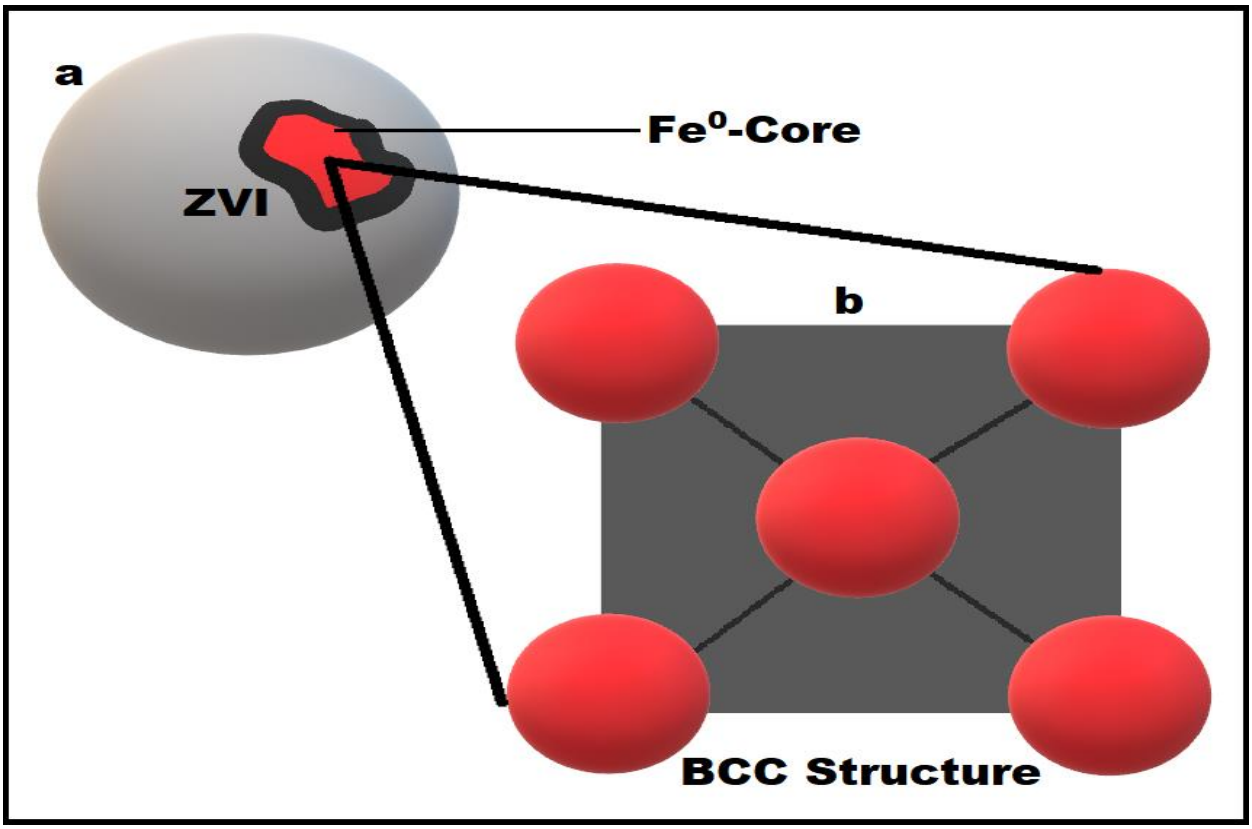

Figure 2.1: Simplified illustration of a) ZVI and b) the basic crystal structure of ZVI (Guan et al, 2015)

Figure 2.1 is a simplified illustration depicting ZVI. Within the Fe^0-core, Fe atoms are densely packed in a body centred cubic (BCC) crystal structure with an iron unit cell length of 0.287 nm (Brog et al., 2013).

2.4.2 ZVI: Challenges and possibilities

Removal of organic and inorganic material using zero-valent metals has been studied in detail prior to 1990. However, only from 1994 and onwards had it been physically implemented in the field (Guan et al., 2015). First reported uses of ZVI was in field trials within PRBs for the remediation of groundwater contaminated by pentachloroethylene (PCE) and trichloroethylene (TCE) at a Canadian Air Force Base in 1991 (Guan et al., 2015). Karri et al. (2005) stated that ZVI was a common reactive tool used in PRBs and due to its success, ZVI has gained much attention over the last two decades presented in Table 2.2.

Table 2.2: The progress of ZVI technology according to Guan et al., (2015)

1994
Publication of two papers on ZVI degrading halogenated aliphatics
Acid washing pre-treatment for pristine ZVI
First full scale ZVI-PRB reactor installed
1996
Incorporating nZVI in groundwater remediation
1998
Ultrasound pre-treatment for pristine ZVI
Exploration of ZVI bimetals
Coupling ZVI with zeolites
2000
First field demonstration of groundwater remediated with nZVI
2002
ZVI-PRB designated as a standard remediation technology by USEPA
2004
Coupling ZVI with activated carbon or bentonite
H_2 pre-treatment of pristine ZVI
2008
ZVI assisted with UV light technology
2010
Microwave assisted ZVI technology
Coupling ZVI with iron oxides
2014
Future possibilities of ZVI remediation

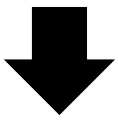

Guan et al., (2015) explained that research on ZVI is still in its infancy and there is a need for improving the efficiency of contaminant removal by overcoming ZVI's limitations such as; 1) ZVI's low reactivity toward contaminants caused by the passive layer generated during ZVI's manufacturing; 2) ZVI's reactivity drops over time caused by the precipitation of metal oxy(hydroxides); 3) ZVI's relatively small specific surface area; 4) ZVI is only efficient under acidic conditions because of the direct involvement of H^+ on the corrosion rate of ZVI; 5) ZVI's adsorption capacity and selectivity for organic material is especially low; and 6) ZVI's low reactivity causes the accumulation of toxic intermediates such as chlorinated hydrocarbons to form.

The two major limitations in contaminant sequestration through ZVI is its low reactivity due to coating of passive layers that formed via ageing and oxidation of the iron particles and the specific surface area of ZVI (Guan et al., 2015). Noubactep (2015) stated that ZVI removed organic and inorganic material through a combination of three mechanisms such as adsorption, co-precipitation and size-exclusion and various methods have been implicated and tested to enhance ZVI removal (Guan et al., 2015) and to overcome the limitations of ZVI. Zero-valent iron's ability to reduce and sequester contaminants can be enhanced by three methods; 1) Physical enhancement; 2) Coupled enhancement; and 3) Chemical enhancement.

Physical enhancement involves; Ultrasound to continuously clean the ZVI's surface and chemically activate the surface of Fe^0; Gas-bubbled ZVI, allowing H^+ to create an acidic environment for ZVI; UV-visible light, where reactive oxygen species would form on the surface of ZVI; and Microwave assisted technology.

Coupled enhancement involves the coupling of ZVI with activated carbon, pillared bentonite, zeolite and other iron oxides. These couplings provided additional adsorption sites, mass transfer of ZVI increased and a synergistic effect is created between the sorption and reduction of ZVI.

Chemical enhancement involves adding organic ligands such as EDTA or oxalate which forms complexes between ZVI and ligands eliminating iron oxy(hydroxides) that would precipitate on the ZVI's surface. Dosing ZVI with Fe^{2+}, Co^{2+} & Mn^{2+} was also an effective chemical enhancement where electron transfer of ZVI was improved. The enhancements mentioned above greatly improved ZVI's capability of removing contaminants, however, for this study these enhancements will not be investigated.

Other factors greatly influencing ZVI's magnetic characteristics, tendency to aggregate, surface oxidation and interaction with the environment is its particle size, surface charge, bulk composition and surface chemistry (Chekli et al., 2016). The major factor is the particle size of ZVI as it is directly related to its reactivity and specific surface area. The following section (2.3.2) elaborates on the particle sizes of ZVI.

2.4.3 ZVI: Physico-chemical characteristics of nano ZVI (nZVI), micro ZVI (mZVI) and granular ZVI (gZVI)

There seems to be larger contribution toward studying nZVI and little investigation on mZVI and gZVI (Fu et al., 2014; Noubactep, 2008), however, Velimirovic et al. (2014) conducted a study to determine the particle sizes, surface areas and lifetimes of nZVI, mZVI and gZVI, through anaerobic corrosion and H_2 production. Velimirovic et al. (2014) observed that mZVI has a lower corrosion rate (10 - 30 times lower) than nZVI making it ideal for passive remediation of sulfate-rich mine water. The particle sizes of ZVI are divided into three main categories presented in Table 2.3 and although nZVI has the biggest surface area, it has the shortest lifetime. Granular ZVI has the longest lifetime but a very small surface area. The surface area of mZVI is 10 times bigger than gZVI and has a predicted lifetime of 11 to 16 years, making it the best candidate in passive remediation.

Table 2.3: Physical properties of nZVI, mZVI & gZVI (Velimirovic et al., 2014)

	PSD[a]	BET[b]	Lifetime[c]
nZVI	60 - 90 nm	30 - 35 $m^2 g^{-1}$	0.34 - 1.62
mZVI	20 - 160 μm	~11.4 $m^2 g^{-1}$	11.2 - 16.2
gZVI	300 - 1300 mm	~1.15 $m^2 g^{-1}$	~137

a = Average particle size distribution (PSD).

b = Average specific surface area according to the Brunauer-Emmet-Teller surface analysis.

c = Extrapolated average lifetimes of ZVI in years.

Nano zero-valent iron receives the most attention for environmental remediation due to its affordable cost in chemical preparation, high reactive surface sites and high in-situ reactivity (Chekli et al., 2016; Elliott & Zhang, 2001; Wang & Zhang, 1997). According to Wang & Zang (1997), nZVI with surface areas in the range of 20 - 40 $m^2 g^{-1}$, can yield 10 – 1000 times greater reactivity compared with mZVI and gZVI. Unfortunately, nZVI had limited mobility and reactivity due to three basic mechanisms; nZVI's magnetic properties leading to natural aggregation, causing a loss in its reactivity and mobility in the environment; nZVI is prone to rapid surface oxidation leading to the formation of corrosion products inhibiting electron flow from Fe^0 to contaminant lowering reactivity and; nZVI becomes inert; and relatively immobile when attaching to larger minerals or aggregates (Chekli et al., 2016).

Pullin et al. (2017) stated that any form of Fe^0 (nZVI, mZVI or gZVI) has a zero-valent core with ferrous and ferric oxide surface layers after synthesis. This thickness of the surface, however, depends on the initial production and storage of the type of ZVI but the average thickness is ~3 nm thick (Wang et al., 2005).

2.4.4 ZVI: Fe^0 corrosion and iron (oxy)hydroxide formation

Zero-valent iron is not soluble in water. Furthermore, submersed in water, the corrosion of iron is an electrochemical process where Fe^0 is spontaneously oxidized. (Noubactep, 2009a; Noubactep, 2015). Zero-valent iron acts as the cathode and transfers electrons through the metallic iron to its surface, where water (H_2O), contains O_2 (acting as the

anode) which is reduced to form hydroxides, presented by the redox reactions in Equation 2.2;

$$Fe^{0}_{(s)} + O_{2(aq)} + 2H_2O_{(l)} \leftrightarrows 2Fe^{2+}_{(aq)} + 4OH^{-}_{(aq)} \quad (2.2)$$

At the ZVI's surface in water, the hydroxide ions can move inward to react with the Fe^{2+} ions diffusing from the oxidized surface, precipitating ferrous hydroxide in Equation 2.3.

$$Fe^{2+}_{(aq)} + 2OH^{-}_{(aq)} \leftrightarrows Fe(OH)_{2(s)} \quad (2.3)$$

In the presence of oxygen, further oxidation of ferrous hydroxide, Equation 2.4, rapidly produces ferric oxides, hydroxides and (oxy)hydroxides commonly referred to as rust.

$$4Fe(OH)_{2(s)} + O_{2(g)} \leftrightarrows 2Fe_2O_3 \cdot H_2O_{(s)} + 2H_2O_{(l)} \quad (2.4)$$

Mu et al. (2017) explained the iron oxide phases in the shell encapsulating the core is difficult to identify, however, FeO is expected to be the initial iron oxide to form in the oxide shell. Furthermore, the Fe-oxide shell is porous and Fe^{2+}, O_2 & H^+ can migrate through the shell. (Keenan & Sedlak, 2008; Lee et al., 2014; Li et al., 2014; Mu et al., 2017; Pullin et al., 2017). Stated previously and according to Noubactep (2009b), Fe^0 acts as a cathodic reactant and as the oxidative dissolution of Fe^0 occurs, freshly oxidized Fe^{2+} is diffused into the solution. This in turn causes pitting and edging on the Fe^0's surface and exposes fresh Fe^0. Chemical precipitation follows, where the iron is oxidized, consequently forming porous Fe-oxide and -oxy(hydroxide) layers on the Fe^0's surface. Mu et al., (2017) stated that the reaction of ZVI and oxygen is thermodynamically favoured above all other oxidizing agents such as NO_3^- and SO_4^{2-}, in a ZVI-solution system.

Equations 2.2, 2.3 and 2.4 presented the corrosion stages of Fe^0 in H_2O. The sequential growth of a typical Fe(II)/Fe(III)-oxide shell in the presence of O_2, on Fe^0, is presented by Equation 2.5 to 2.7 (Noubactep, 2008);

$$2Fe^{0}_{(s)} + O_{2(aq)} \leftrightarrows 2FeO_{(s)} \quad (2.5)$$

$$6FeO_{(s)} + O_{2(aq)} \leftrightarrows 2Fe_3O_{4(s)} \quad (2.6)$$

$$4Fe_3O_{4(s)} + O_{2(aq)} \leftrightarrows 6Fe_2O_{3(s)} \quad (2.7)$$

where Equation 2.5 represented the orange zone in the Fe oxide scale in Figure 2.2. The yellow scale (Fig. 2.2) showed continuous oxidation of FeO and the outward growth of Fe_3O_4 (Eq. 2.6), followed by further oxidation of Fe_3O_4 and the final growth stage of Fe_2O_3 (Eq. 2.7) and/or FeOOH.

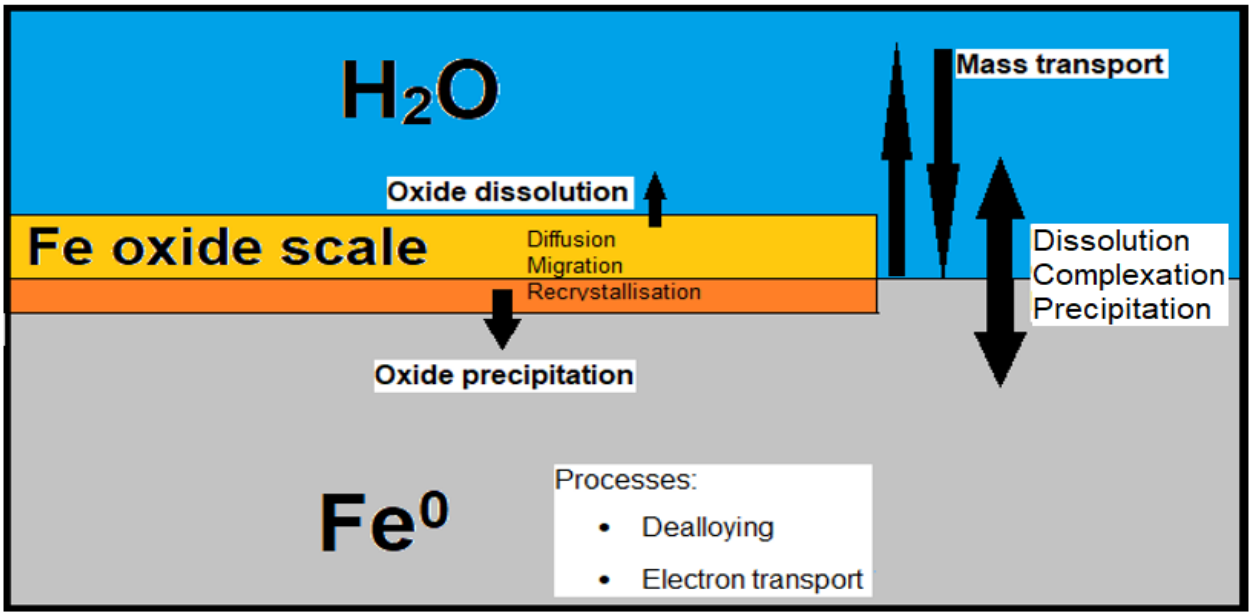

Figure 2.2: Simplified Fe^0/Fe(II)/(III)-oxide/H_2O system adapted from Noubactep, (2015)

The orange zone (Fig. 2.2) is dominated by Fe^{2+} and in the yellow zone (Fig. 2.2) there is a mixture of Fe(II) and Fe(III) and the Fe^{2+}/Fe^{3+} ratio is controlled by the solution's pH.

Noubactep (2008) and Noubactep (2015) stated that in a Fe^0/Fe(II)/Fe(III)-oxide/H_2O system the oxide layer will:

- Act as a semiconductor, creating pathways for electrons to transfer from the Fe^0's surface to the contaminant, referred to as direct reduction of contaminants.

- Re-adsorb Fe^{2+} to produce highly reactive structural Fe^{2+} sites on Fe^0's surface to reduce contaminants, referred to as indirect reduction of contaminants.
- Have variable charge and surface reactivity that enables it to sorb anions or cations depending on the pH.

2.4.5 ZVI: Contaminant sequestration by an Fe^0/Fe-oxide/H_2O system

Contaminants are immobilized and removed by Fe^0 through an electrochemical process. However, Fe(III)-oxide and (oxy)hydroxide layers, such as hematite (Fe_2O_3) and goethite (FeOOH), on the Fe^0's surface will inhibit electron transfer from the surface to the contaminant as hematite and goethite are non-conductive solid phases (Noubactep, 2008). The formation of Fe(II)/Fe(III)-oxide and (oxy)hydroxide layers enables the Fe^0/Fe-oxide/H_2O system to remove contaminants without the help of redox chemistry and was further validated by Noubactep (2009a) stating that contaminants are primarily removed through co-adsorption and co-precipitation and are stable within the oxide layers as the iron does not dissolve. Noubactep (2008) also reported that adsorbed or structural ferrous iron (structural Fe^{III}/Fe^{II}, E^o = -0.34 to -0.65 V) can be a more powerful reductant and remover of contaminants than Fe^0 (Fe^{II}/Fe^0, E^o = -0.45 V) itself.

Ferric iron is also reduced to Fe(II) by Fe^0, even more so in environments that are anoxic making this auto-reductive reaction an important process in Fe(0)/Fe(II)/Fe(III)-oxide/H_2O systems (Triszcz et al., 2009). Liu et al. (2013a) stated that Fe(II)/Fe(III) oxides and (oxy)hydroxide minerals such as magnetite and green rust are important constituents to reduce contaminants. Fe(III) oxides and (oxy)hydroxides, however, are fully oxidized and unable to reduce any contaminant but is still able to adsorb and precipitate contaminants, depending on the solutions pH.

Zero-valent aluminium (Al^{3+}/Al^0, E^o = -1.33) and Zn^0 (Zn^{2+}/Zn^0, E^o = -0.76) are more electrochemically reactive than iron but the rapid corrosion of Al^0 and Zn^0 forms mono-oxide scales of Al and Zn, pacifying the surface of Al^0 and Zn^0 immediately. The different oxidation states of iron ($Fe^{III}/Fe^{II}/Fe^0$) make it more suited for contaminant removal (Noubactep, 2009). Furthermore, the rate of aqueous iron corrosion was proportional to

the total amount of reducible species transferred to the ZVI particle's surface. Figure 2.3 illustrates the removal of contaminants on a ZVI particle in a Fe^0/Fe-oxide/H_2O-system.

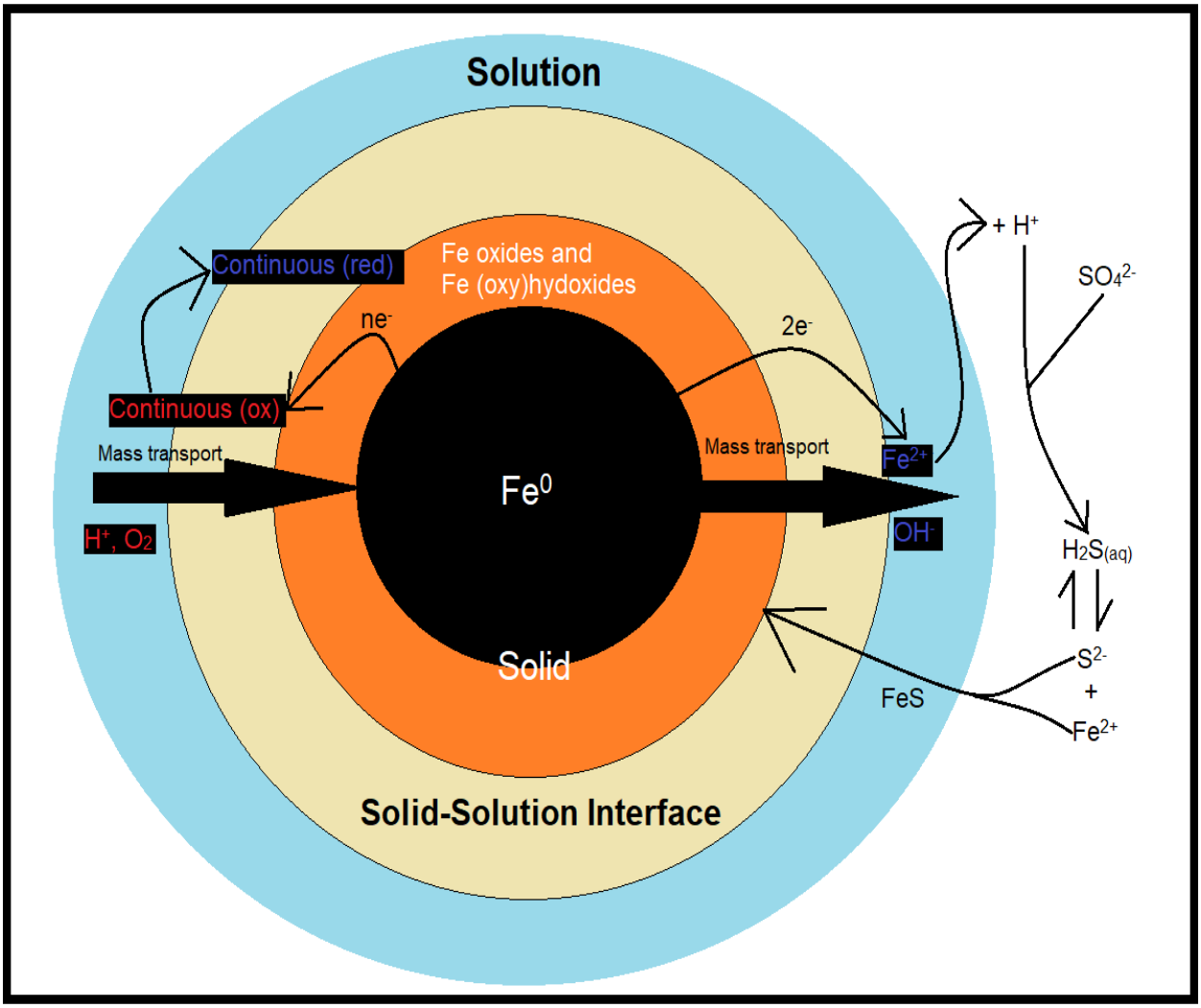

Figure 2.3: Simplified illustration of the corrosion of a ZVI particle submersed in solution (Guan et al., 2015)

2.4.6 ZVI: Sulfate and ZVI

Karri et al. (2005) investigated methanogenesis and sulfate reduction with anaerobic sewage sludge mixed with mZVI and reported that 0.804 *mM* (1.383 mg l^{-1}) sulfate was reduced by 0.834 *M* (46.5 g/l) Fe^0 and sulfate reducing bacteria (SRB) in 24 hours, stating

that mZVI could readily release electrons at a slow pace that reduced sulfate in anaerobic sewage sludge. Miao et al. (2012) stated that ZVI is oxidized by water, in the absence of O_2, producing ferrous iron and H_2 (Equation 2.8). Through microbial mediated reactions sulfate is then reduced by ferrous iron and H_2 to sulfide, which will form iron sulfide precipitates (Equation 2.9).

$$4Fe^0_{(s)} + 2H_2O_{(l)} \leftrightarrows Fe^{2+}_{(aq)} + H_{2(g)} + 2OH^-_{(aq)} \quad (2.8)$$

$$2Fe^{2+}_{(aq)} + SO_4^{2-} + 4H_{2(g)} \leftrightarrows FeS_{(s)} + 4H_2O_{(l)} \quad (2.9)$$

Studies conducted by Blowes et al. (2000), Karri et al. (2005) and Miao et al. (2012) found that ZVI reduced sulfate (S^{6+}) to sulfide (S^{2-}) through abiotic reduction and was presented in Equation 2.10;

$$2Fe^0_{(s)} + SO_4^{2-}{}_{(aq)} + 8H^+_{(aq)} \leftrightarrows FeS_{(s)} + Fe^{2+}_{(aq)} + 4H_2O_{(l)} \quad (2.10)$$

The possible iron sulfides that can form in pH ranges of 3 to 8 by increasing stability are; iron sulfide (FeS) which is the least stable form of the iron sulfides, greigite (Fe_3S_4) which is analog to magnetite, phyrrotite ($Fe_{1-x}S$ or $Fe_7S_{8)}$, troilite (FeS, and end member of phyrrotite), mackinawite ($Fe_{1-x}S$), marcasite (FeS_2, orthorhombic) and the most stable iron sulfide is pyrite (FeS_2, cubic).

2.5 Approach in selecting sulfate concentrations and pH values for the experimental section

2.5.1 Selecting River monitoring points

Borehole data from selected river monitoring points in the Mpumalanga Province of South Africa was used, obtained from an database provided on the website of the Department of Water and Sanitation (DWS). The river monitoring points selected are shown in the red area in Figure 2.4, indicated by blue markers labelled B1H002 to C1H045.

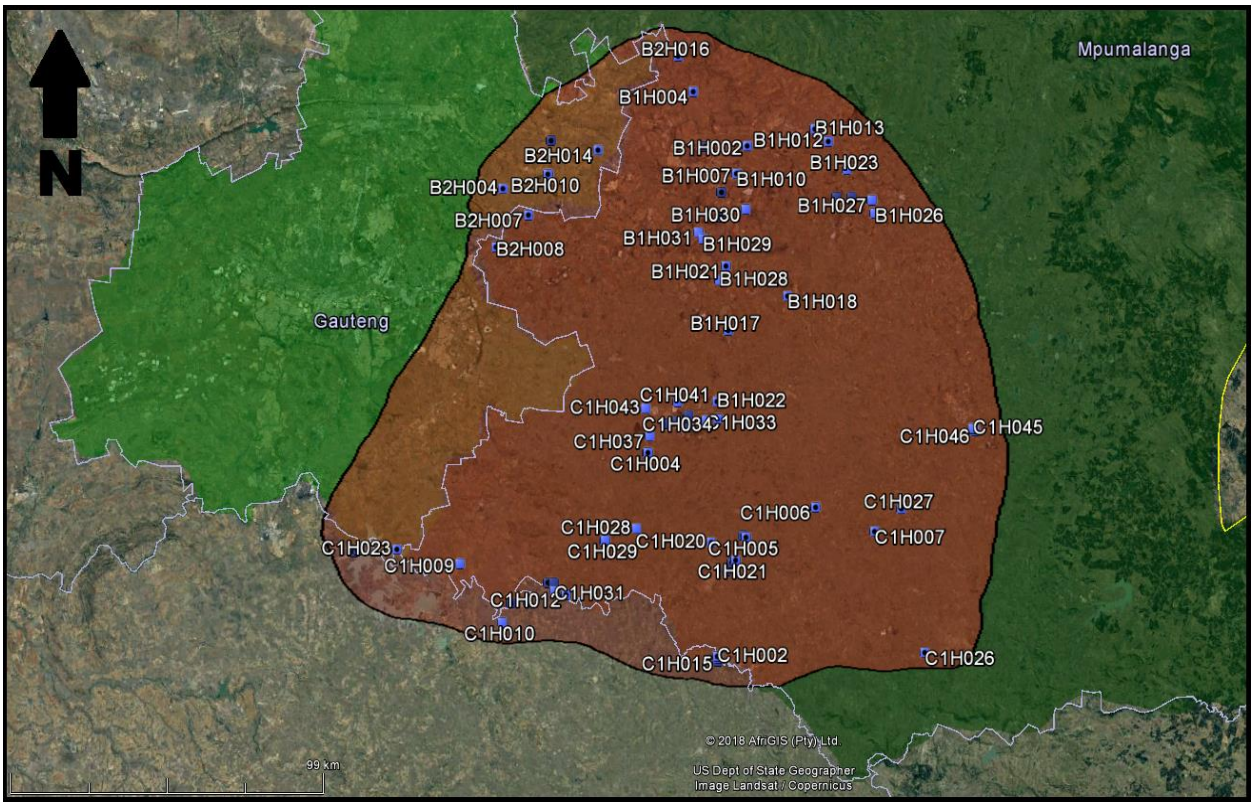

Figure 2.4: Locality of selected river monitoring points: 1997 – 2012 (DWS, 2013 & Google Earth)

The red area is an ideal location as it envelopes the Upper Olifants River catchment and includes the Olifants River and its various tributaries as well as a variety of mines, including gold to coal mines, where a wide range of sulfate concentrations and pH values were observed.

2.5.2 Selecting sulfate concentrations

It was clear that a range defining low to high sulfate concentrations needed to be established. Sulfate concentrations below 200 mg l^{-1} are considered safe (WHO, 2004b) and was not considered. Geldenhuys et al. (2003) reported that limestone ($CaCO_3$) and lime ($Ca(OH)_2$) can reduce sulfate concentrations of ~3000 mg l^{-1} to 1200 mg l^{-1}. And so, concentrations above 1200 mg l^{-1} were also not considered. A range between 200 and 1200 mg l^{-1} was therefore the aim. Borehole data from selected river monitoring points in the Upper Olifants River Catchment, provided by the DWS (2013), were analysed in order to obtain a perspective of the realistic sulfate concentrations.

Figure 2.5 showed that the lower range of sulfate concentrations at 200 to 300 mg l^{-1}, was the most frequent and so 300 mg l^{-1} was chosen, where it was sensible to include and evaluate a concentration in this range along with the higher concentration at 1200 mg l^{-1}.

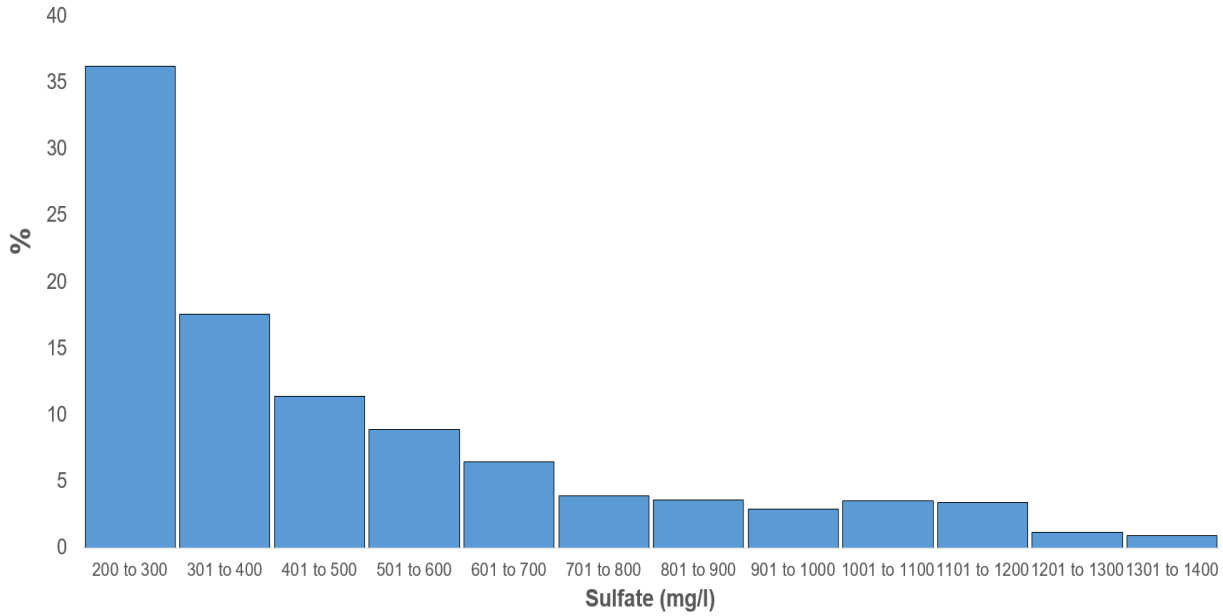

Figure 2.5: Histogram of sulfate concentration levels from borehole data of selected river monitoring points: 1997-2012 (DWS, 2013)

2.5.3 Selecting pH values

The removal and/or reduction of sulfate by ZVI was also to be investigated in acidic and alkaline conditions and the selection of these two pH vales were done with the same statistical approach as in 2.4.2. The same borehole data from selected river monitoring points in 2.4.2 were also used to acquire the pH range in Figure 2.6.

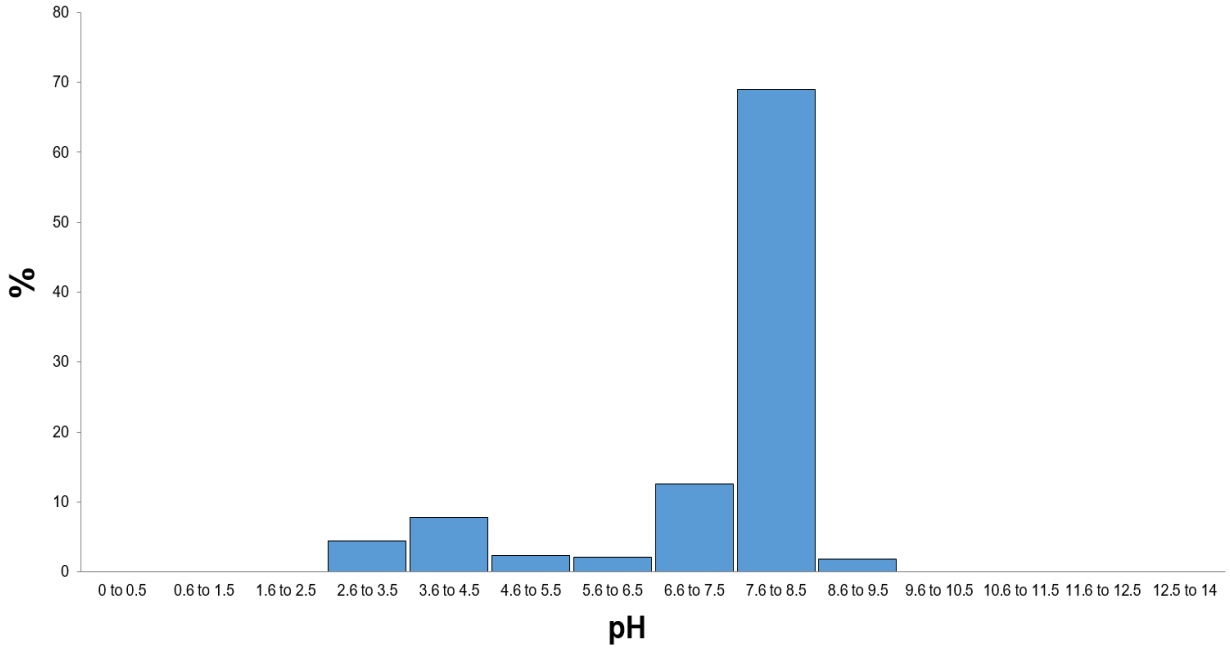

Figure 2.6: Histogram of pH ranges from borehole data of selected river monitoring points: 1997-2012 (DWS, 2013)

Overall, the most frequent range were pH 7.6 to 8.5, and this led to the decision to use a pH of 8 (Fig. 2.6). A second lower range (acidic) population also appeared (3.6 to 4.5) and to simplify the study, a pH value of 4 was chosen.

CHAPTER 3: PURGING DISSOLVED OXYGEN (DO)

3.1 Introduction

The reduction of sulfate is favoured by anoxic environments of low reduction potentials, less than -100 mV, therefore it was important to be able to create conditions optimal for sulfate reduction. Studies conducted by (Ling et al., 2015; Liu et al., 2013a; Liu et al., 2013b; Liu et al., 2014; Tang et al., 2014), purged DO from solutions with N_2 or argon gas, however, the methodology was vaguely described. Purging time used in these studies was long (1 - 2 hours) and it was not clear if it was arbitrarily decided on or established through research. Because of the experimental design, Ar purging for 1 to 2 hours per sample would have been impractical and too costly for this study.

This chapter aims to establish and validate an Ar purging protocol and also to better understand the response of different sulfate solutions degassing with respect to E_h, pH and electric conductivity (EC).

3.2 The process of degassing a solution

Argon was considered as the best option as it is a denser gas than N_2 (density of Ar = 1.784 g/l versus 1.25 g/l for N_2, at standard temperature and pressure (STP)) and will not diffuse into the air as readily as N_2.

Air is mainly composed of, on a mole fraction basis, 21% oxygen, 78% nitrogen (in the form of N_2) and 0.9% argon while the rest of the gasses such as neon and helium make up the 0.1%. Oxygen and argon has more or less the same solubilities in freshwater of (40 versus 55 mg l^{-1}) at a temperature of 25 °C and 1 atm, and also has the same temperature dependencies and diffusion coefficients at standard temperature and pressure (STP) (Hamme & Emmerson, 2004; Valderrama et al., 2016) but, as stated, argon is denser than oxygen (density) and when a solution is purged with argon, it will gradually displace oxygen at the solution's surface and blankets the surface, (Fig. 3.1).

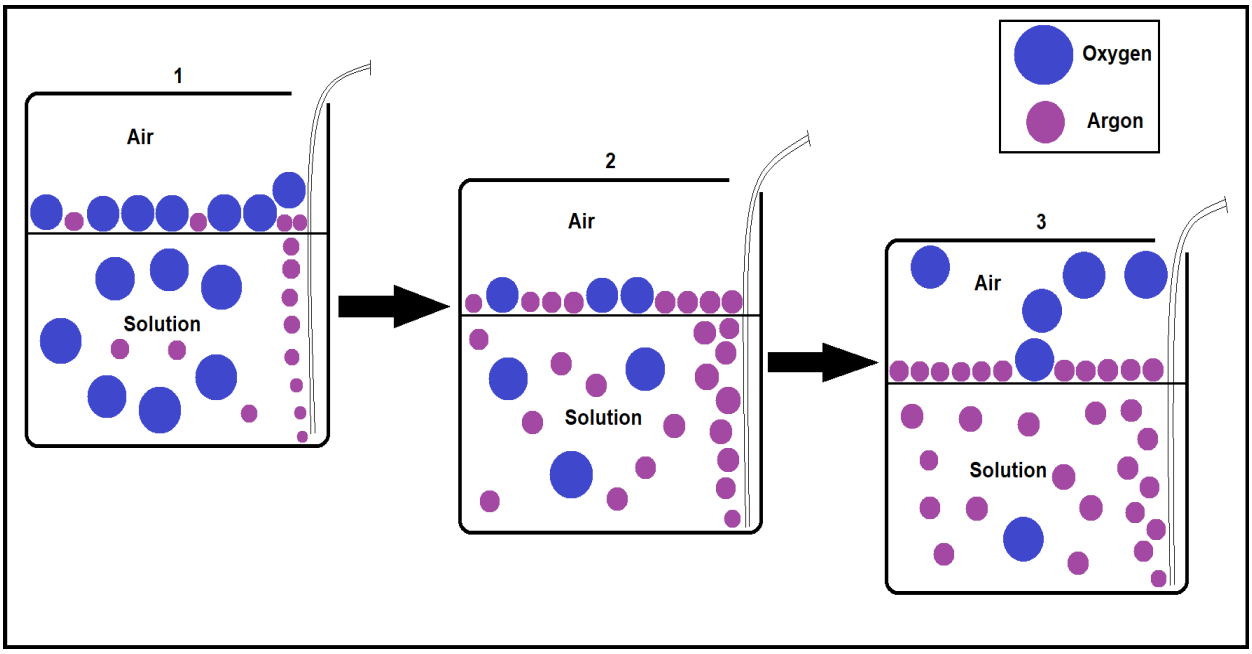

Figure 3.1: Simplified representation of argon purging oxygen

This in turn reduces the partial pressure of $O_{2(g)}$ at the solution's surface, (solutions 1 through 3 in Fig. 3.1). Henry's law states that the concentration of any gas in solution is directionally proportional to the gas's partial pressure. Therefore, if the partial pressure of $O_{2(g)}$ (PO_2) at the solution - air interface decreases, $O_{2(aq)}$ will diffuse out of solution in order to re-establish an equilibrium between the oxygen in the air above the solution and $O_{2(aq)}$.

However, the heavier $Ar_{(g)}$ gradually and effectively seals of the solution, making the partial $O_{2(g)}$ pressure at the solution-air interface negligible. The Le Chateliers' principal dictates that $O_{2(aq)}$ will continue to be forced out of solution and concentrations should eventually be negligible (Brown et al., 2006; Chang, 2008).

3.3 Materials and Methodology

3.3.1 Purging material, reagents and measuring equipment

Argon gas (99% purity) was obtained from Afrox SA, along with the argon pressure gauge used in the purging of DO. The tubing, connections and couplings were provided by Festo SA with brief descriptions of each item used for purging DO in Table 3.1. The nozzle was able to purge with a flow rate of 0.1 l s^{-1} and remove 0.0106 mg DO in one second, pre-tested on de-ionized water of 500 ml, 1 l and 2 l respectively.

Table 3.1: Purging equipment

ITEM	DESCRIPTION/PARAMETERS
Argon Cylinder	Afrox supplied Argon gas baseline 5.0 99% purity 17.4 kg, 10.5 m^3
Pressure Gauge	Argon/CO_2 Saffire Shieldmaster 0-30 l/min flow rate range Max inlet pressure: 23000 Pa
Tubing	Festo tubes, pneumatic, blue Outer diameter: 8 mm , Inner diameter 5.7 mm Polyamide, resistant to chemicals
Connections & Couplings	Festo couplings Polyamide, resistant to chemicals

High purity (99%) gypsum ($CaSO_4.2H_2O$) and epsomite ($MgSO_4.7H_2O$) were used in preparing all sulfate solutions. De-ionized water (DW) by MERCK Millipore (0.5 mS/cm at 25° C) was used throughout all the experiments. The IP67 COMBO Meter with DO probe was used to read the DO concentrations. The WTW pH 3310 with the Sentix Redox electrode was used to measure reduction potentials. METTLER TOLEDO SG87 with its pH and EC probes were used to measure the pH and electric conductivity (EC). Appendix A provided figures depicting the purging equipment (Fig. 1), experimental setup (Fig. 2) and measuring equipment (Fig. 3).

3.3.2 Purging dissolved oxygen (DO)

Three different sulfate solutions with concentrations of 1200 mg l^{-1} (12.5 *mM*) were prepared; a) $CaSO_4$ solution, b) $MgSO_4$ solution and a c) Ca-$MgSO_4$ solution (containing 6.25 *mM* of Ca and Mg) by weighing 2.15 g $CaSO_4.2H_2O$ for the $CaSO_4$ solution, 3.08 g $MgSO_4.7H_2O$ for the $MgSO_4$ solution and a 50:50 mixture of 1.08 g $CaSO_4.2H_2O$ and 1.54 g $MgSO_4.7H_2O$ for the Ca-$MgSO_4$ solution. The selected concentrations were chosen from the discussion in Chapter 2.4. The prepared solutions were made up in three separate volumetric flasks (1 l) with DW as control. The DW and sulfate solutions were transferred to individual 2 litre volumetric flasks. This was done for more convenient measurements (easier for the DO probe to be submersed in each flask making observations easier and consistent, depicted in Appendix A, Figure 4).

The argon purging nozzle and IP67 probe was inserted into the 2 l volumetric flask and DO, pH, E_h and EC of each solution and DW were recorded before and directly after DO was purged. Argon gas was pumped into each individual 2 l volumetric flask at 5 l/min for 6 minutes. The highest concentration of DO was removed between 5 and 6 minutes and after 6 minutes there were no changes in DO concentrations, concluding that 6 minutes was ideal. This procedure was repeated, over three days to determine the reproducibility of purging of the sulfate solutions. Three sulfate solutions and DW at 3 replications produced a total of 12 samples. Results are tabulated and discussed in section 3.4.

3.4 Results and Discussion

3.4.1 Dissolved oxygen (DO) in solution before purging

Thermodynamically it is known that gas solubility decreases when the ionic strength of a solution increases. This attributed to a decreasing affinity of a solution for non-polar oxygen molecules. The reaction between water and the ions drives out O_2 and this phenomenon is referred to as the "salting out effect" (Valderrama et al., 2016).

Pressure and temperature also influence the concentration of DO in saline solutions (Geng & Duan, 2010; Hamme & Emmerson, 2004; Valderrama et al., 2016). In a study by Benson & Krause (1984) it was determined that DO concentrations of freshwater and seawater (a highly heterogeneous solution) at 25 °C and 1 atm are 258 μM and 206 μM respectively, which also relates to modern literature (García & Gordon, 1992; Geng & Duan, 2010). This means that in fresh water to seawater, at 25 °C and 1 atm, DO can decrease from (258 μM) 8.26 mg l^{-1} to (206 μM) 6.59 mg l^{-1}.

The measured DO concentrations of the sulfate solutions were compared to DO concentrations, calculated by PHREEQCI and Equation 3.1, for said solutions and presented in Table 3.2. Benson & Krause (1984) created a model for calculating the DO concentration in water with temperature ranging from 0 to 45 °C and salinity ranging from 0 to 50 ppt (Eq. 3.1);

$$\begin{aligned} \ln C_O = {} & [-35.90205 + (1.575701 * 10^5)/(T) - (6.642308 * 10^7)/(T^2) \\ & + (1.243800 * 10^{10})/(T^3) - (8.621949 \times 10^{11})/(T^4) \\ & - S * (0.017674 - 10.754 / (T) + 2140.7/(T^2)\,)] \end{aligned} \quad (3.1)$$

where C_O is the concentration of DO in µM, T is the temperature in Kelvin and S is the salinity measured by the practical salinity scale of 1978 (PSS-78).

Table 3.2: The influence of the various solutions on $O_{2(g)}$ solubility (in µM)

	Measured	PHREEQCI	Equation 3.1
De-ionised water	198	270	281
$CaSO_4$	127	267	271
$MgSO_4$	130	267	271
Ca-$MgSO_4$	130	267	271

The measured DO concentrations in Table 3.2 were lower than DO concentrations in waters determined by Benson & Krause (1984) but this study was conducted at approximately 1350 m where the barometric air pressure is roughly 0.855 atm and not at 1 atm and because of lower barometric pressure the oxygen partial pressure is also approximately 14% lower than at sea level (0.21 *atm*). Using Dalton' Law this translates to a partial oxygen pressure of 0.885 *atm* * 0.21 = 0.186 *atm*.

Furthermore, the measured DO concentrations, from the solutions, were lower than the calculated DO concentrations determined by PHREEQCI and Equation 3.1. The DO concentrations of the solutions calculated by Equation 3.1 were slightly higher than the DO concentrations calculated by PHREEQCI. This was attributed to the fact that Eqaution 3.1 was developed for seawater (at sea level) and therefore does not take barometric pressure into account, and as previously stated, this study was conducted at a barometric pressure of approximately 0.855 atm, which will result in lower DO concentrations in the solutions. Dissolved oxygen concentrations calculated from both PHREEQC and Equation 3.1 do, however, fall within the DO concentration ranges presented by Benson & Krause (1984) but the measured DO concentrations from the solutions are lower than the calculated values because PHREEQCI and Equation 3.1 does not take atmospheric pressure into account.

Even with the difference between the measured DO and the calculated DO concentrations, it was clear that there were less DO in the sulfate solutions compared to the DW, showing that the salting out is measurable at mine water salinity levels.

3.4.2 Dissolved oxygen (DO) after purging

Purging DO with argon gas at 5 l/min for 6 minutes was successful for the DW as well as all sulfate solutions presented in Table 3.3, where 0.1 mg l^{-1} or 3 *µM* (96.8 - 97.0%) when DO was removed. Due to the blanket of argon gas that formed above each solution after purging, the DO concentration remained under 0.3 mg l^{-1} for more than 24 hours. The Ar gas is denser than O_2 and inhibited it from being re-adsorbed from the atmosphere.

Table 3.3: Effect of Ar purging on DO concentrations of solutions (in *µM*)

	Unpurged	**Purged**
De-ionised water	198 (± 3.61E-03)[a]	3.00 (± 1.69E-17)
$CaSO_4$	127 (± 4.77E-03)	3.00 (± 1.69E-17)
$MgSO_4$	130 (± 3.61E-03)	3.00 (± 1.69E-17)
Ca-$MgSO_4$	130 (± 4.77E-03)	3.00 (± 1.69E-17)

a = Values in brackets are the standard deviations of three readings.

With the successful purging of DO from the DW and sulfate solutions it was important to understand what concentrations of $Ar_{(g)}$ and $Ar_{(aq)}$ possibly formed and remained in these purged systems. Unfortunately, it was not possible to physically measure argon concentrations in solution or partial pressure at the solution - air interface but by using the Ideal Gas Law (PV = nRT) it was calculated that 40.85 mg l^{-1} (1.02 *mM*) argon could be pumped into a 1 litre volumetric flask. Using Henry's law constant (K_H) in Equation 3.2 it was possible to calculate the partial pressure of argon at the solution – air interface;

$$Pg = K_H * C_g \qquad (3.2)$$

where P_g is the partial pressure of argon, K_H is the gas constant of argon at 714.28 $l \cdot atm \cdot mol_{gas}^{-1}$ and *Cg* is the molar concentration of said gas.

It was calculated that the partial pressure of Ar above each solution's surface would be 0.27 *atm*, which was higher than the partial pressure of oxygen (0.21 *atm*) at STP.

3.3.3 Redox potential, pH and EC of solutions before and after purging

This was important to assess if a solution saturated with dissolved Ar had possible impacts on its redox measurements. The electron activity of the DW and sulfate solutions were calculated by using Equation 3.3, and was another way to validate the reductive status (oxic, sub-oxic or anoxic) of the sulfate solutions before and after purging with argon gas;

$$pe = \frac{FE}{RTln10} \tag{3.3}$$

where *pe* is the negative logarithm of electrons in solution. *F* is the Faraday constant, the number of coulombs per mole of electrons ($9.64853399*10^4$ C mol^{-1}). *E* is the cell potential (electromotive force) at the temperature of interest, measured in mV. *R* is the universal gas constant (8.314472 J K^{-1} mol^{-1}). *T* is the temperature in Kelvin.

Table 3.4: The influence of Ar purging on the redox potential of DW and sulfate solutions

	Unpurged		**Purged**	
	REDOX (mV)	**pe**	**REDOX (mV)**	**pe**
De-ionised water	240 (± 17.1)[a]	4.0	170 (± 17.1)	3.0
$CaSO_4$	276 (± 26.8)	4.7	272 (± 26.7)	4.6
$MgSO_4$	324 (± 7.21)	5.5	322 (± 7.21)	5.5
Ca-$MgSO_4$	332 (± 9.54)	5.7	324 (± 9.50)	5.5

a = Values in brackets are the standard deviations.

The *pe* values of the DW and sulfate solutions were between 3 and 6, presented in Table 3.5, and it was clear that the sulfate solutions had higher pe values due to the Ca and Mg ions in the sulfate solutions, which was strange because Ca and Mg are not redox active. Furthermore, Table 3.4 showed that the purged DW's E_h decreased by 70 mV, compared to the unpurged DW's E_h. This was expected as the DO concentration was decreased.

The sulfate solutions' redox potentials, however, only decreased slightly when DO was purged and showed that decreasing DO concentration and the presence of Ar in a solution did not influence the redox state, when dissolved Ca, Mg & SO_4 was included.

Table 3.5: The influence of Ar purging on the pH and EC of DW and sulfate solutions

		Unpurged	Purged
De-ionised water			
	pH	6.96 (± 0.10)[a]	7.17 (± 0.06)
	EC (mS/m)	0.12 (± 0.02)	0.15 (± 0.06)
$CaSO_4$			
	pH	6.30 (± 0.04)	5.87 (± 0.16)
	EC (mS/m)	184 (± 2.15)	187 (± 2.15)
$MgSO_4$			
	pH	6.05 (± 0.02)	5.85 (± 0.07)
	EC (mS/m)	185 (± 0.38)	184 (± 0.38)
Ca-$MgSO_4$			
	pH	6.20 (± 0.08)	5.70 (± 0.17)
	EC (mS/m)	188 (± 0.10)	187 (± 0.10)

a = Value in brackets are the standard deviations.

The pH values for the DW increased slightly when DO was purged (Table 3.5), caused by the inhibition of O_2 from the atmosphere being re-adsorbed by DW. The electric conductivity (EC) of DW and the sulfate solutions did not change as argon gas is inert and did not increase salinity in DW or the sulfate solutions.

3.5 Conclusion

The aim of this chapter was to establish and validate an Ar purging protocol as literature detailing the methodology of Ar purging was sparse. This study therefore started-off with a revisit of the methodology for oxygen purging with Ar to obtain a detailed understanding of the response of different salt solutions ($CaSO_4$, $MgSO_4$ and Ca-$MgSO_4$) used in this study. The method was quite effective, and it was concluded that with the procedure

followed argon readily purged oxygen. The method was able to remove 98% (~4.1 mg l^{-1} to 0.1 mg l^{-1}) DO from the sulfate solutions and 98% from DW (~6.3 mg l^{-1} to 0.1 mg l^{-1}). Dissolved oxygen remained at 0.1 mg l^{-1}, when the DO probe was submersed for 24 hours.

Furthermore, the sulfate solutions had less DO than DW, which proved that dissolved salts decreased a solution's DO concentration. The E_h of DW decreased by 70 mV after purging with Ar, while the sulfate solutions' redox potentials only differed by ~12 mV at the most, caused by the dissolved Ca, Mg and sulfate in the sulfate solutions. Purging DO from the solutions had negligible impact on the pH and EC.

It can also be inferred, from these findings, that when salinization of a wetland occurs (contamination through saline mine water from farming or mining), less oxygen can dissolve from the atmosphere and will lead to decreases in DO concentrations. The addition of ZVI, when applied in wetland systems, will be problematic because ZVI will further consume oxygen from these systems.

CHAPTER 4: EVOLUTION OF mZVI REDOX POTENTIALS IN ACIDIC AND ALKALINE SOLUTIONS

4.1 Introduction

This study depends on the capability of mZVI to induce low redox potentials in saline solutions, redox potentials below -100 mV (optimally, ≤-200 mV, or lower). Dissolved oxygen in the system is expected to disrupt mZVI's reductive capabilities as it is an oxidizing agent that can inhibit low reduction potentials. The constant presence of dissolved oxygen will also inevitably result in amorphous ferric oxide shell formation around the Fe^0-core (see 2.4.3). According to Yan et al. (2010) and Mu et al. (2017) ferric oxide shells restrict the electron flow from Fe^0.

Chapter 4 aims to investigate mZVI reduction behaviour, as reflected by reduction potential changes, in acidic and alkaline ZVI-sulfate solution in oxygen purged and unpurged systems.

4.2 Materials and Methodology

4.2.1 Reagents

Micro-zerovalent iron (mZVI), (97%, fine powder, ~44 µm), sourced from Sigma-Aldrich, was used as the reducing agent. The sulfate salts, gypsum and epsomite, used to prepare the saline solutions in Chapter 3 were also used for this chapter.

4.2.2 Preparation of acidic (pH = 4) and alkaline (pH = 8) sulfate solutions

The same sulfate solutions and concentrations used in Chapter 3 were also prepared for this chapter. Sub-samples of these solutions; $CaSO_4$, $MgSO_4$ and Ca-$MgSO_4$ were adjusted to a pH of 4 and 8. Hydrochloric acid (10 *mM*) was used to adjust acidity because Cl^- cannot be reduced, and so mZVI will favour SO_4^- reduction. Sodium hydroxide (10 *mM*) was used to adjust alkalinity because Na^+, at this low concentration, will not interfere with Ca^{2+} or Mg^{2+} in solution. The pH selections were discussed in Chapter 2, section 2.5. Forty millilitres of each solution, (pH 4 and 8 solution), was dispensed into separate 50 ml centrifuge tubes containing 1 g of mZVI. The dosage rate, 1 g ZVI per 40 ml solution (25

g l^{-1} or 2.5%) was selected because Plessl et al., (2022) reported that a dosage rate of 2% (20 g l^{-1}) ZVI showed optimal sorption results. Two sets of controls were created, where the 1st set was the various sulfate solutions (at pH = 4 and 8) without mZVI and the second set was de-ionized water (at pH = 4 and 8) with mZVI, from this point forward the latter is referred to as FeDW.

The $CaSO_4$, $MgSO_4$, Ca-$MgSO_4$ solutions and controls were duplicated, and the one set was purged with argon gas. The same argon purging procedure was used as described in Chapter 3, however, just a smaller volume of 40 ml was purged (for a minimum of 30 seconds). The purged samples were sealed by tightly closing the cap (of the centrifuge tube) with polytetrachloroethelene (PTCE) tape followed by vacuum sealing, to ensure anaerobic conditions and to inhibit leaking of solutions or contamination by atmospheric oxygen. Figures 1 and 2 (Appendix B) depicted the preparation and storing of the samples while the unpurged samples were not vacuum sealed. A large number of batches were prepared to ensure that there were enough samples to be sacrificed, logged and discarded for each allocated day, to avoid oxygen contamination. Figure B4.1 depicts the packing and storing and Figure B4.2 depicts the measuring and logging of each sample (Appendix B). The redox potentials of the mZVI-sulfate solutions were recorded 6 hours after the initial reaction started and on day 1 to 8, 10, 12, 14 and 16.

Redox potential measurements of the FeDWs were logged every hour, for 6 hours, after the initial reaction. Furthermore, E_h measurements of FeDW were also logged on day 1 to 6, 8, 10, 12, 14 and 16. The measurement taken after 6 hours was because of a study by Zhang & Huang (2006) that explained that 1g of mZVI consumed up to 95% of DO, after 6 hours, in a 20 ml solution. Dissolved oxygen measurements were only taken on day 1 and 16 to verify if purging with argon gas was effective. The experimental design (Fig. 4.1) illustrates the main samples, each with 3 replicates, where the 3 unpurged sulfate solutions (acidic and alkaline) with mZVI were prepared for the initial 6-hour measurement and were re-tested on allocated days. DO contamination was allowed to better understand how quickly re-oxygenation takes place. The 3 unpurged sulfate

solutions (acidic and alkaline) with mZVI were prepared in excess to be measured individually for each allocated day as DO contamination is not allowed.

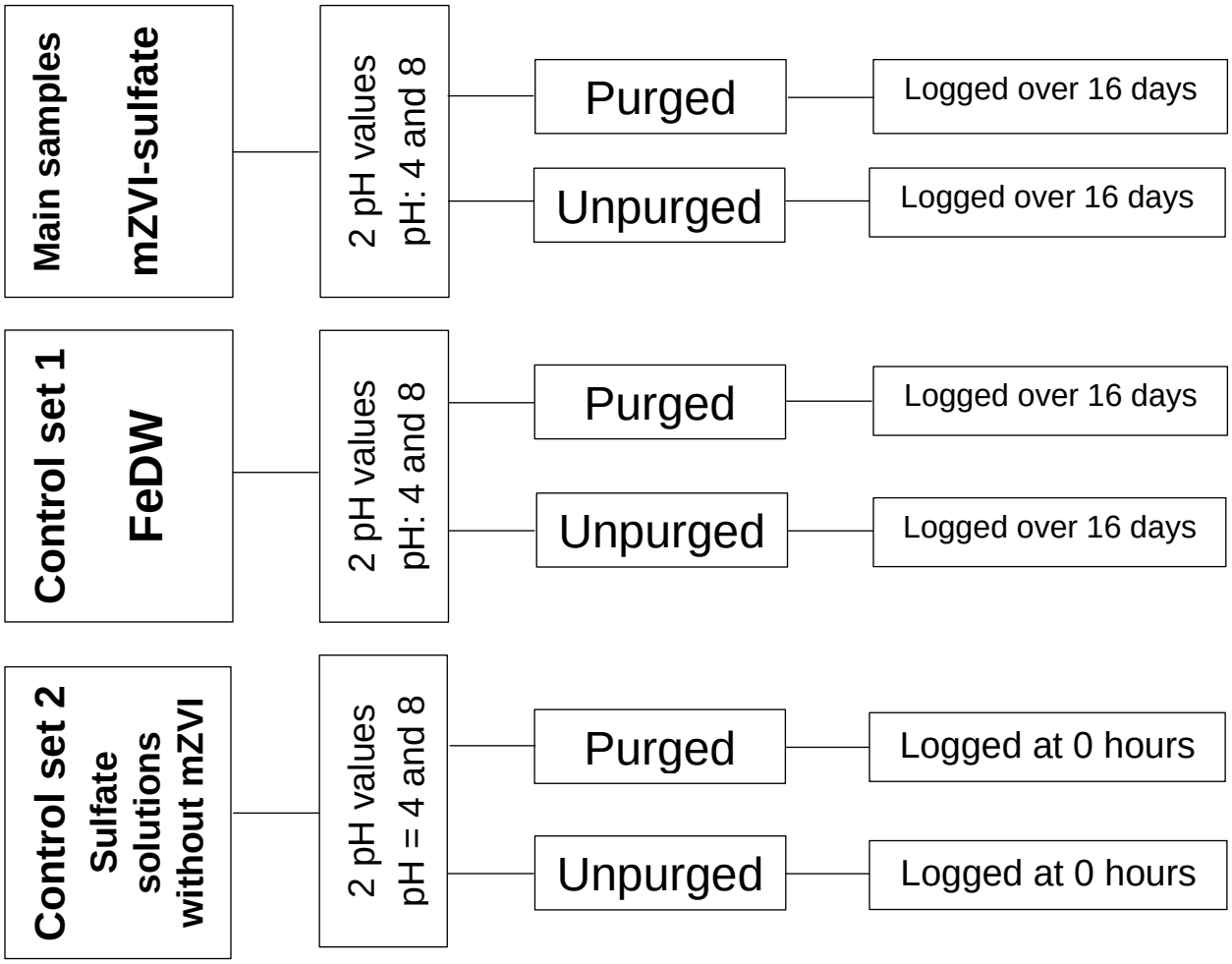

Figure 4.1: Experimental design for the $CaSO_4$, $MgSO_4$ and Ca-$MgSO_4$ solutions

4.3 Results and Discussion

Chapter 5 provides a more in-depth discussion on how ZVI reacted with the sulfate, Ca and Mg in solutions.

4.3.1 Redox potential changes of mZVI-de-ionized water systems

It was expected that a purged ZVI-de-ionized water (FeDW) system would achieve lower redox potentials compared to an unpurged FeDW system. Furthermore, it was expected that FeDW that was initially acidic would achieve lower reduction potentials compared to

a system that was initially alkaline. After 5 hours the purged alkaline solution (ALK_FeDW_P) produced the lowest reduction potential (-179 mV), followed by the purged acidic solution (AC_FeDW_P = -167 mV) and showed that ZVI was able to effectively decrease the O_2 concentration. It was also evident that lower redox potentials were achieved in alkaline systems. Furthermore, oxidation of mZVI produced a high buffering capacity in FeDW systems (Table 4.1).

Table 4.1: Redox potentials of acidic & alkaline FeDWs

	0 hours	5 hours	6 hours	16 days
AC_FeDW_U				
Redox (mV)	223 (± 2.00)[a]	-135 (± 3.06)	-112 (± 3.00)	68.0 (± 2.00)
pH	4.00 (± 0.01)	8.90 (± 0.04)	9.20 (± 0.02)	10.1 (± 0.01)
AC_FeDW_P				
Redox (mV)	220 (± 2.00)	-167 (± 2.00)	-139 (± 3.00)	70.7 (± 1.00)
pH	4.00 (± 0.01)	8.64 (± 0.01)	8.97 (± 0.05)	10.2 (± 0.01)
ALK_FeDW_U				
Redox (mV)	81.0 (± 3.00)	-149 (± 2.00)	-139 (± 2.00)	61.3 (± 2.00)
pH	8.00 (± 0.01)	9.44 (± 0.03)	9.67 (± 0.01)	10.1 (± 0.01)
ALK_FeDW_P				
Redox (mV)	78.0 (± 3.00)	-179 (± 3.00)	-152 (± 2.00)	52.3 (± 3.00)
pH	8.00 (± 0.01)	9.29 (± 0.06)	9.55 (± 0.06)	10.1 (± 0.01)

a = Value in brackets are the standard deviation of samples.

Table 4.1 showed that after 5 hours ZVI increased the pH, for all FeDW systems, to a value of ±9. For the unpurged FeDW (AC_FeDW_U and ALK_FeDW_U) the increase in pH was attributed to aqueous iron corrosion by oxygen oxidation (Equation 4.1). For the purged FeDW systems (AC_FeDW_P and ALK_FeDW_P) the increase in pH was attributed to possibly aqueous iron corrosion by hydrogen evolution (Equation 4.2) because in the absence of any other oxidant, H^+ will act as electron acceptor (Miao et al., 2012; Noubactep, 2008). Furthermore, for FeDW systems pertaining natural pH ranges (4 to 10), sorbed Fe(II) readily hydrolyses water, forming $>Fe(OH)_2$ at the surface of ZVI, which is expected to generate acidity (Equation 4.3) (Guan et al., 2015). After 6 hours the pH of all the FeDW were buffered between the values of 9 and 10. This shows that the reactions taking place on net generated alkalinity, presented by Equation 4.1

(unpurged FeDW) or Equation 4.2 (purged FeDW). But hydrolyses will again generate H^+ (Eq. 4.3), however, the pH showed a net alkaline reaction.

$$2Fe^0_{(s)} + O_{2(aq)} + 4H^+ \leftrightarrows 2Fe^{2+}_{(aq)} + 2H_2O_{(l)} \quad (4.1)$$

$$Fe^0_{(s)} + 2H^+_{(aq)} \leftrightarrows Fe^{2+}_{(aq)} + H_{2(g)} \quad (4.2)$$

$$Fe^{2+}_{(aq)} + 2H_2O_{(l)} \leftrightarrows >Fe(OH)_{2(s)} + 2H^+_{(aq)} \quad (4.3)$$

Where $>Fe(OH)_2$ is a generic A-type ferrous hydroxide functional group, which is bonded on mZVI's surface. The anoxic oxidation of $>Fe(OH)_2$ to magnetite is possible and occurs through the Schikorr reaction (Equation 4.4). During this reaction two protons from water molecule is reduced. This reaction rate increases at room temperature with increasing formation of $>Fe(OH)_2$ on the surface of ZVI (Mizutani et al., 2008).

$$>3Fe(OH)_{2(s)} \leftrightarrows >Fe_3O_{4(s)} + 2H_2O_{(l)} + H_{2(g)} \quad (4.4)$$

Heterogeneous Fe(II) oxidation by magnetite will then occur, where electron transfer from Fe(II) in magnetite to ($>Fe(OH)_2$) is possible (Jones et al., 2014). Furthermore, magnetite transformation is enhanced when Fe(III) is formed and Fe(II) will again adsorb, hydrolyse and form $>Fe(OH)_2$, together with magnetite, on ZVI's surface. Magnetite did form on the surfaces of ZVI as will be shown later in Chapter 5.

The E_h in the FeDW systems are possibly controlled by the following redox couples; magnetite (Fe^{III}/Fe^{II}, E° = +47 to -477 mV); and $>Fe(OH)_2$/ZVI (Fe^{II}/Fe^0, E° = -450 mV). The variable E_h of magnetite is the result of the stoichiometric ratio of ferrous and ferric iron (x = Fe(II)/Fe(III)) and dissolved Fe^{2+}. If x = ~0.17 the solution will have a E_h close to ~+47 mV and if x = 0.50 the solution will have a E_h close to ~-477 mV. The E_h of $>Fe(II)/Fe^0$ is also influenced by the dissolved concentration of Fe^{2+} (Gorski et al., 2010). Figure 4.2 showed the change in E_h for all FeDW systems over a 16-day period. For the FeDW systems, initial concentration of dissolved Fe^{2+} was 0 *mM* and after day 1 the

concentration increased to 3.38 *µM*, but after day 16, however, the concentration decreased to 0.77 *µM* (Chapter 5). The decrease is attributed to magnetite formation. Zero-valent iron, in the absence of a strong electron acceptor at high quantities, could not sustain reduction potentials low enough for abiotic reduction of sulfate and after 6 hours the E_h increased, where an equilibrium E_h was reached after day 4.

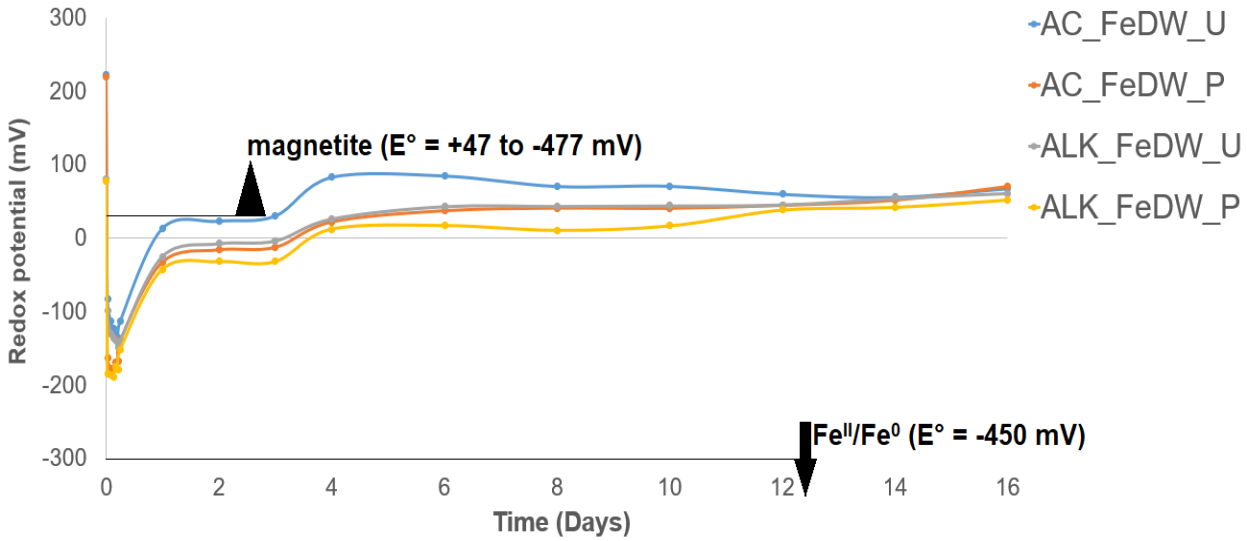

Figure 4.2: The change in redox potentials for the ZVI-DW systems

This experiment therefore showed that ZVI, in a FeDW system, was only capable of producing reduced conditions (<-135 mV) for 5 hours. The redox potentials also ended close to that of a system where magnetite with low Fe(II) occur and controlled the E_h.

4.3.2 Redox potential changes of ZVI-sulfate systems

The fundamental difference for the sulfate solutions (unpurged and purged) was that the redox potentials did not increase as in 4.3.1. In fact, it decreased to very low potentials which were expected to be conducive for abiotic sulfate reduction, which is evidence of S(VI) reduction to lower oxidations states (0, 1-, 2- or 3-). Sulfate is an electron acceptor which thermodynamically is easier to reduce than H^+. The pH also increased for the acidic and alkaline sulfate solutions and was buffered between the values of 6 and 10, similar to the FeDW systems (Table 4.1). It was expected that for the unpurged sulfate solutions DO would enhance Fe(III) oxide formation and increase acidification. This will lead to an

increased sorption of sulfate and would pacify the surface of ZVI. Which in turn, will reduce ZVI's capability to induce less negative redox potentials (<-100 mV). Purging DO, on the other hand, was expected to reduce Fe(III) oxide formation, increase alkalinity, and induce more negative reduction potentials quicker. It was also expected that corrosion of ZVI's surface is enhanced for the acidic sulfate solutions and would gain a reductive advantage over the alkaline sulfate solutions.

It seemed that, for the various in ZVI-sulfate (ZVI-SO_4) systems, that the type of sulfate solution was a more dominant driver in determining the "end-point" E_h (Table 4.2). DO concentration, determined how quickly redox potentials became negative after 6 hours, while (initial) acidity or alkalinity impacted the start of the reactions and had a minor impact on the trajectory of the reactions. In the case of the $CaSO_4$ solutions (unpurged and purged) the initial acidity or alkalinity appeared to have had an impact, where reduction potentials of -81 & -292 mV (unpurged solutions) and -55 & -284 mV (purged solutions) were produced. However, the acidic and alkaline $MgSO_4$ solutions produced much lower reduction potentials of -387 and -337 mV. While the acidic and alkaline Ca-$MgSO_4$ solutions produced the lowest reduction potentials of -484 and -483 mV, respectively.

Table 4.2: Redox potentials of sulfate solutions

	0 hours	6 hours	16 days
Ac_$CaSO_4$_U			
Redox (mV)	307 (± 5.00)[a]	-40.0 (± 1.00)	-82 (± 2.00)
pH	4.00	8.60 (± 0.01)	7.23 (± 0.02)
Ac_$CaSO_4$_P			
Redox (mV)	266 (± 4.00)[a]	-85.0 (± 4.00)	-55 (± 3.00)
pH	4.00	8.45 (± 0.027)	7.13 (± 0.02)
Alk_$CaSO_4$_U			
Redox (mV)	180 (± 2.00)	-74.0 (± 4.00)	-292 (± 2.00)
pH	8.00	9.40 (± 0.02)	8.10 (± 0.10)
Alk_$CaSO_4$_P			
Redox (mV)	180 (± 8.00)	-208 (± 7.00)	-284 (± 2.00)
pH	8.00	9.31 (± 0.02)	8.06 (± 0.06)
Ac_$MgSO_4$_U			
Redox (mV)	318 (± 4.00)	-14.3 (± 2.00)	-387 (± 2.00)
pH	4.00	7.03 (± 0.02)	6.36 (± 0.03)
Ac_$MgSO_4$_P			
Redox (mV)	270 (± 5.00)	-73.0 (± 4.00)	-477 (± 4.00)
pH	4.00	7.23 (± 0.02)	6.27 (± 0.02)
Alk_$MgSO_4$_U			
Redox (mV)	192 (± 6.00)	-45.3 (± 4.00)	-337 (± 2.00)
pH	8.00	9.30 (± 0.03)	6.87 (± 0.02)
Alk_$MgSO_4$_P			
Redox (mV)	210 (± 3.00)	-209 (± 1.00)	-351 (± 2.00)
pH	8.00	9.28 (± 0.02)	6.85 (± 0.01)
Ac_Ca-$MgSO_4$_U			
Redox (mV)	301 (± 2.00)	-32.7 (± 3.00)	-484 (± 1.00)
pH	4.00	7.17 (± 0.01)	6.31 (± 0.01)
Ac_Ca-$MgSO_4$_P			
Redox (mV)	256 (± 5.00)	-77 (± 3.00)	-459 (± 1.00)
pH	4.00	7.22 (± 0.025)	6.30 (± 0.07)
Alk_Ca-$MgSO_4$_U			
Redox (mV)	177 (± 6.00)	-62.0 (± 3.00)	-483 (± 4.00)
pH	8.00	9.74 (± 0.04)	7.04 (± 0.01)
Alk_Ca-$MgSO_4$_P			
Redox (mV)	176 (± 2.00)	-202 (± 5.00)	-497 (± 1.00)
pH	8.00	9.37 (± 0.20)	7.04 (± 0.01)

a = Value in brackets are standard deviation of samples.

The reason for the higher redox potentials observed in the $CaSO_4$ solutions could be attributed to gypsum precipitation, which (temporarily) obstructed ZVI's capability to transfer electrons. However, gypsum will not be stable on ZVI's surface and will breakdown through reductive decomposition of S(VI), whereas the redox in-active CaO and $Ca(OH)_2$ will remain on ZVI's surface, stabilized by the alkaline environment created. It will be shown later in Chapter 5 that $Ca(OH)_2$ occurred at XRD detectable levels. Furthermore, H^+ will dissociate from surface Fe(III) hydroxyl groups ($>Fe^{III}\text{-}OH_2^{0.5+}$ on magnetite surfaces) between the pH values of ~7 and ~9, to form $>Fe^{III}\text{-}OH^{0.5-}$, which can participate in cation exchange. Ca^{2+} and/or Mg^{2+} can exchange with H^+ at the surface of the $>Fe^{III}\text{-}OH^{0.5+}$, to form $>Fe^{III}OCa^{1.5+}$ or $>Fe^{III}OMg^{1.5+}$. H^+ can be re-adsorbed elsewhere by ZVI and corrode and re-activate passivated surfaces. Ca^{2+} and/or Mg^{2+} can also be adsorbed by $>Fe^{III}\text{-}OH^{0.5+}$ without H^+ exchange ($>Fe^{III}OHCa^{2.5+}$ or $>Fe^{III}OHMg^{2.5+}$), decreasing the activity of H^+ in solution (Liu et al., 2013b; Liu et al., 2014).

A higher resolution look at E_h change over time for the $CaSO_4$ solutions showed that it fluctuated substantially between 0 and -300 mV (Fig. 4.3). It was observed E_h decreased on days 1, 5, 6, 13 and 14 and increased on days 2 to 4, 7 to 12 and 15 to 16. The substantial fluctuation could be the reductive decomposition of gypsum that enabled electron transfer, on ZVI's surface again.

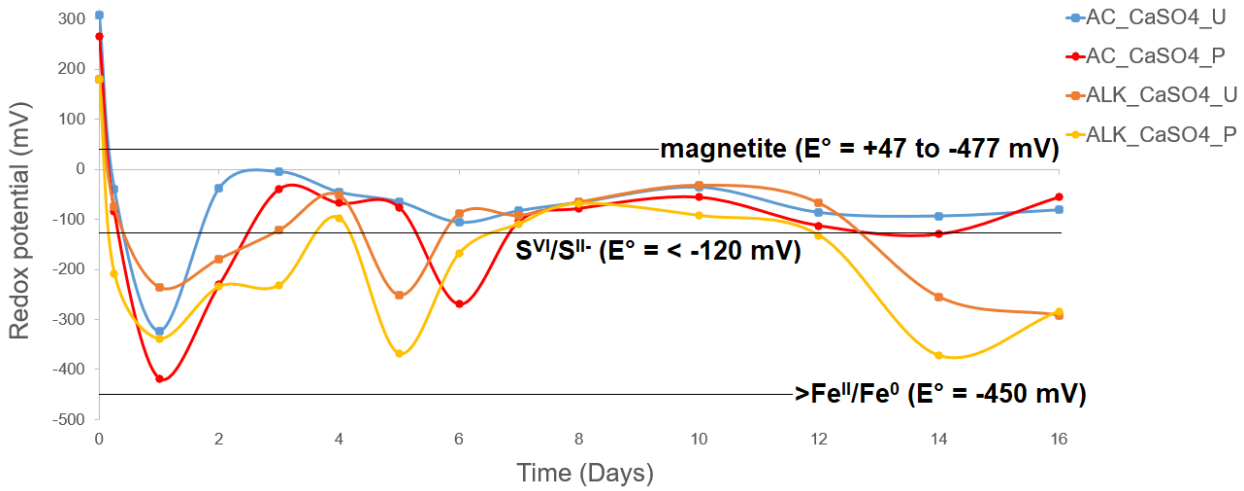

Figure 4.3: The change in redox potentials for $CaSO_4$-ZVI systems

In contrast to the $CaSO_4$ solutions, the $MgSO_4$ solutions showed a clearer decreasing trend with time and ending at much lower redox potentials after 16 days (Fig. 4.4). Furthermore, there was no evidence of Mg precipitating on ZVI's surface that could potentially inhibit electron transfer. This also leads to increased corrosion of ZVI and the excessive dissolution of Fe(II), discussed in Chapter 5, enabling lower redox potentials in the solution.

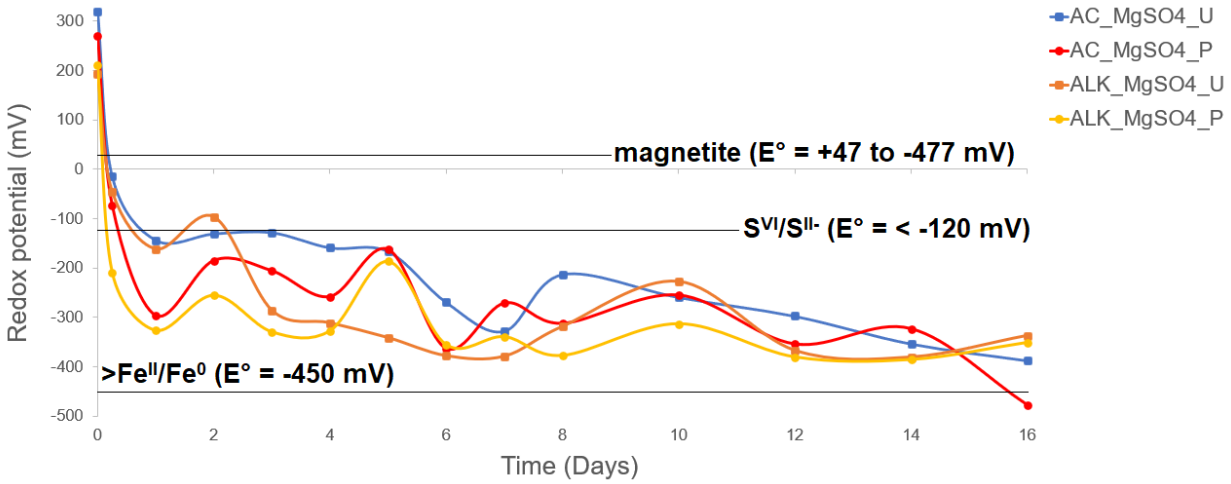

Figure 4.4: The change in redox potentials for ZVI-$MgSO_4$ systems

Figure 4.5 showed that Ca-$MgSO_4$ solutions exhibited almost a linear decrease with time and, as pointed out earlier, reached the lowest redox potentials. The fluctuations observed for the other solutions were not observed here and a synergism existed between Ca and Mg which allowed the development of very low reduction potentials.

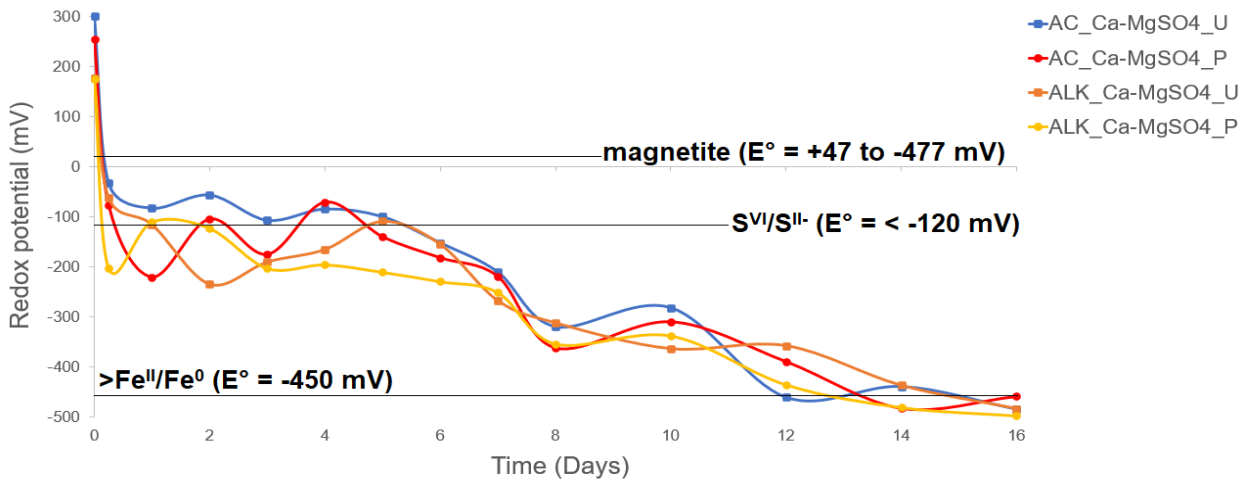

Figure 4.5: The change in reduction potentials of ZVI-Ca-$MgSO_4$ systems

This experiment therefore showed that the removal (purging) of oxygen at the beginning appeared almost inconsequential. ZVI was capable of producing and maintaining reduced conditions for all sulfate solutions. The type of cation (Ca, Mg or Ca-Mg) from the sulfate solutions was a very strong driver determining the E_h at the end. Sulfate concentrations, however, did not enhance the de-passivation of ZVI's surface, nor did it contribute to low redox potentials.

4.3.3 Statistical inference of the effect of purging on redox potentials

The change in E_h of the unpurged sulfate solutions were lower compared to the purged sulfate solutions after 6 hours. But, after 16 days the change in E_h of the unpurged and purged sulfate solutions looked similar (Figs. 4.3, 4.4 & 4.5) and their reduction potential values were close to one another (Table 4.2). However, the highly significant difference between the unpurged and purged sulfate solutions, after 6 hours and after 16 days (except for the Ac_Ca-$MgSO_4$ after 16 days), showed that purging DO produced lower reduction potentials (Table 4.3). Purging DO from the solutions was not consequential for the reduction of sulfate. Although the E_h of the solutions varied statistically, they still followed the same trajectory and ended with more or less the same redox potentials.

Table 4.3: Significance of differences in redox potentials between unpurged and purged sulfate solutions[a]

	p-Values	p-Values
Solution	**6 hours**	**16 days**
AC_$CaSO_4$	3.10E-03**	<1.00E-04**
ALK_$CaSO_4$	<1.00E-04**	<1.00E-04**
AC_$MgSO_4$	3.00E-04**	<1.00E-04**
ALK_$MgSO_4$	<1.00E-04**	<1.00E-04**
AC_Ca-$MgSO_4$	8.00E-04**	6.94E-01
ALK_Ca-$MgSO_4$	<1.00E-04**	<1.00E-04**

* = Significant difference (α = 0.01).

** = Highly significant difference (α = 0.05).

a = An unpaired, two-tailed, non-equal variance T-Test was performed on the sulfate solutions. The redox potentials of the UNPURGED (acidic and alkaline) sulfate solutions were compared to the PURGED (acidic and alkaline) sulfate solutions, where each time (6 hours and 16 days) were analysed separately.

4.3.4 Statistical inference of the effect of initial acidity and alkalinity on redox potentials

Zero-valent iron neutralised the acidic sulfate solutions and buffered all of the sulfate solutions (Table 4.2). Furthermore, the E_h of each solution was close to one another over the 16 day period (Figs. 4.3, 4.4 & 4.5). Table 4.4 showed the p-values between redox potentials of the acidic (unpurged & purged) sulfate solutions and the alkaline (unpurged & purged) sulfate solutions. It was discovered, however, that there were highly significant differences between redox potentials, for the initial acidic and alkaline sulfate solutions, after 6 hours and after 16 days. Furthermore, there were consequential differences for the acidic and alkaline $CaSO_4$ solutions, where the initial pH of 8 was advantageous for the lower reduction potential achieved for the ALK_$CaSO_4$ solutions.

Table 4.4: Significance of differences in redox potentials between acidic and alkaline sulfate solutions[a]

	p-Values	p-Values
Solution	**6 hours**	**16 days**
$CaSO_4$_U	1.70E-03**	2.00E-04**
$CaSO_4$_P	<1.00E-04**	1.12E-02**
$MgSO_4$_U	<1.00E-04**	<1.00E-04**
$MgSO_4$_P	<1.00E-04**	1.00E-03**
Ca-$MgSO_4$_U	2.00E-04**	<1.00E-04**
Ca_$MgSO_4$_P	<1.00E-04**	2.15E-04**

* = Significant difference (α = 0.01).

** = Highly significant difference (α = 0.05).

a = An unpaired, two-tailed, non-equal variance T-Test was performed on the sulfate solutions. The redox potentials of the ACIDIC (unpurged and purged) sulfate solutions were compared to the ALKALINE (unpurged and purged) sulfate solutions, where each time (6 hours and 16 days) were analysed separately.

4.3.5 The effect of Ca^{2+}, Mg^{2+} and SO_4^{2-} in sulfate solutions on redox potentials

Fe^0 is not a strong enough electron donor to reduce calcium and magnesium (Liu et al., 2014). Table 4.5 showed the p-values between sulfate solutions containing Ca, Mg and Ca & Mg, that there was a highly significant difference between the solutions. Mg presumably eliminates or inhibits the formation of solid phases that interferes with the electron transfer of ZVI in solution.

Table 4.5: Significance of differences in redox potentials between samples containing Ca^{2+} and/or Mg^{2+}, after 16 days[a]

	p-Values	p-Values	p-Values
Solution	**Ca vs Mg**	**Ca vs Ca-Mg**	**Mg vs Ca-Mg**
Ac_SO4_U	<1.00E-04**	<1.00E-04**	<1.00E-04**
Ac_SO4_P	<1.00E-04**	<1.00E-04**	1.10E-03**
Alk_SO4_U	<1.00E-04**	<1.00E-04**	<1.00E-04**
Alk_SO4_P	<1.00E-04**	<1.00E-04**	<1.00E-04**

* = Significant difference (α = 0.01).

** = Highly significant difference (α = 0.05).

a = An unpaired, two-tailed, non-equal variance T-Test was performed on the sulfate solutions. The redox potentials of the sulfate solutions containing Ca were compared to the solutions containing Mg and Ca-Mg.

4.4 Conclusion

Zero-valent iron reduced the acidic and alkaline DW's below -100 mV within 5 hours. The FeDWs, however, appeared to re-oxidized after 6 hours, and after 16 days their reduction potentials were above >50 mV. In contrast, the sulfate solutions, acidic & alkaline and unpurged & purged, reached reduction potentials well below -200 mV after 16 days. The reason is that when sulfate was added a large amount of electron acceptors were added to each treatment and the transfer of electrons from ZVI to S(VI) is thermodynamically favoured. The purged and unpurged AC_$CaSO_4$ solutions (-55 to -88 mV) were the exceptions and clearly showed that the $CaSO_4$ solutions hindered electron transfer, restricting low redox potential formation.

The type of sulfate solution was the main driver determining end-point redox potentials. Mg^{2+} and combined Ca^{2+}-Mg^{2+} solutions were responsible for the gradual decrease in E_h. In alkaline situations brucite can form and magnesium (brucite, $Mg(OH)_2$) will possibly "poison" $Fe(OH)_2$ precipitation as both have the same structure ($M^n(OH)_n$). Additionally, the $Mg_xFe_{x-1}(OH)_2$ precipitate that formed is not stable and will breakdown. Ca^{2+} however, was responsible for a fluctuating E_h pattern over time. The possible explanation of this pattern was caused by the repeated precipitation and dissolution of gypsum, as a result of reductive decomposition of S(VI) on ZVI surfaces. The combined Ca-$MgSO_4$ solution caused ZVI to induce the lowest redox potentials, while solutions containing only Ca produced the highest redox potentials. Furthermore, purging sulfate solutions had a minor effect on the results in the end. Only slightly lower reduction potentials compared to the unpurged sulfate solutions were measured.

Even though there were negligible differences between pH and EC for the unpurged and purged samples, reactions between ZVI and oxygen, in a ZVI-solution system, is thermodynamically favoured above all other oxidizing agents, mentioned previously. Purging DO in the solutions for the following chapter will still be required.

CHAPTER 5: SULFATE, CALCIUM AND MAGNESIUM REMOVAL BY MICRO ZERO-VALENT IRON

5.1 Introduction

The previous chapters investigated the effectiveness of experimental conditions created to maintain sufficiently reduced conditions.

With that established, the aim of this chapter is to investigate the removal of S, Ca and Mg, by mZVI in $CaSO_4$, $MgSO_4$ and Ca-$MgSO_4$ solutions. It is hypothesized that SO_4 will be sorbed and potentially reduced by mZVI below a pH value of 7, while Ca and Mg will be sorbed by mZVI above a pH value of 7. It was hypothesized that although gypsum might precipitate from the $CaSO_4$ solutions, it was not expected to be stable in the presence of a strong electron donor (ZVI) and will undergo reductive decomposition.

The reduction of SO_4^{2-}, will be accompanied by the oxidation of Fe^0 to ferrous, ferric and/or mixed ferrous/ferric iron phases such as magnetite. This, in turn, can change the ability of zero-valent iron (ZVI) surfaces to act as electron donors in facilitating the reduction of sulfate. Following Fe^0 oxidation is important to understand what is happening in these systems. According to Li et al., (2014) and X-ray powder diffraction (XRD) patterns presented by Fujioka et al., (2016), the oxidation of Fe^0, in acidic and alkaline solutions, resulted in the corrosion products of magnetite (Fe_3O_4), hematite (α-Fe_2O_3) and goethite (α-FeOOH), identified on the ZVI's surface.

This chapter therefore also follows the changes in concentration of dissolved Fe in the sulfate solutions and the Fe(II):Fe(III) ratio of the dissolved Fe.

5.2 Materials and Methodology

5.2.1 The batch sorption procedure

The sulfate solutions with their concentrations and pH values used in Chapter 4 were also prepared for this chapter, with the addition of 3.12 *mM* $CaSO_4$ and $MgSO_4$ solutions at initial pH 4 and 8. The concentrations of 3.12 *mM* $CaSO_4$ and $MgSO_4$ were added to

increase the range of solutions investigated, to lower concentrations discussed in Chapter 2. The solutions that started at pH = 4, at 3.12 *mM*, will be referred to as ac_$CaSO_4$ & ac_$MgSO_4$, while the solutions that started at pH = 8 will be referred to as alk_$CaSO_4$ & alk_$MgSO_4$ respectively. The initially acidic $CaSO_4$, $MgSO_4$ & Ca-$MgSO_4$ solutions at 12.5 *mM* will be referred to as AC_$CaSO_4$, AC_$MgSO_4$ & AC_Ca-$MgSO_4$ while the initially alkaline $CaSO_4$, $MgSO_4$ & Ca-$MgSO_4$ solutions will be referred to as ALK_$CaSO_4$, ALK_$MgSO_4$ & ALK_Ca-$MgSO_4$ respectively. The solutions mentioned above, without ZVI, as well as acidic and alkaline de-ionized water with ZVI (FeDW) were used as controls. Each sample was replicated three times.

The same argon purging procedure was used as described in Chapter 4 on all treatments. A batch equilibration approach was followed, where three samples of each treatment were sacrificed on days 1, 20, 120 and 145 for analyses (Fig. 5.1). The ZVI to solution ratio was 1:40 and the samples were shaken every second day, for 30 minutes, starting from the beginning to the end of the experiment. Ten millilitres of each sample were extracted through a micro filter (0.45 µm) by 50 ml syringes and analysed with inductively coupled plasma atomic emission spectroscopy (ICP-AES) to determine the concentrations of Ca, Mg, Fe and S remaining in solution.

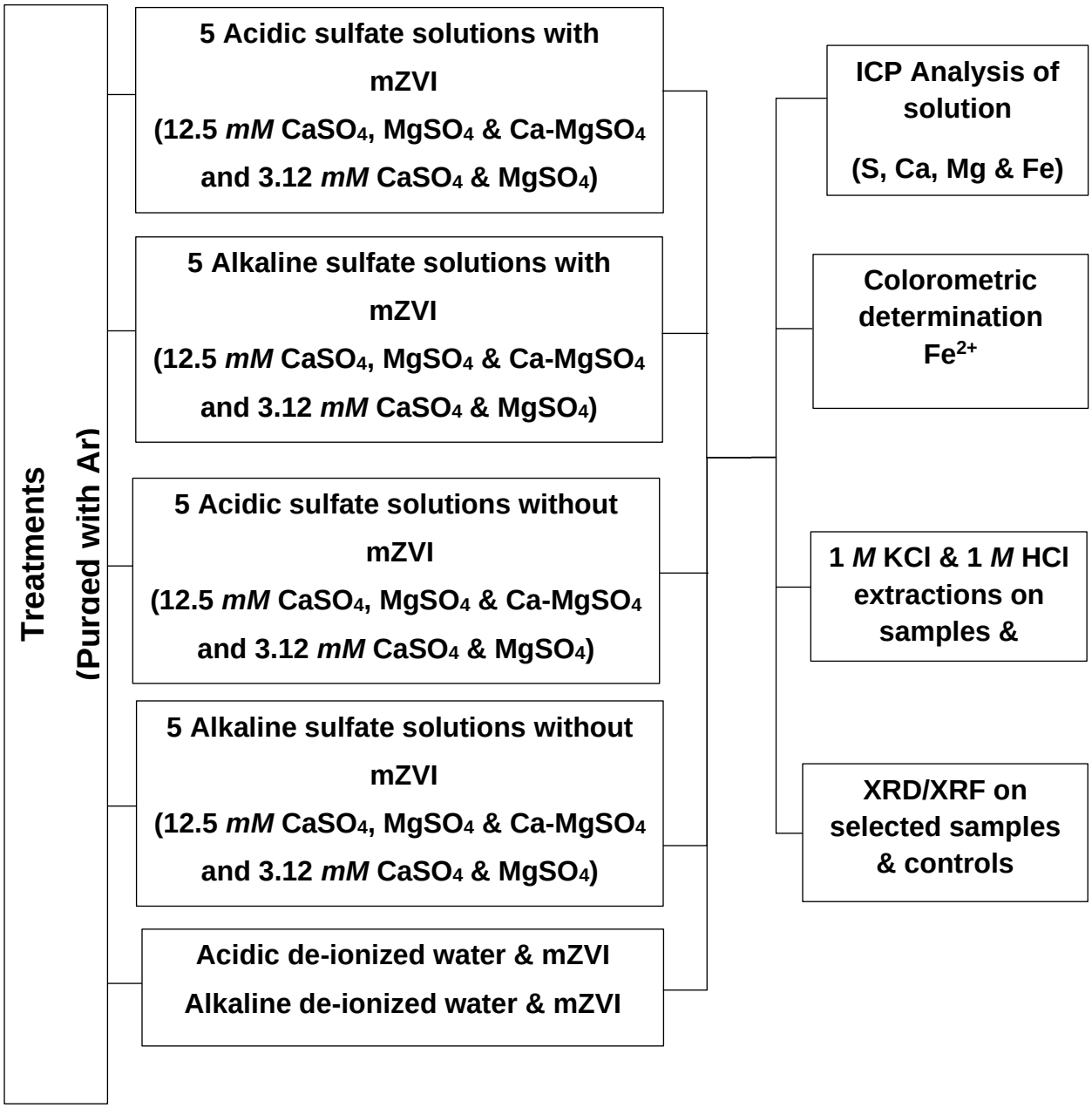

Figure 5.1: Experimental design illustrating the sulfate solutions with their controls and the experiments carried out

5.2.2 Colorometric determination of Fe(II)

At each sampling day another 15 ml of each sample were extracted through a micro filter (0.45 μm) by 50 ml syringes and preserved with 1 ml concentrated HCl (32%), to slow-down oxidation of Fe(II). Dissolved Fe^{2+} from the 15 ml extracts were measured colorimetrically by using the 1,10 - phenanthroline colorimetric method (Eaton et al., 1998). Total dissolved Fe (Fe_{tot}) (Fe^{2+} and Fe^{3+}) was acquired from ICP analysis. Dissolved Fe^{3+} was therefore calculated as the difference between Fe_{tot} and dissolved Fe^{2+}.

5.2.3 Calculating the chemical equilibria of solutions

Mineral phases in the solutions were calculated with the Geochemist Workbench. Mineral saturation indexes (SI), ion activity products (*IAP*) and solubility products (K_{sp}), were calculated with the PHREEQCI model using the minteq.v4 database. The mineral schwertmannite is not included in the PHREEQCI databases but were added to the PHASES block. The solubility product proposed by (Yu et al., 1999) was used (Equation 5.1);

$$Fe_8O_8(OH)_{4.8}(SO_4)_{1.6} + 20.8H^+ \leftrightarrows 8Fe^{3+} + 1.6SO_4^{2-} + 12.8H_2O \qquad K_{sp} = 10 \qquad (5.1)$$

Furthermore, the distribution of ion species, together with their molar concentrations and activities, were also calculated with PHREEQCI. The input file for the sulfate solutions can be viewed in Appendix D.

5.2.4 X-ray powder diffraction (XRD) on selected mZVI samples after mZVI sorption

Micro-ZVI selected from samples, where only the highest concentration of S was removed from the $CaSO_4$, $MgSO_4$ & Ca-$MgSO_4$ solutions, after day 145, were subjected to XRD to determine if secondary minerals, at XRD detectable levels (2%), formed on the ZVI's surface. The selected ZVI powder samples were centrifuged from the solutions and transferred onto filter paper. The samples were rinsed with 99% ethanol, dried and stored until the XRD analysis. Samples were analyzed using a PANalytical X'Pert Pro powder diffractometer in θ-θ configuration with an X'Celerator detector and variable divergence-

and fixed receiving slits with Fe filtered Co-Kα radiation(λ=1.789Å). The phases were identified using Excel software. Errors were reported on the 3 sigma level. X-ray fluorescence was not performed on the mZVI samples as this was not in the scope of this study.

5.3 Results and Discussion

5.3.1 Changes in aqueous sulfur, calcium and magnesium over time

The Fisher's Least Significant Difference (LSD) test showed a statistically significant decrease between initial concentration and the remaining S, Ca & Mg in the solutions, at 3.12 *mM* and 12.5 *mM*, after days 1, 20, 120 & 145 (Appendix C, Tables 1 & 2).

5.3.1.1 The $CaSO_4$ solution at 3.12 mM

It was expected that S sorption would be the result of ZVI reduction in the ac_$CaSO_4$ solution. While Ca sorption would be favoured initially in the alk_$CaSO_4$ solution, followed by S sorption, as the point of zero charge (pzc) for nano-ZVI was reported as 7.9, 6.6, 9.1 and 8.8 (Denis et al., 2019), in $FeSO_4$, $Fe(NO_3)_3$, $FeCl_2$ and $FeCl_3$ solutions respectively. Figures 5.2a and 5.2b depicted the decrease of S and Ca, in the ac_$CaSO_4$ and alk_$CaSO_4$ solutions respectively, during the experiment. Furthermore, Fig. 5.2 shows the results that were subjected to statistical inference and showed that the decreases were statistically significant. Table 5.1 showed the sorption of S and Ca by ZVI in the $CaSO_4$ solutions.

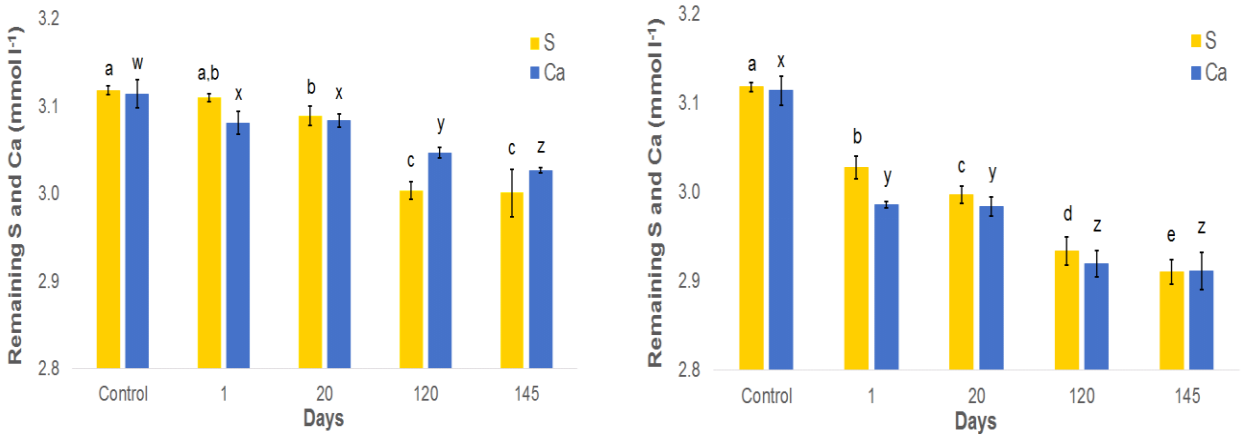

a **b**

Figure 5.2: Decrease in aqueous S & Ca in the (a) ac_$CaSO_4$ and (b) alk_$CaSO_4$ solutions. The least significant difference of S & Ca for (a) are 0.03 & 0.02 and for (b) are 0.02 & 0.03 at a confidence level of 95% (α = 0.05). Error bars represent standard deviations and the letters represent the significant differences between experimental days

Table 5.1: Sorption of S and Ca for the 3.12 *mM* $CaSO_4$ solutions

ac_$CaSO_4$ Sorbed (mmol kg^{-1})						**alk_$CaSO_4$ Sorbed (mmol kg^{-1})**					
Day	**S**	**Ca**	**S/Ca**	**pH**	**E_h[a]**	**Day**	**S**	**Ca**	**S/Ca**	**pH**	**E_h**
1	0.35	1.32	0.27	7.18	-387	1	3.63	5.13	0.71	8.90	-314
20	1.15	1.21	0.95	7.43	-384	**20**	4.83	5.23	0.92	8.08	-309
120	4.59	2.69	1.71	8.05	-278	**120**	7.35	7.80	0.94	8.42	-272
145	4.67	3.50	1.33	8.12	-228	**145**	8.31	8.11	1.02	8.37	-258

a = Redox potentials reported in mV.

The sorption of S and Ca were calculated using Equation 5.2;

$$C_m = [(C_i - C_f)*V]/m \quad (5.2)$$

where C_m is the concentration per mass mZVI (mmol kg^{-1}), of removed S and Ca from the solution. C_i is the initial concentration of the solution (*mM*), C_f is the final concentration measured after each experimental day (*mM*). V is the volume of the sample used (0.04 l) and m is the amount, in kg, of mZVI used (0.001 kg).

Figure 5.2a and Table 5.1 showed that for the ac_$CaSO_4$ solution, the sorption of aqueous S was less than Ca, for the first 20 days. ZVI oxidation generated alkalinity (Tables 4.1 & 4.2, Chapter 4) as the pH increased from 4 to 7.18 in one day. The reaction occurred at a remarkable pace, under 24 hours, and was an indication of fast initial electron transfer between ZVI and the electron acceptor SO_4^{2-}. The pH was buffered between 7 & 8 for the rest of the experiment and the E_h showed a gradual increase, however, conditions were optimal for pyrite precipitation (Fig. 5.3).

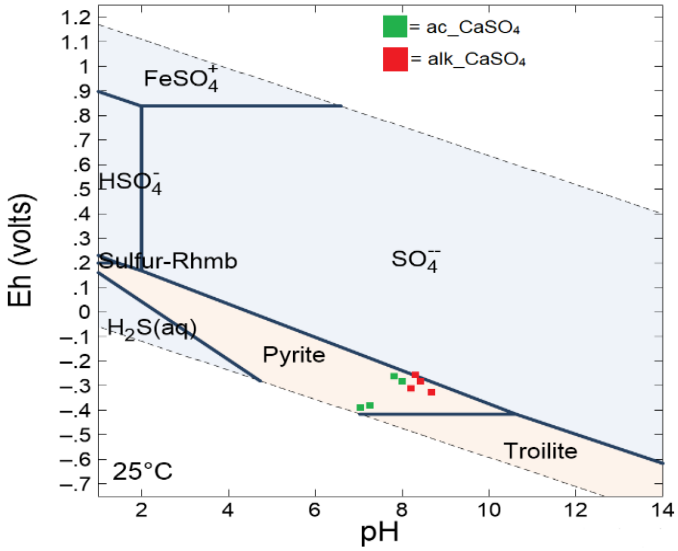

Figure 5.3: The redox and pH data, (green and red points represent data of day 1, 20, 120 & 145), of the ac_$CaSO_4$ and alk_$CaSO_4$ superimposed on a E_h-pH (Pourbaix) diagram for the Fe-Ca-S system. The predominance areas for the various sulfur phases in the E_h–pH diagram is based for the following conditions: soluble Fe^{2+} activity is 10^{-6}; SO_4^{2-} activity is 10^{-4}; Ca^{2+} activity is 10^{-3}; activity of H_2O is unity; T = 25°C; and P = 0.101 MPa. Activities were modelled using the Geochemist Workbench software

Assuming ideal conditions were created for SO_4^{2-} reduction and pyrite surface precipitation on ZVI surfaces, SO_4^{2-} will reduce to S^{2-} and precipitate on the surface of ZVI, resulting in the oxidation of Fe^0 to Fe^{2+} (Equation 5.3);

$$4Fe^0_{(s)} + SO_4^{2-}{}_{(aq)} + 8H^+_{(aq)} \leftrightarrows >Fe^{II}\text{-}S^{1.67-}_{(surf)} + 3Fe^{2+}_{(aq)} + 4H_2O_{(l)} \quad (5.3)$$

Butler & Rickard (2000) stated that in due course oxidation of amorphous FeS (S^{2-}) by aqueous H_2S will produce FeS_2 (S^{1-}) (Equation 5.4);

$$>Fe^{II}\text{-}S^{1.67-}_{(surf)} + H_2S_{(aq)} \leftrightarrows >Fe^{II}\text{-}S_2^{1.67-}{}_{(surf)} + H_{2(g)} \quad (5.4)$$

Followed by pyrite induced Ca^{2+} sorption (Equation 5.5);

$$>Fe^{II}\text{-}S_2^{1.67-}{}_{(surf)} + Ca^{2+}_{(aq)} \leftrightarrows >Fe^{II}\text{-}S_2\text{-}Ca^{0.33+}_{(surf)} \quad (5.5)$$

Iron oxide formation was also possible either as a precursor, in serie or parallel with pyrite precipitation from the additional Fe^{2+} that formed in Equation 5.3. The iron oxides were expected to show cation affinity in alkaline solutions with the pzc reported between 6.8 - 7.7 for magnetite, goethite and hematite (Mansour et al., 2009). Sorption mechanisms of S and Ca on pyrite or magnetite surfaces could not be directly determined with the experimental set-up used. However, Table 5.2 showed that apart from dissolved Fe^{2+}, Fe^{3+} was also present which is evidence magnetite or ferric oxides were present. Therefore, surface reactions involving generic A-type functional groups; $>Fe^{II}\text{-}OH^{0.33-}$ and/or $>Fe^{III}\text{-}OH^{0.5-}$, were possible for the ac_$CaSO_4$ solution as well as the other solutions (Equation 5.6a and/or Equation 5.6b).

$$>Fe^{II}\text{-}OH^{0.33-}_{(surf)} + Ca^{2+}_{(aq)} \leftrightarrows >Fe^{II}\text{-}OHCa^{1.67+}_{(surf)} \quad (5.6a)$$

$$>Fe^{III}\text{-}OH^{0.5-}_{(surf)} + Ca^{2+}_{(aq)} \leftrightarrows >Fe^{III}\text{-}OHCa^{1.5+}_{(surf)} \quad (5.6b)$$

Followed by the subsequent sorption of SO_4^{2-} (Equation 5.7a and/or 5.7b);

$$>Fe^{II}\text{-}OHCa^{1.67+}_{(surf)} + SO_4^{2-}{}_{(aq)} \leftrightarrows Fe^{II}\text{-}OHCaSO_4^{0.33-}{}_{(surf)} \quad (5.7a)$$

$$>Fe^{III}\text{-}OHCa^{1.5+}_{(surf)} + SO_4^{2-}{}_{(aq)} \leftrightarrows Fe^{III}\text{-}OHCaSO_4^{0.5-}{}_{(surf)} \quad (5.7b)$$

However, it is also possible initially when the pH was still low that the removal by iron oxides could have started with SO_4^{2-} sorption (Equation 5.8a and/or Equation 5.8b) followed by Ca^{2+} sorption.

$$>Fe^{II}\text{-}OH_2^{0.33+}_{(surf)} + SO_4^{2-}{}_{(aq)} \leftrightarrows >FeOSO_3^{1.67-}{}_{(surf)} + H_2O_{(l)} \quad (5.8a)$$

$$>Fe^{III}\text{-}OH_2^{0.5+}_{(surf)} + SO_4^{2-}{}_{(aq)} \leftrightarrows >FeOSO_3^{1.5-}{}_{(surf)} + H_2O_{(l)} \quad (5.8b)$$

All the proposed Ca or S induced sorption reactions involving these functional groups, on net, will most likely result in equimolar removal of Ca^{2+} and SO_4^{2-} from solution, regardless

of the surface being net negative or net positive. The S/Ca stoichiometry changes during the experiment can therefore not be explained by these surface sorption reactions alone. At the low measured redox potentials, S(VI) will be meta-stable and expected to be highly susceptible to reduction. Therefore, any sorption and precipitation mechanisms (e.g., gypsum precipitation) that involve SO_4^{2-} will be meta-stable. After the 20th day the pH increased to 7.45 and at this stage, with the low redox potential, it seemed that sorption/reduction/precipitation processes are actively favouring S over Ca removal from the ac_$CaSO_4$ solutions. After day 120 and 145 S sorption exceeded Ca sorption and ended at S/Ca = 1.33.

For the ac_$CaSO_4$ solution there was a strong correlation between the sorption of S & Ca and increasing pH, as well as with increasing E_h, (Figs. 5.4a & 5.4b). This, along with the wider S/Ca ratio, suggested that the reduction of SO_4^{2-}, and precipitation as pyrite, was most likely the dominant mechanism for S removal. Weerasooriya & Tobschall (2005) found the pzc of pyrite to be as low as 1.7. Ca is therefore expected to be sorbed by pyrite surfaces as shown in Equation 5.5. The relationships between Ca^{2+} and pH, as well as Ca^{2+} and redox potential, are therefore indirect. This also explains the linear relationship between S and Ca sorption (Fig. 5.5).

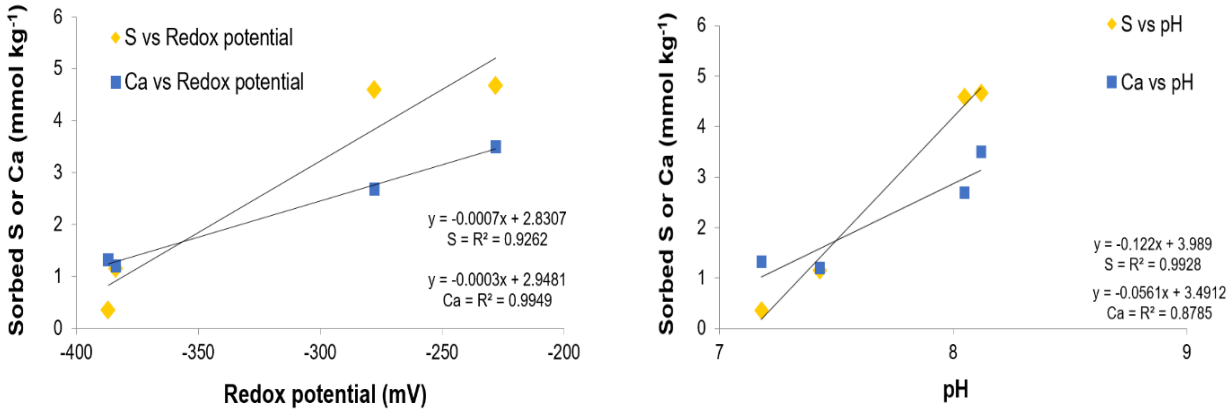

a **b**

Figure 5.4: Correlation of S and Ca sorption as a function of (a) pH and (b) redox potential for the ac_$CaSO_4$ solution

Overall, the sorption of aqueous S and Ca was greater for the alk_$CaSO_4$ solution than for the ac_$CaSO_4$ solution (Fig. 5.5 & Table 5.1). The distinct difference between the ac_CaSO4 and alk_CaSO4 solutions was also the fact that the stoichiometric ratio for S/Ca of the alk_$CaSO_4$ solution was close to unity through-out the experiment. Which suggests possible co-sorption and/or gypsum precipitation. However, SO_4^{2-} and therefore gypsum was not exepected to be stable at these low redox pontentials for long. Saturation indices also showed it was unlikely that gypsum precipitation occurred through homogenous nucleation from the ac_$CaSO_4$ nor alk_$CaSO_4$ solution (Appendix D, Table D.1). However, it is well established that heterogeneous nucleation and surface precipitation of minerals can occur even when the bulk solution is unsaturated (Essington, 2004; Sparks, 2003). The $CaSO_4$ solutions exhibited a characteristic fluctuation in E_h (Chapter 4, Figure 4.3). It is hypothesised that gypsum surface precipitation was possibly kinetically favoured (as discussed in Chapter 4) which temporarily pacified the surface of ZVI, limiting electron transfer. However, because it is meta-stable under the reduced conditions created, it dissolved again. Thus creating the observed fluctuation in redox potential over time.

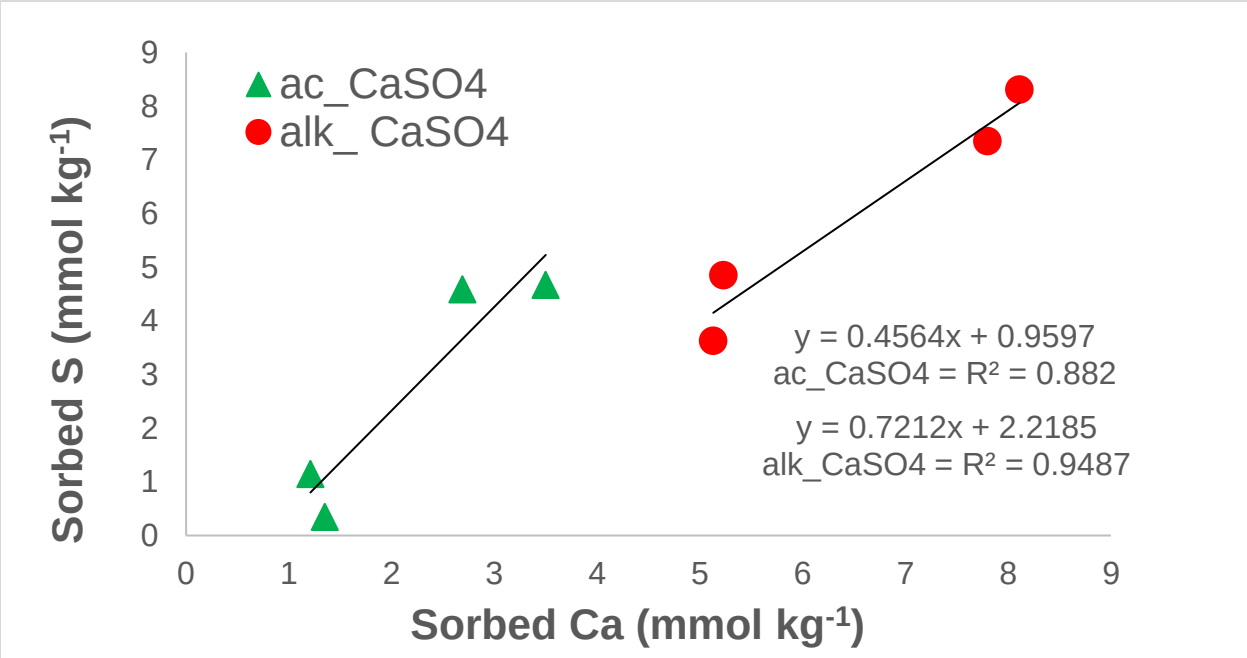

Figure 5.5: Correlation between S and Ca sorption for the ac_$CaSO_4$ and alk_$CaSO_4$ solution

The pH of the solution was higher during the experiment than for the ac_$CaSO_4$ solution and ranged between 8 and 8.9. The pH and low redox potential were also advantageous for pyrite precipitation (Fig. 5.3) and pyrite induced Ca^{2+} sorption. Equations 5.3 to 5.8 were proposed as possible mechanisms for S sorption and surface pyrite formation, as well as Ca sorption, during the experiment.

There was a weak correlation between the sorption of S & Ca and the increase in pH for the alk_$CaSO_4$ solution (Fig. 5.6a) and showed a non-linear tendency between sorption and pH. There was, however, a correlation between the sorption of S & Ca and the increase in E_h (Fig. 5.6b) and suggested the sorption of S by iron oxides which stability increased with increasing redox potential. The initial alkalinity of the solution was advantageous for sorption of Ca by pH dependant surfaces, however, Ca was most likely indirectly related to the E_h.

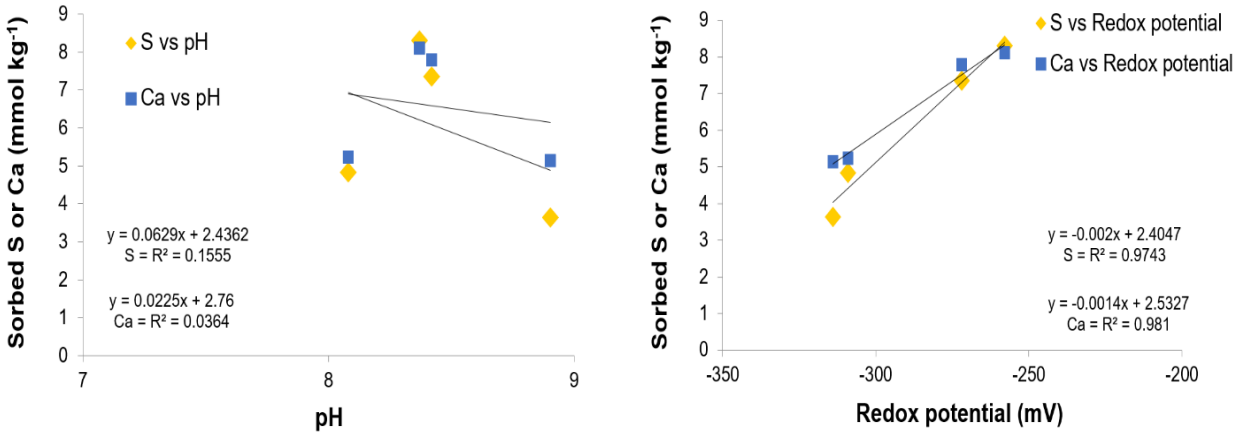

a **b**

Figure 5.6: Correlation of S and Ca sorption as a function of (a) pH (b) redox potential for the alk_$CaSO_4$ solution

Table 5.2 showed the total dissolved Fe (Fe_{Tot}), dissolved ferrous (Fe^{2+}) and dissolved ferric (Fe^{3+}) ions, together with the Fe^{3+}/Fe_{Tot} molar fraction, in the ac_$CaSO_4$ and alk_$CaSO_4$ solutions. Ferrous, ferric and sulfate ions orients the condensation process in the formation of solid Fe phases (Jolivet et al., 2004; Ruby et al., 2006). Furthermore,

ferrous and ferric iron can occur as oxides or sulphides as discussed and by examining the parameters provided an idea can be established as to where the equilibrium lies.

The corrosion of ZVI was greater in the alk_$CaSO_4$ solution compared to the ac_$CaSO_4$ solution as the alk_$CaSO_4$ solution contained a higher dissolved Fe concentration (Table 5.2). Furthermore, the alk_$CaSO_4$, in particular, shows Fe^{3+} enrichment. For both the ac_$CaSO_4$ and alk_$CaSO_4$ solutions, the Fe^{3+}/Fe_{Tot} ratio in both solutions were ≤0.4 during experimentation because of the low redox potentials created. Furthermore, even under these low redox potentials, ferrous iron oxidized to ferric iron, described by the Schikorr reaction (Chapter 4, Eq. 4.4). Reduced conditions inhibited the majority of Fe^{2+} to be oxidized to Fe^{3+} which suggested that Fe^{2+}:Fe^{3+} rich minerals such as magnetite and green rust were more likely to precipitate rather than pure ferric or ferrous oxides.

Table 5.2: Dissolved Fe in the 3.12 *mM* $CaSO_4$ solutions

ac_$CaSO_4$	**Fe_{Tot}[a]**	**Fe^{2+}**	**Fe^{3+}**	**Fe^{3+}/Fe_{Tot}**
Day 1	0.13	0.08 (± 3.30E-04)[b]	0.04 (± 1.90E-04)	0.34
Day 20	0.13	0.08 (± 0.00)	0.05 (± 1.90E-05)	0.37
Day 120	0.14	0.08 (± 7.50E-04)	0.06 (± 2.80E-04)	0.40
Day 145	0.20	0.08 (± 4.60E-04)	0.12 (± 3.80E-04)	0.59
alk_$CaSO_4$	**Fe_{Tot}**	**Fe^{2+}**	**Fe^{3+}**	**Fe^{3+}/Fe_{Tot}**
Day 1	0.31	0.28 (± 3.70E-04)	0.02 (± 5.80E-04)	0.08
Day 20	0.34	0.32 (± 6.50E-04)	0.02 (± 5.90E-04)	0.07
Day 120	0.35	0.34 (± 0.00)	0.01 (± 3.00E-04)	0.03
Day 145	0.36	0.35 (± 3.70E-04)	0.01 (± 2.00E-04)	0.02

a = FeTot, Fe^{2+} and Fe^{3+} reported in mmol kg^{-1}.
b = Value in brackets is standard deviation of samples.

There was no correlation between S & Ca sorption and dissolved Fe^{2+} (Fig. 5.7a) for the ac_$CaSO_4$ solution, with the concentration of dissolved Fe^{2+} remaining constant during the experiment. There was, however, a correlation between S sorption and dissolved Fe^{3+}, with a stronger correlation observed between Ca sorption and dissolved Fe^{3+}. The ferric concentration was higher for the ac_$CaSO_4$ and showed an increase over time, which also supported the increase of E_h. Oxidation of Fe^{2+} was slow as the pH increased because of low redox potentials during the experiment.

In contrast to the ac_$CaSO_4$ solution, the alk_$CaSO_4$ solution showed strong correlations between the sorption of S & Ca and dissolved Fe^{2+}. There were also strong correlations between the sorption of S & Ca and dissolved Fe^{3+} (Fig. 5.7b). Another notable difference was that the ac_$CaSO_4$ solution showed an increasing trend in Fe^{3+}, while the alk_$CaSO_4$ showed a decreasing trend. The alk_$CaSO_4$ solution was clearly more conducive for S removal from solution. However, the reduction of sulfate means other constituents must have been oxidized. The higher Fe^{2+} concentration of the alk_$CaSO_4$ solution suggests that the electron donor was Fe^0 rather than Fe^{2+}. In the case of the ac_$CaSO_4$ solution, the higher Fe^{3+} concentration suggests that Fe^{2+} was an important electron donor, as well.

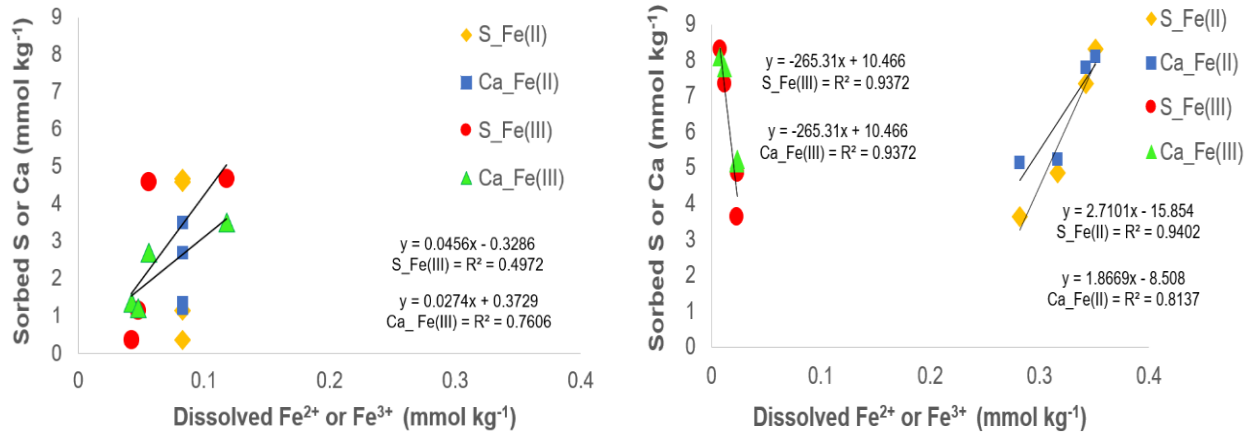

a **b**

Figure 5.7: Sorption of S or Ca vs dissolved Fe^{2+} and Fe^{3+} for the (a) ac_$CaSO_4$ and (b) alk_$CaSO_4$ solution

5.3.1.2 The $CaSO_4$ solution at 12.5 mM

Gypsum precipitation occurs at higher concentrations (±14.7 *mM* at 25°C), and it was expected that the change for heterogeneous nucleation and gypsum precipitation would be greater. Figures 5.8a & 5.8b depicted the decrease of S and Ca, in the AC_$CaSO_4$ and ALK_$CaSO_4$ solutions, respectively. Furthermore, Fig. 5.8 is a direct analysis that showed the decreases were statistically significant and Table 5.3 showed the sorption of S and Ca by ZVI in the $CaSO_4$ solutions.

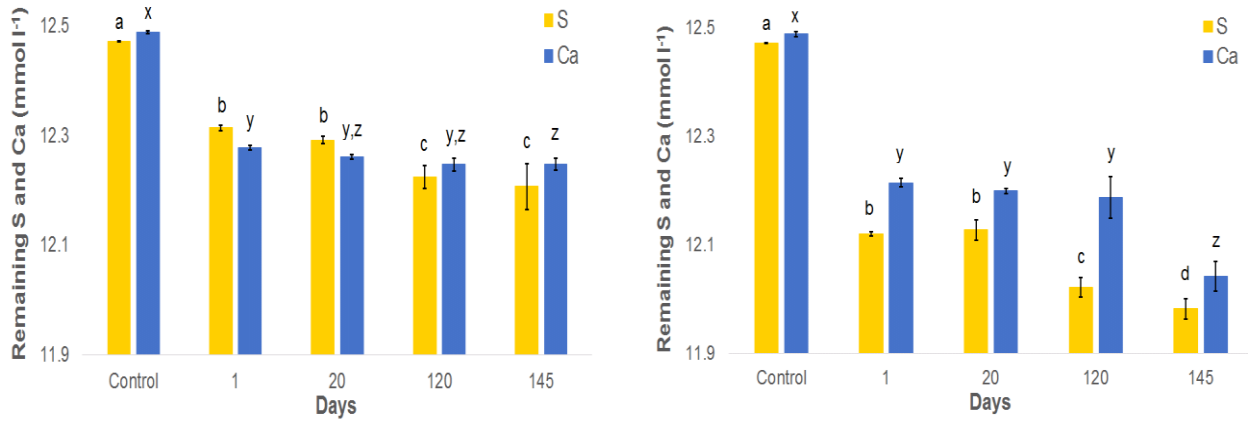

Figure 5.8: Decrease in aqueous S & Ca in the (a) AC_$CaSO_4$ and (b) ALK_$CaSO_4$ solutions. The least significant difference of S & Ca for (a) are 0.04 & 0.02 and in (b) are 0.03 & 0.04 at a confidence level of 95% (α = 0.05). Error bars represent standard deviations and the letters represent the significant differences between experimental days

Table 5.3: Sorption of S and Ca for the 12.5 *mM* $CaSO_4$ solutions

AC_$CaSO_4$ Sorbed (mmol kg^{-1})						ALK_$CaSO_4$ Sorbed (mmol kg^{-1})					
Day	**S**	**Ca**	**S/Ca**	**pH**	**E_h[a]**	**Day**	**S**	**Ca**	**S/Ca**	**pH**	**E_h**
1	6.31	8.42	0.75	7.12	-400	**1**	14.1	11.0	1.28	8.87	-318
20	7.19	9.08	0.79	7.39	-388	**20**	13.8	11.6	1.19	8.10	-312
120	9.90	9.63	1.03	8.09	-328	**120**	18.0	12.0	1.50	8.52	-311
145	10.6	9.68	1.22	8.11	-330	**145**	19.6	17.9	1.09	8.46	-298

a = Redox potentials reported in mV.

Figure 5.8a and Table 5.3 showed that for the AC_$CaSO_4$ the sorption of S and Ca was more than double the ac_$CaSO_4$ solution and greater, but not more than double, the alk_$CaSO_4$ solution. Sorption of S was less than Ca after the 1st day as the pH increased from 4 to 7.12. Furthermore, the redox potential was below -300 mV during the experiment and ideal conditions were created for sulfate sorption/reduction and pyrite precipitation, as shown in the Pourbaix diagram (Fig. 5.9). The plotted pH and E_h points of each day suggested that the other Fe phases identified with XRD (Fig. 5.14) were possibly meta-stable and with time, if redox conditions persist, will transform to pyrite.

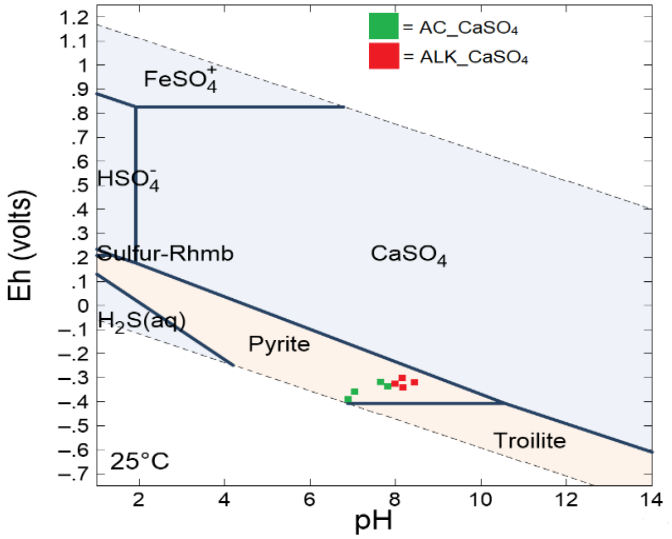

Figure 5.9: The redox and pH data, (green and red points represent data for day 1, 20, 120 & 145), of the AC_$CaSO_4$ and ALK_$CaSO_4$ superimposed on a E_h-pH (Pourbaix) diagram for the Fe-Ca-S system. The predominance areas for the various sulfur phases in the E_h–pH diagram is based for the following conditions: soluble Fe^{2+} activity is 10^{-6}; SO_4^{2-} activity is 10^{-3}; Ca^{2+} activity is 10^{-3}; activity of H_2O is unity; T = 25°C; and P = 0.101 MPa. MPa. Activities were modelled using the Geochemist Workbench software

The pH was buffered between 7.12 and 8.11 during the experiment. The sorption mechanisms proposed for the A-type functional groups, described in 5.3.1, is also proposed for this section. Sulfate sorption and reduction by ZVI occurred (Eqs. 5.3 & 5.4), inducing Ca^{2+} sorption (Eq. 5.5). Under alkaline conditions, Ca^{2+} and SO_4^{2-} sorption was also possible by Fe oxides (Eqs. 5.7 to 5.8) that potentially precipitated on ZVI's surface. However, as discussed, the proposed sorption reactions involved, on net, result in the removal of Ca^{2+} and SO_4^{2-} from solution, regardless of the surface charge. The sorption of Ca was still greater than S after day 20, however, after day 120 and 145 there was little to no more sorption of Ca and as a result, sorption of S surpassed Ca. The S:Ca stoichiometry increase during the experiment was most likely due to pyrite precipitation.

The AC_$CaSO_4$ solution showed a strong correlation between the sorption of S and pH, as well as the decrease in E_h. There was, however, a weak correlation between the sorption of Ca and pH, as well as the increase in E_h (Fig. 5.10a and 5.10b). It therefore

seemed that sorption of S was dependent on pH and redox potential, while Ca sorption was not. However, Ca and S sorption still showed a relationship (Fig. 5.11). This suggested that the reduction of SO_4^{2-}, and precipitation as pyrite, was most likely the dominant mechanism for S removal.

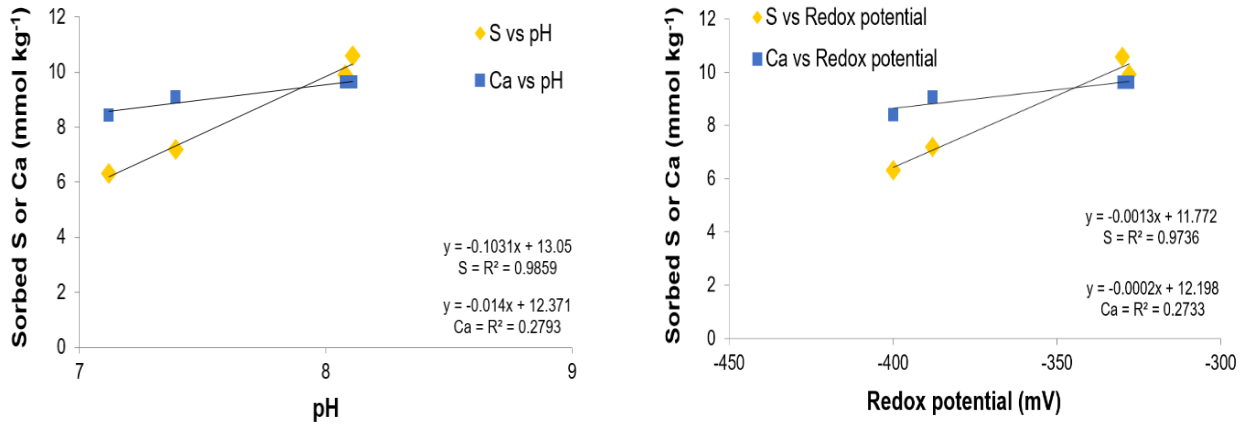

a **b**

Figure 5.10: Correlation of S and Ca sorption as a function of (a) pH and (b) redox potential for the AC_$CaSO_4$ solution

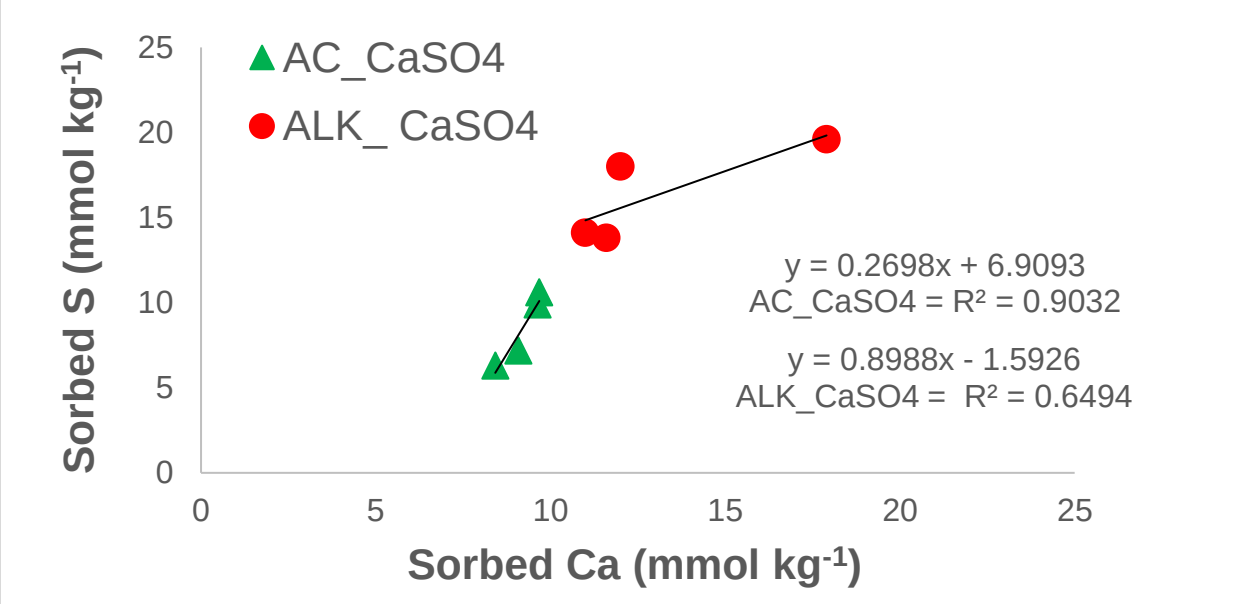

Figure 5.11: Correlation between S and Ca sorption for the AC_$CaSO_4$ and ALK_$CaSO_4$ solutions

For the ALK_$CaSO_4$ solution (Fig. 5.11 & Table 5.3) the sorption of S was greater than Ca. The pH was buffered at a higher pH range of 8.1 and 8.87. The pH, together with the redox potential, which stayed close to -300 mV during the experiment, created ideal conditions for pyrite precipitation (Fig. 5.9). The same sorption mechanisms for sulfate sorption and subsequent reduction thereof, followed by Ca sorption is proposed for the ALK_$CaSO_4$ solution, as well (Eqs. 5.3 to 5.8). For the ALK_$CaSO_4$ solution the stoichiometric ratio of S and Ca approached unity similar to the alk_$CaSO_4$ solution, which suggests possible co-sorption and/or gypsum precipitation, as discussed for the alk_$CaSO_4$ solution. However, SO_4^{2-} and therefore gypsum was also not expected to be stable at these low redox pontentials. The same redox potential fluctuations were seen therefore. Gypsum possibly formed but dissolved again and SO_4^{2-} reduce and precipite as pyrite, because no gypsum was detected with XRD, however, pyrite was (Fig. 5.12).

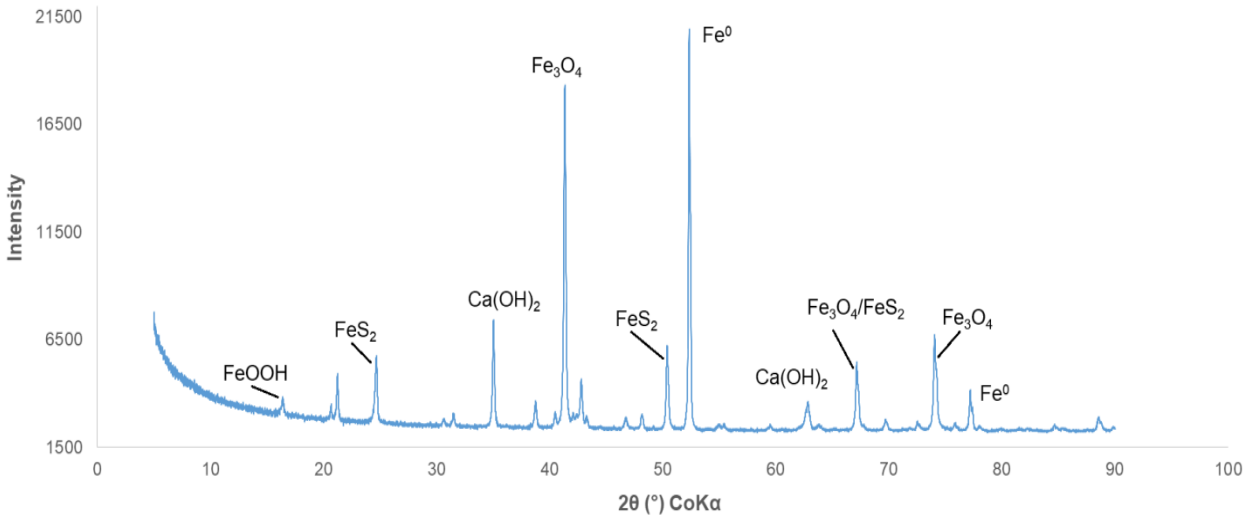

Figure 5.12: XRD of mZVI powder, taken from the ALK_$CaSO_4$ solution after 145 days

A variety of Fe phases formed in the ALK_$CaSO_4$ solution (Fig. 5.12), showing that the system was not at a thermodynamic equilibrium. Pyrite was identified at XRD peaks of 24°, 52° and 67° which related to XRD data of natural pyrite presented by Fathinia et al. (2015). The other phases that precipitated on the ZVI's surface were identified as goethite, magnetite and $Ca(OH)_2$ based on the d-spacing reported by (Furukawa et al., 2002; Filip et al., 2014; Fujioka et al., 2016; Ghica et al., 2016; Mu et al., 2017).

There were weak correlations between the sorption of S & Ca and increasing pH (Fig. 5.13a). There was a strong correlation between the sorption of S & Ca and increasing E_h (Fig. 5.13b), however, it shows that the E_h did not benefit sorption. This suggested, just as in 5.3.1.1, that there was mutual sorption of S, subsequent reduction, and precipitation as pyrite. Calcium was indirectly related to the increase in E_h as sorption was enhanced due to pyrite formation and initial alkalinity of solution.

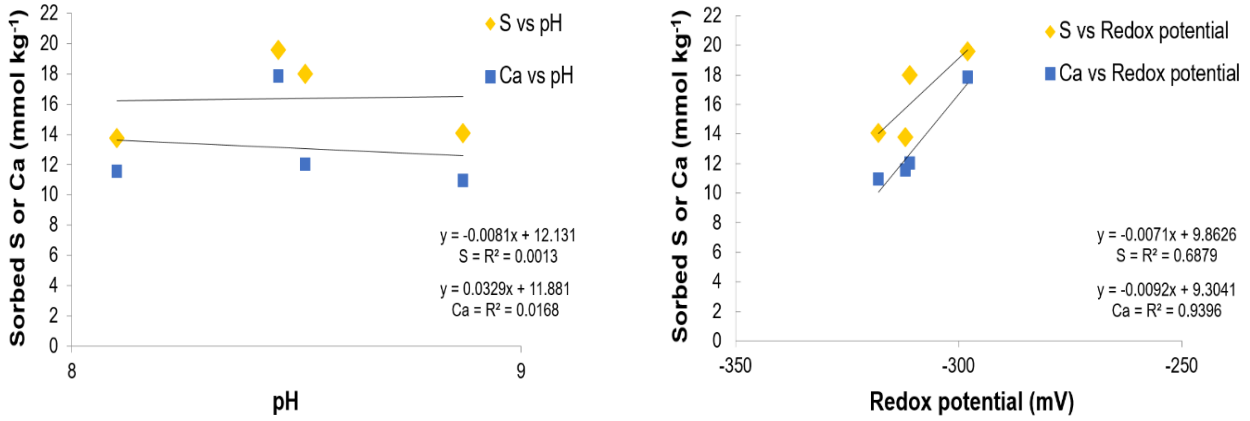

a **b**

Figure 5.13: Correlation of S and Ca sorption as a function of (a) pH and (b) redox potential for the ALK_$CaSO_4$ solution

The main differences for the acidic and alkaline treatments were that the sorption of S and Ca at 12.5 *mM* (AC_$CaSO_4$ and ALK_$CASO_4$) were more than double the sorption of S and Ca at 3.12 *mM* (ac_$CaSO_4$ & alk_$CaSO_4$).

The pH, for both solutions, was buffered near ±8 which meant that ZVI went through the same cycle (the cycle observed for the $CaSO_4$ solutions at 3.12 *mM*). However, with the higher concentration of $CaSO_4$ (of 12.5 *mM*) an increase in the dissolved Fe was observed for both solutions (Table 5.4) compared to the solutions at 3.12 *mM* (Table 5.2). There were 4 times more electron acceptors [SO_4^{2-}] in the 12.5 *mM* solutions which contributed to the increase of ZVI oxidation and dissolved Fe. Higher concentrations of both dissolved Fe^{2+} and Fe^{3+} suggested conditions for magnetite precipitation.

Table 5.4: Dissolved Fe in the 12.5 *mM* $CaSO_4$ solutions

AC_$CaSO_4$	**Fe_{Tot}[a]**	**Fe^{2+}**	**Fe^{3+}**	**Fe^{3+}/Fe_{Tot}**
Day 1	1.47	0.93 (± 3.70E-04)[b]	0.54 (± 3.4E-03)	0.36
Day 20	1.38	0.94 (± 6.50E-04)	0.45 (± 4.8E-04)	0.32
Day 120	1.38	0.96 (± 3.70E-04)	0.43 (± 6.4E-04)	0.31
Day 145	1.39	0.98 (± 3.70E-04)	0.41 (± 7.9E-04)	0.29
ALK_$CaSO_4$	**FeTot**	**Fe^{2+}**	**Fe^{3+}**	**Fe^{3+}/Fe_{Tot}**
Day 1	0.79	0.64 (± 4.50E-03)	0.15 (± 2.20E-03)	0.37
Day 20	0.73	0.65 (± 6.50E-04)	0.08 (± 1.30E-03)	0.34
Day 120	0.78	0.69 (± 4.50E-04)	0.09 (± 4.60E-04)	0.27
Day 145	0.79	0.76 (± 1.00E-04)	0.03 (± 1.10E-03)	0.29

a = Fe_{Tot}, Fe^{2+} and Fe^{3+} reported in mmol kg^{-1}.
b = Value in brackets is standard deviation of samples.

The greater concentration of dissolved Fe_{Tot} in the AC_$CaSO_4$ solution (Table 5.4) showed that the pH, before 24 hours, was more advantageous in dissolving Fe from the ZVI, because electron transfer in solution was apparently stronger compared to the ALK_$CaSO_4$ solution. However, the Fe^{3+}/Fe_{Tot} ratio and its over-all decrease, for the AC_$CaSO_4$ solution, during the experiment was similar to the ALK_$CaSO_4$ solution. The concentration of Fe^{2+} did not increase substantially after the first 24 hours, further suggesting that the initial pH had the biggest influence in corroding ZVI. In the AC_$CaSO_4$ solution oxidation to Fe^{2+} occurred slowly as the pH increased and because of low reduction potentials that were also achieved after day 1 (Fig. 5.13b). For the ALK_$CaSO_4$ solution, however, Fe^{3+} was considerably lower than the Fe^{3+} in the AC_$CaSO_4$ solution as oxidation of Fe^{2+} to Fe^{3+} was restricted because of the higher pH and low redox potentials achieved during the experiment.

There were strong correlations between S & Ca sorption and dissolved Fe^{2+} for both AC_$CaSO_4$ and ALK_$CaSO_4$ solution (Fig. 5.14a). There were also strong correlations between S & Ca sorption and dissolved Fe^{3+} for the AC_$CaSO_4$ solution, however the correlations observed for the ALK_$CaSO_4$ solution were not as strong (Fig. 5.14b). More Fe^{3+} correlated to less sorption of S and Ca, or in other words, a strong link was seen between increased sorption of S & Ca and increase in dissolved Fe^{2+}.

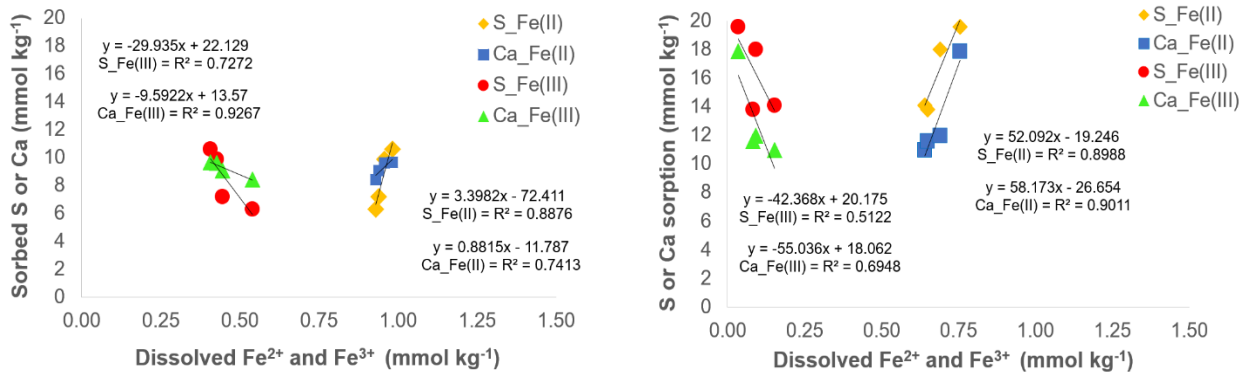

a **b**

Figure 5.14: Sorption of S & Ca vs dissolved Fe^{2+} and Fe^{3+} for the (a) AC_$CaSO_4$ and (b) ALK_$CaSO_4$ solution

5.3.1.3 The $MgSO_4$ solution at 3.12 mM

The $MgSO_4$ solutions created lower E_h values compared to the $CaSO_4$ solutions (Chapter 4). This, in turn, represented more ideal conditions for the reduction of SO_4^{2-}. The expectation was, therefore, that there would be a greater sorption of S, compared to the solutions containing S and Ca. For the $CaSO_4$ solutions the relationship between Fe^{2+} and Ca^{2+} sorption suggested possible FeS_2 precipitation induces Ca sorption. Similar was expected for Mg. Furthermore, it was expected that ZVI will buffer the pH between 7 and 9, for the ac_$MgSO_4$ and alk_$MgSO_4$ solution, where cation sorption was expected to be the most pronounced by variably charged surfaces. Figures 5.15a & 5.15b depicted the decrease of S and Mg, in the ac_$MgSO_4$ and alk_$MgSO_4$ solutions, respectively. Furthermore, Figure 5.15 is a direct solution analysis and showed the decreases were statistically significant and Table 5.5 showed the sorption of S and Mg by ZVI in the $MgSO_4$ solutions.

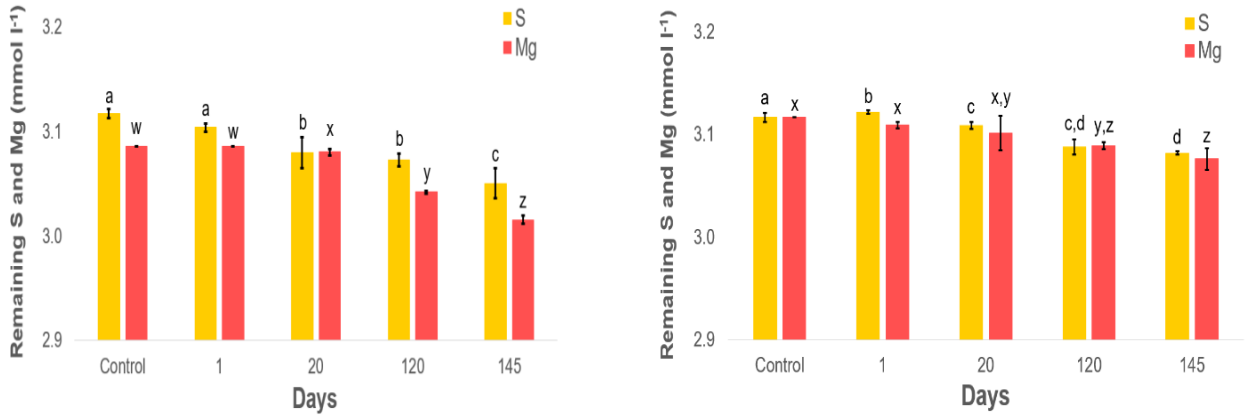

a **b**

Figure 5.15: Change in aqueous S & Mg in the (a) ac_$MgSO_4$ and (b) alk_$MgSO_4$ solutions. The least significant difference of S & Mg for (a) are 0.02 & 0.004 and in (b) are 0.008 & 0.02 at a confidence level of 95% (α = 0.05). Error bars represent standard deviations and the letters represent the significant differences between experimental days

Table 5.5: Sorption of S and Mg for the 3.12 *mM* $MgSO_4$ solutions

ac_$MgSO_4$ Sorbed (mmol kg^{-1})						alk_$MgSO_4$ Sorbed (mmol kg^{-1})					
Day	**S**	**Mg**	**S/Mg**	**pH**	**E_h[a]**	**Day**	**S**	**Mg**	**S/Mg**	**pH**	**E_h**
1	0.52	0.01	50.0	6.86	-313	**1**	0.00	0.31	1.26	7.88	-339
20	1.49	0.23	6.48	6.51	-319	**20**	1.02	0.62	1.65	7.03	-334
120	1.76	1.76	1.00	6.89	-324	**120**	1.15	1.12	1.03	7.19	-343
145	2.66	2.82	0.94	7.01	-340	**145**	1.39	1.63	0.85	7.22	-356

a = Redox potentials reported in mV.

The ac_$MgSO_4$ solution experienced, initially, a more rapid removal of S compared to Mg in the first 20 days (Fig. 5.15a & Table 5.5). The solution was at pH = 4 when prepared, however, the rapid rise of pH to 6.86 after 24 hours shows the strong buffering and kinetically fast initial oxidation of ZVI. This coincided with stronger sulfate sorption. Overall sorption of S & Mg for the ac_$MgSO_4$ solution and alk_$MgSO_4$ solution was lower than the ac_$CaSO_4$ solution (4.67 mmol kg^{-1} S & 3.5 mmol kg^{-1} Ca) and alk_$MgSO_4$ solution (8.31 mmol kg^{-1} S & 3.5 mmol kg^{-1} Ca). The slightly acidic conditions and very low E_h during the experiment were ideal for pyrite precipitation for the ac_$MgSO_4$ solution (Fig. 5.16).

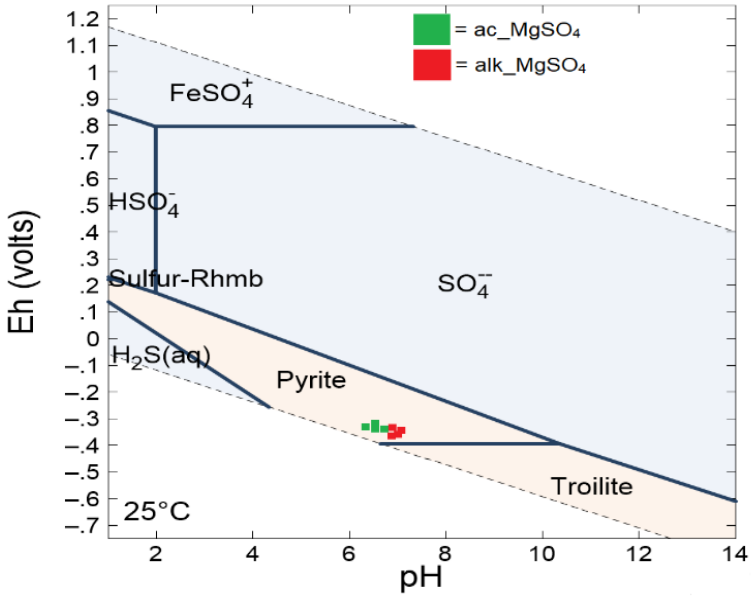

Figure 5.16: The redox and pH data, (green and red points represent data for day 1, 20, 120 & 145), of the ac_$MgSO_4$ and alk_$MgSO_4$ superimposed on a E_h-pH (Pourbaix) diagram for the Fe-Mg-S system. The predominance areas for the various sulfur phases in the E_h–pH diagram is based for the following conditions: soluble Fe^{2+} activity is 10^{-5}; SO_4^{2-} activity is 10^{-4}; Mg^{2+} activity is 10^{-3}; activity of H_2O is unity; T = 25°C; and P = 0.101 MPa. Activities were modelled using the Geochemist Workbench software

Previously stated, ideal conditions were created for SO_4^{2-} sorption, reduction, and pyrite precipitation (Eqs. 5.3 & 5.4). Followed by the subsequent sorption of Mg^{2+} on the pyrite surfaces (Equation 5.10);

$$>Fe^{II}\text{-}S_2^{1.67-}{}_{(surf)} + Mg^{2+}{}_{(aq)} \leftrightarrows >Fe^{II}\text{-}S_2\text{-}Mg^{0.33+}{}_{(surf)} \quad (5.10)$$

Followed by the sorption of SO_4^{2-} (Equation 5.11), however, $MgSO_4$ complex will not be stable;

$$>Fe^{II}\text{-}S_2\text{-}Mg^{0.33+}{}_{(surf)} + SO_4^{2-}{}_{(aq)} \leftrightarrows >Fe^{II}\text{-}S_2\text{-}Mg\text{-}SO_4^{1.67-}{}_{(surf)} \quad (5.11)$$

With rising pH, the following will also occur if iron oxides were present (Equations 5.12a and/or 5.12b);

$$>Fe^{II}\text{-}OH^{0.33-}_{(surf)} + Mg^{2+}_{(aq)} \leftrightarrows >Fe^{II}\text{-}OHMg^{1.67+}_{(surf)} \quad (5.12a)$$

$$>Fe^{III}\text{-}OH^{0.5-}_{(surf)} + Mg^{2+}_{(aq)} \leftrightarrows >Fe^{III}\text{-}OHMg^{1.5+}_{(surf)} \quad (5.12b)$$

Followed by the subsequent sorption of SO_4^{2-} (Equations 5.13a and/or 5.13b);

$$>Fe^{II}\text{-}OHMg^{1.67+}_{(surf)} + SO_4^{2-}_{(aq)} \leftrightarrows Fe^{II}\text{-}OHMgSO_4^{0.33-}_{(surf)} \quad (5.13a)$$

$$>Fe^{III}\text{-}OHMg^{1.5+}_{(surf)} + SO_4^{2-}_{(aq)} \leftrightarrows Fe^{III}\text{-}OHMgSO_4^{0.5-}_{(surf)} \quad (5.13b)$$

After day 120 and 145 the sorption of S and Mg was about unity as the pH increased to neutral conditions.

For the ac_$MgSO_4$ solution there was a poor correlation between the sorption of S and increasing pH, however, the correlation between Mg sorption and increasing pH was stronger (Fig. 5.17a). Furthermore, there were strong correlations between the sorption of S & Mg and decrease in E_h (Fig. 5.17b). The increased sorption of S and Mg with decreasing E_h was the exact opposite of what occurred in the ac_$CaSO_4$ solution and supported pyrite precipitation. There was a good correlation between Mg and S sorption (Fig. 5.18), where a continued incremental removal of both S and Mg were observed even after day 120.

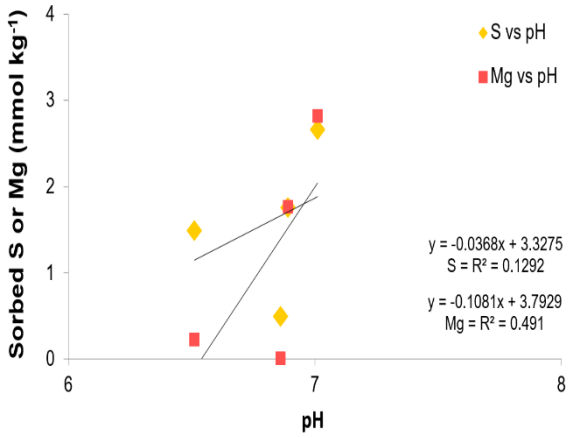

a

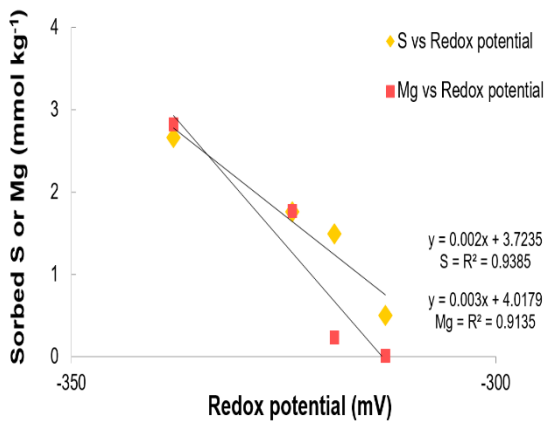

b

Figure 5.17: Correlation of S and Mg sorption as a function of (a) pH and (b) redox potential for the ac_$MgSO_4$ solution

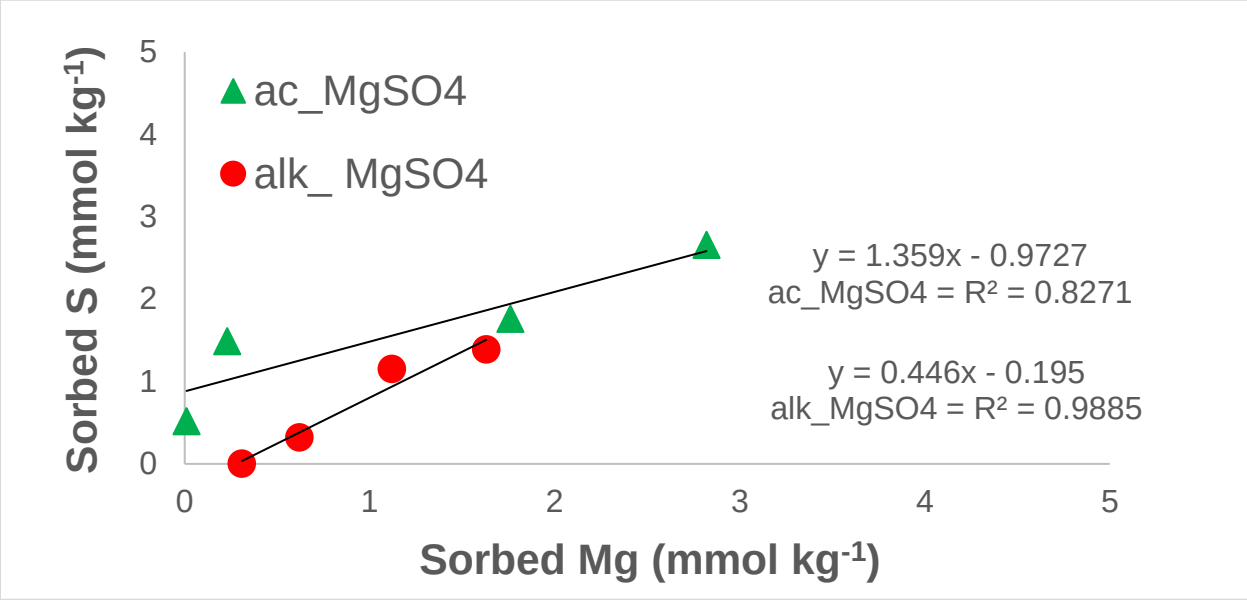

Figure 5.18: Correlation between S and Mg sorption for the ac_$MgSO_4$ and alk_$MgSO_4$ solutions

The alk_$MgSO_4$ solution was more alkaline throughout the experiment and S & Mg sorption was less (Fig. 5.15b & Table 5.5) compared to the ac_$MgSO_4$ solution. A slight decrease in pH from 8 to 7.88 occurred after day 1 and was buffered between 7 and 8 during the experiment. Furthermore, the redox potential decreased below -300 mV and, together with the pH, were ideal for sulfate sorption/reduction and pyrite precipitation on ZVI's surface, just like the ac_$MgSO_4$ solution (Fig. 5.16)

For the alk_$MgSO_4$ there were weak correlations between the sorption of S & Mg and increasing pH (Fig. 5.19a). The pH was not consequential for S sorption, however, for the ac_$MgSO_4$ solution better conditions, before 24 hours, for sulfate sorption was created, compared to the alk_$MgSO_4$ solution. The correlation between the sorption of S & Mg and decrease in E_h was stronger (Fig. 5.19b), however, it was weaker than the correlations observed for the ac_$MgSO_4$ solution. Increased sorption of S and Mg with decreasing E_h

was also observed and further supported pyrite precipitation. The decrease in E_h was the exact opposite of what occurred for the alk_$CaSO_4$ solution.

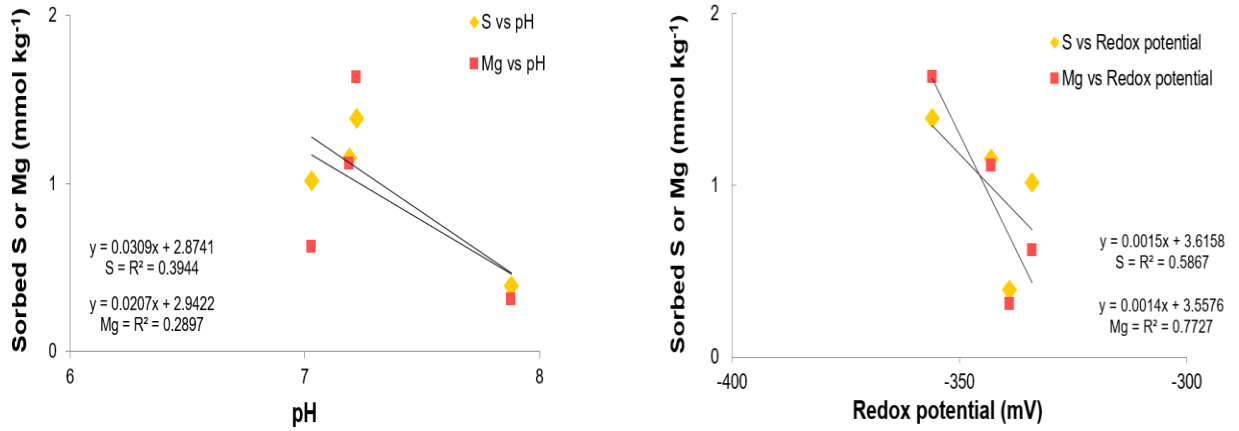

Figure 5.19: Correlation of S and Mg sorption as a function of (a) pH and (b) redox potential for the alk_$MgSO_4$ solution

In both $MgSO_4$ solutions, greater ZVI oxidation occurred compared to the $CaSO_4$ solutions. The differences between the ac_$CaSO_4$ and ac_$MgSO_4$ solutions, as well between the alk_$CaSO_4$ and alk_$MgSO_4$, isolated the greater effect Mg had on ZVI oxidation (Table 5.6 versus Table 5.2). However, $MgSO_4$ complexes are more soluble than $CaSO_4$ complexes because the ionization energy of Mg is higher (Brown et al., 2006) and will be easily exchanged from ZVI surfaces. Both $MgSO_4$ solutions showed higher rates of Fe^0 oxidation to Fe^{2+} as well as oxidation to Fe^{3+} in the first 24 hours but slowed down after day 20. After day 120 there was a decrease in Fe^{3+} concentration for the alk_$MgSO_4$ solution. This was attributed to reduction of Fe^{3+} back to Fe^{2+} because of the continued decrease in redox potential, suggesting strong continued electron transfer to the solution, preventing further oxidation. Table D.3 (Appendix D) suggested neither epsomite nor brucite in the ac_$MgSO_4$ and alk_$MgSO_4$ solution. Strong correlations between S and Mg sorption (Fig. 5.18) suggested co-sorption mechanisms similar than for the $CaSO_4$ treatments (Figs. 5.5 & 5.11)

Table 5.6: Dissolved Fe in the 3.12 *mM* $MgSO_4$ solutions

ac_$MgSO_4$	Fe_{Tot}[a]	Fe^{2+}	Fe^{3+}	Fe^{3+}/Fe_{Tot}
Day 1	2.40	0.84 (± 0.00)[b]	1.56 (± 1.5E-03)	0.65
Day 20	2.40	0.84 (± 3.70E-04)	1.56 (± 3.4E-03)	0.6
Day 120	2.71	1.76 (± 1.30E-03)	0.95 (± 5.5E-04)	0.35
Day 145	2.84	1.85 (± 1.10E-03)	0.99 (± 1.2E-03)	0.35
alk_$MgSO_4$	**Fe_{Tot}**	**Fe^{2+}**	**Fe^{3+}**	**Fe^{3+}/Fe_{Tot}**
Day 1	1.40	0.63 (± 6.50E-04)	0.77 (± 2.50E-03)	0.55
Day 20	1.40	0.65 (± 6.50E-04)	0.75 (± 5.70E-04)	0.53
Day 120	1.50	1.01 (± 1.90E-03)	0.49 (± 2.30E-03)	0.33
Day 145	1.51	1.40 (± 3.70E-04)	0.11 (± 1.40E-03)	0.07

a = Fe_{Tot}, Fe^{2+} and Fe^{3+} reported in mmol kg^{-1}.
b = Value in brackets is standard deviation of samples.

For the ac_$MgSO_4$ solution there was a correlation between S sorption and Fe^{2+}, however, the correlation was stronger between Mg sorption and dissolved Fe^{2+} (Fig. 5.20a). For the ac_$MgSO_4$ solution, S sorption correlated with dissolved Fe^{3+}, however, Mg sorption correlated stronger with Fe^{3+}. Mg showed a higher capacity for exchanging Fe^{2+} on the surface of ZVI, leading to increased concentrations of dissolved Fe in the solutions. For the alk_$MgSO_4$ solution there were strong correlations between S & Mg sorption and dissolved Fe^{2+}, as well as strong correlations between S & Mg sorption and dissolved Fe^{3+} (Fig. 5.20b). Corrosion of Fe was not as strong for the alk_$MgSO_4$ compared to the ac_$MgSO_4$ solution because it started at a pH of 8. The low redox potentials produced was ideal for SO_4^{2-} reduction.

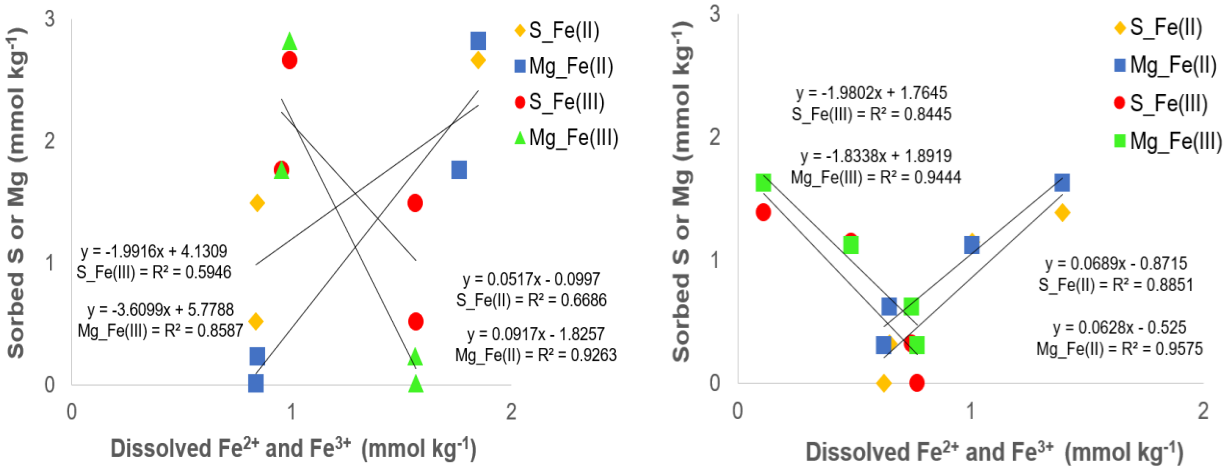

a **b**

Figure 5.20: Sorption of S & Mg vs dissolved Fe^{2+} and Fe^{3+} for the (a) ac_$MgSO_4$ and (b) alk_$MgSO_4$ solution

5.3.1.4 The $MgSO_4$ solution at 12.5 mM

It was expected that the $MgSO_4$ solutions (12.5 *mM*) will also be buffered at a pH value of ±7 because of the buffering capacities ZVI exhibited in the $CaSO_4$ solutions (3.12 *mM* and 12.5 *mM*) and $MgSO_4$ solutions (3.12 *mM*). Another expectation was that the sorption of S and Mg will be greater than the $MgSO_4$ solutions at 3.12 *mM*, given the increased sorption of S and Ca in the $CaSO_4$ solutions at 12.5 *mM* compared to the Ca solutions at 3.12 *mM*. Both S and Mg removal was more substantial for the AC_$MgSO_4$ than the ALK_$MgSO_4$ solution (Fig. 5.21 & Table 5.7).

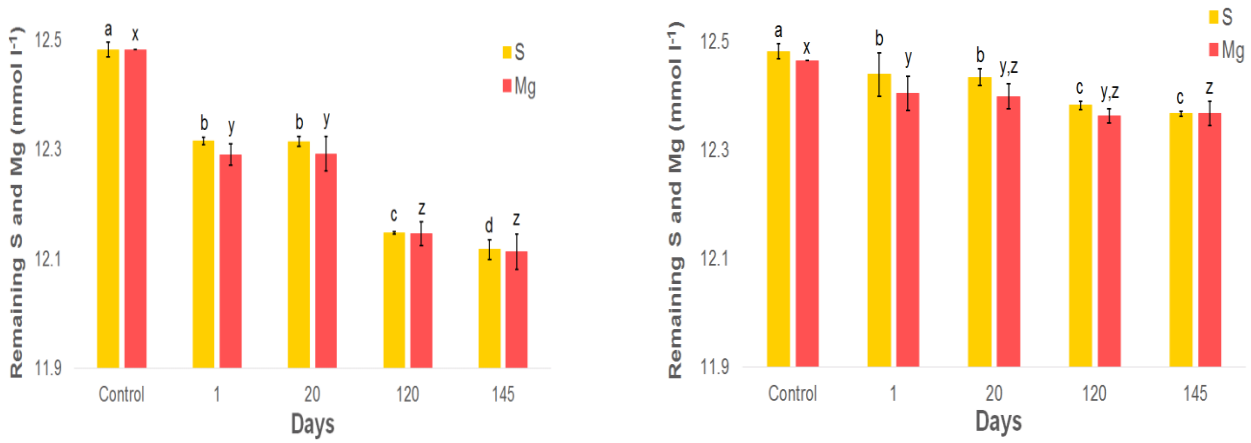

a **b**

Figure 5.21: Change in aqueous S & Mg in the (a) AC_$MgSO_4$ and (b) ALK_$MgSO_4$ solutions. The least significant difference of S & Mg for (a) are 0.02 & 0.04 and in (b) are 0.04 & 0.04 at a confidence level of 95% (α = 0.05). Error bars represent standard deviations and the letters represent the significant differences between experimental days

Table 5.7: Sorption of S and Mg for the 12.5 *mM* $MgSO_4$ solutions

AC_$MgSO_4$ Sorbed (mmol kg^{-1})						ALK_$MgSO_4$ Sorbed (mmol kg^{-1})					
Day	**S**	**Mg**	**S/Mg**	**pH**	**E_h[a]**	**Day**	**S**	**Mg**	**S/Mg**	**pH**	**E_h**
1	6.65	7.67	0.87	6.78	-296	**1**	1.71	2.44	0.70	7.71	-329
20	6.70	7.60	0.88	6.45	-309	**20**	1.90	2.64	0.72	6.93	-334
120	13.4	13.4	1.00	6.75	-324	**120**	3.96	4.07	0.97	7.12	-343
145	14.6	14.8	0.99	6.90	-342	**145**	4.60	3.91	1.18	7.15	-385

a = Redox potentials reported in mV.

The AC_$MgSO_4$ solution showed the most sorption of all $MgSO_4$ treatments. Furthermore, the AC_$MgSO_4$ solution showed the second highest cation removal. For the AC_$MgSO_4$ solution, the sorption of S was less than Mg after day 1 and 20. The pH increased from 4 to 6.78 in 24 hours, caused by ZVI oxidation and H_2O decomposition as H^+ is reduced to H_2. This kinetic reaction was in a rapidly repeating cycle. The pH slightly decreased to 6.45 after 20 days. The E_h decreased close to -300 mV after 24 hours and 20 days and remained below -300 mV after day 120 & 145. This was ideal conditions for sulfate sorption and reduction as well as pyrite precipitation (Eqs. 5.4 & 5.5) and was supported by data in the Pourbaix diagram (Fig. 5.22). This was followed by the sorption of Mg (Eq. 5.10). If Fe oxides were present on ZVI's surface sorption of S and Mg was also possible (Eqs. 5.11 & 5.12). After day 120 and 145 there was an equimolar decrease in S and Mg as the pH increased to 6.75 and then 6.9. The pH was near neutral and showed a co-sorption of S and Mg.

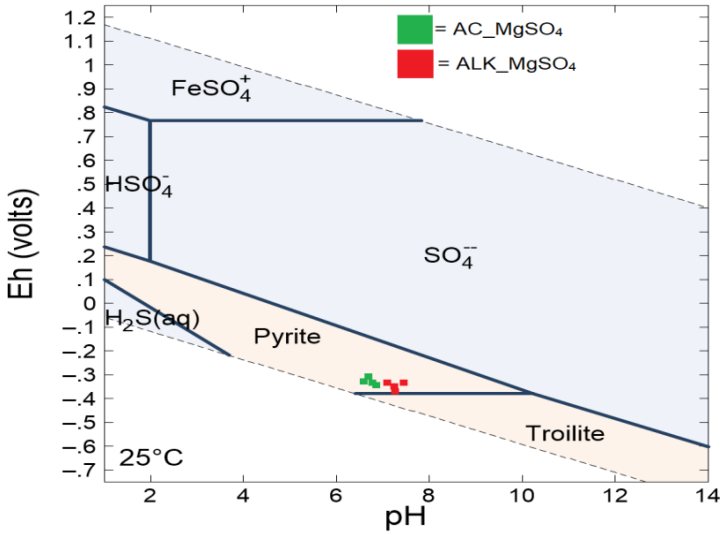

Figure 5.22: The redox and pH data, (green and red points represent data for day 1, 20, 120 & 145), of the AC_$MgSO_4$ and ALK_$MgSO_4$ superimposed on a E_h-pH (Pourbaix) diagram for the Fe-Mg-S system. The predominance areas for the various sulfur phases in the E_h–pH diagram is based for the following conditions: soluble Fe^{2+} activity is 10^{-5}; SO_4^{2-} activity is 10^{-3}; Mg^{2+} activity is 10^{-3}; activity of H_2O is unity; T = 25°C; and P = 0.101 MPa. Activities were modelled using the Geochemist Workbench software

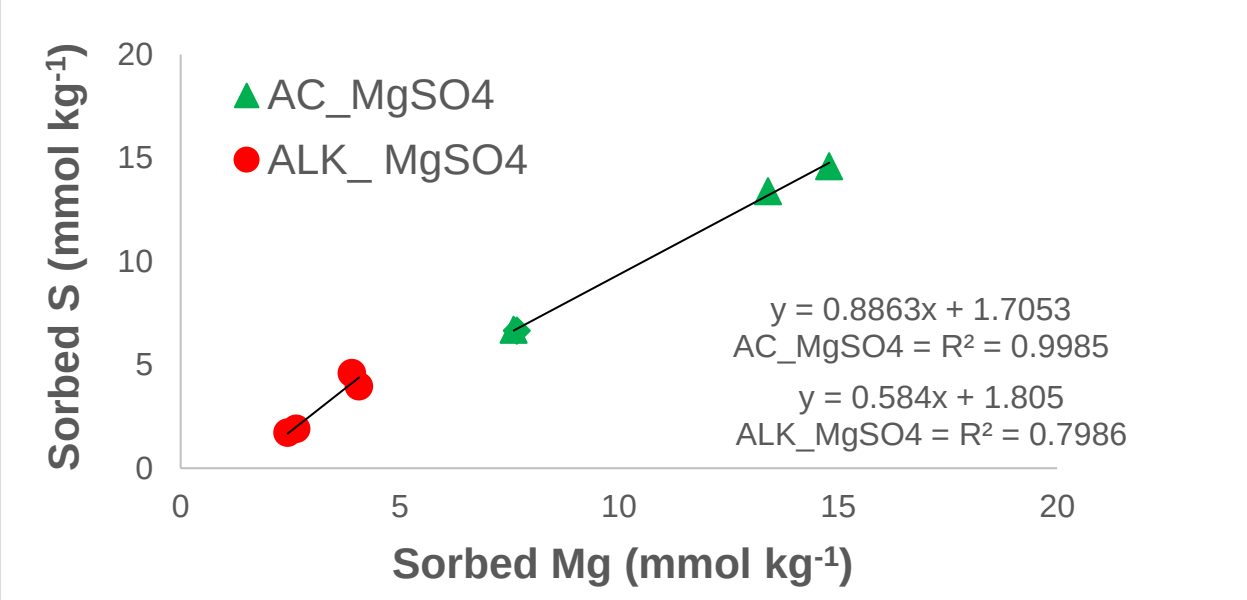

Figure 5.23: Correlation between S and Mg sorption for the AC_$MgSO_4$ and ALK_$MgSO_4$ solutions

The Pourbaix diagram does not explain Mg sorption, however, the positive correlations between S removal from solution and that of Mg (Fig. 5.23) suggested that Mg and S sorption was possibly linked. Further supporting evidence for this is the fact that Mg sorption increased with decreasing redox potential (Fig. 5.25b). The fact that Mg sorption showed some increase with increasing pH points to sorption on surfaces that carries variable charge (Fig. 5.25a). XRD analysis of the AC_$MgSO_4$ solution, did not show that iron oxides formed on the surface of ZVI. If it did form, the concentration thereof must have been less than 2% (the detection limit of XRD) (Fig. 5.24). The phases that precipitated on the ZVI's surface could only be identified as pyrite at XRD peaks of 24°, 52° and 67° which related to XRD data of natural pyrite presented by Fathinia et al. (2015). As discussed, pyrite has variable charged surfaces (with pzc = 1.7). The role of iron oxide surfaces was expected to be less important than for the $CaSO_4$ solutions.

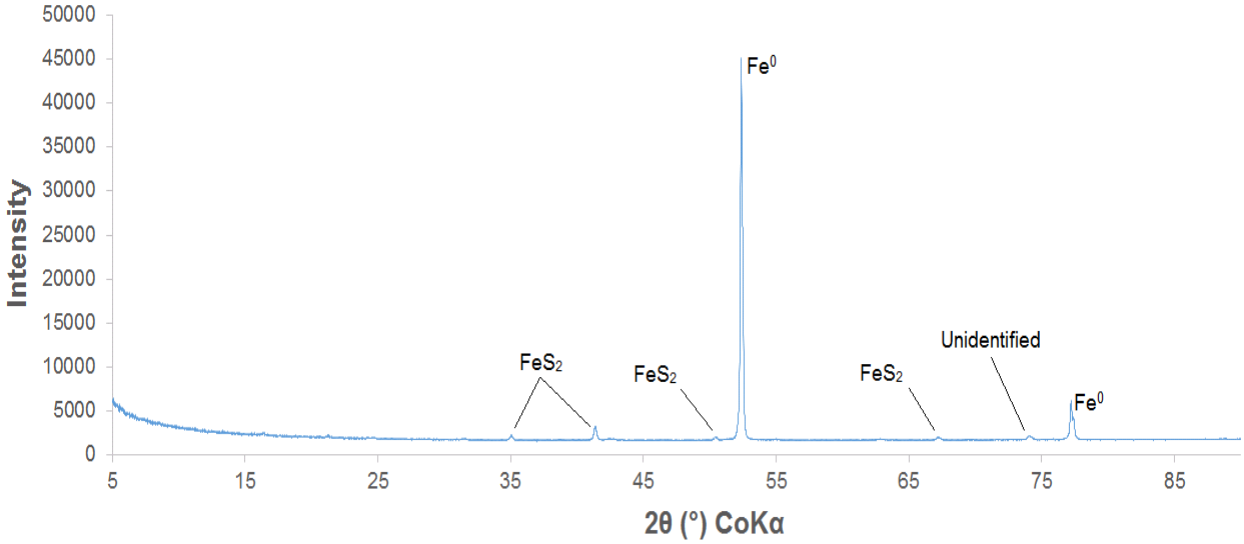

Figure 5.24: XRD of mZVI powder, taken from the AC_$MgSO_4$ solution after 145 days

Mg precipitation as brucite occurs when the pH approaches 9 (Limper et al., 2018). The pH, for each $MgSO_4$ solutions, was buffered between 6 and 8 and could not reach conditions for possible Mg precipitation. The sorption of Mg was, as mentioned, attributed to pyrite precipitation and subsequent Mg sorption on their variably charged surfaces.

There were weak correlations between the sorption of S & Mg and increase in pH for the AC_$MgSO_4$ solution (Fig. 5.25a). However, strong correlations between the sorption of S & Mg and decrease in E_h was observed (Fig. 5.25b). Figure 5.23 showed a strong correlation between the co-sorption of S and Mg, while the S/Mg ratio remained close to ±1 during the experiment (Table 5.7). The correlation between Mg sorption and decrease in E_h suggested pyrite induced co-sorption.

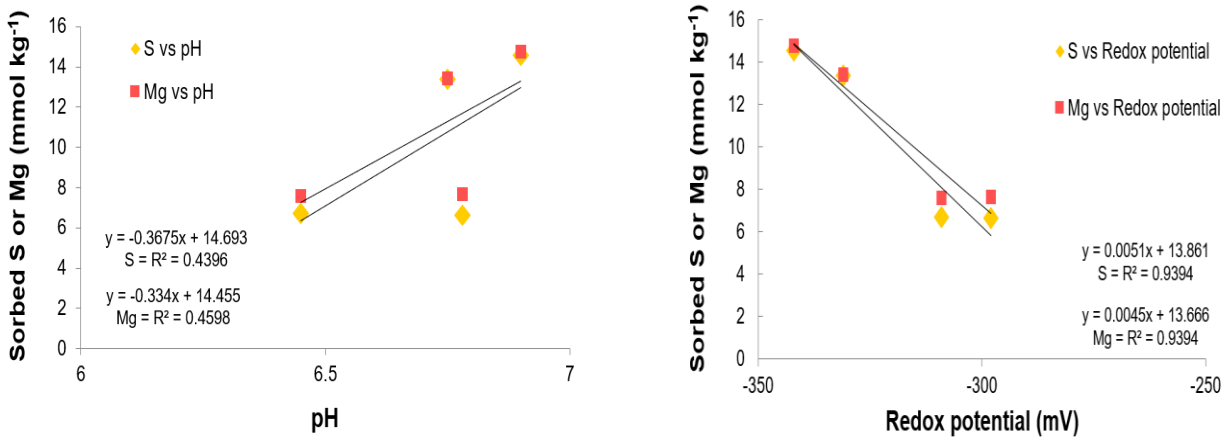

a **b**

Figure 5.25: Correlation of S and Mg sorption as a function of (a) pH and (b) redox potential for the AC_$MgSO_4$ solution

The sorption of S and Mg for the ALK_$MgSO_4$ solution was much lower compared to the AC_$MgSO_4$ solution (Fig. 5.21b & Table 5.7) Furthermore, the sorption of S was less than Mg during the experiment except after day 145. The pH decreased from 8 to 7.71 and then to 6.93 after day 1 & 20. The slight decrease in pH and the greater concentration of dissolved Fe^{3+} in the ALK_$MgSO_4$ solution (Table 5.8) suggested precipitation of Fe oxides that will also produce acidity in solution. Magnesium sorption by $>Fe^{II}\text{-}OH^{0.33-}$ and $>Fe^{III}\text{-}OH^{0.5-}$ functional groups (Eq. 5.11a and/or 5.11b) and S sorption (Eq. 5.12a and/or 5.12b) on ZVI's surface were likely. There was a slight increase in pH after day 120 and 145 where the pH was buffered between 6 and 8. The sorption mechanisms for sulfate and its reduction, and transformation/precipitation to pyrite (Eqs. 5.3 & 5.4) were proposed because the pH and E_h in solution were ideal (Fig. 5.22).

There were weak correlations between the sorption of S & Mg and increase in pH for the ALK_$MgSO_4$ solution (Fig. 5.26a). However, there were strong correlations between the sorption of S & Mg and the decrease in E_h (Fig. 5.26b), suggesting the co-sorption of Mg occurred during pyrite precipitation.

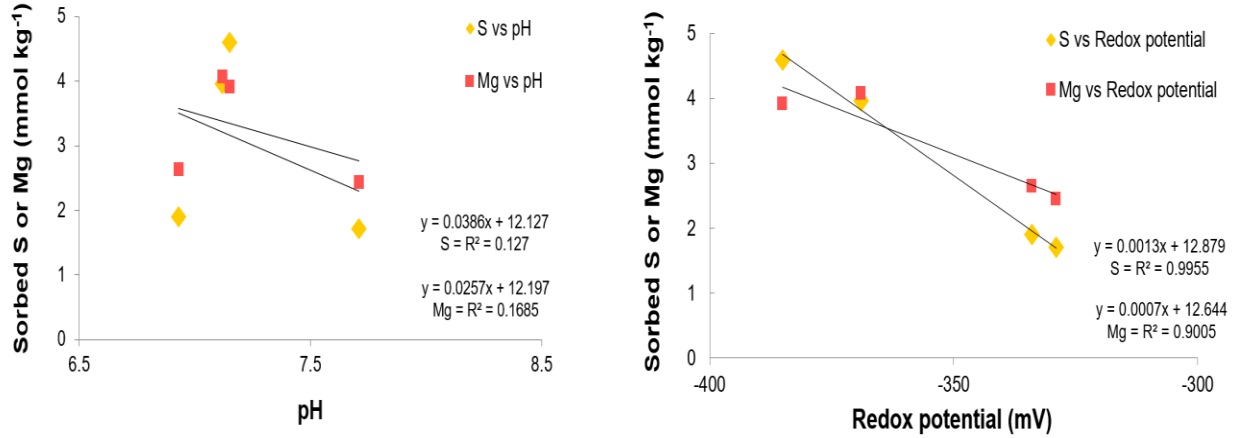

a **b**

Figure 5.26: Correlation of S and Mg sorption as a function of (a) pH and (b) redox potential for the ALK_$MgSO_4$ solution

The sorption of S and Mg in solutions at 12.5 *mM* was greater than for the 3.12 *mM* treatments, which was the same trend than for Ca^{2+} in the $CaSO_4$ solutions (Table 5.8 versus Table 5.6). Furthermore, there was a big difference in sorption between the AC_$MgSO_4$ solution and the ALK_$MgSO_4$ solution and for Fe-Mg-S systems the anoxic corrosion of ZVI, by Mg, also occurred at a higher rate compared to Ca in Fe-Ca-S systems at 12.5 *mM*.

Table 5.8 showed that in both $MgSO_4$ solutions Fe^0 rapidly oxidized to Fe^{2+} within 1 day, and concentrations continued to increase during the experiment. Rapid oxidation of Fe^{2+} to Fe^{3+} also occurred in the first 24 hours. The Fe^{3+}/Fe_{Tot} ratios in both solutions were below 0.35, also suggesting that Fe^{2+}:Fe^{3+} rich minerals such as magnetite and green rust were likely to precipitate. The fundamental difference between AC_$MgSO_4$ and ALK_$MgSO_4$ solution was that for the AC_$MgSO_4$ solutions Fe^{3+} increased from day 1 to 120 and then drastically decreased on day 145, suggesting that, in the long run, Fe^{3+} was

not stable in the AC_$MgSO_4$ solution. ZVI left reduced S, and presumably reduced Fe^{3+} back to Fe^{2+}, at a greater rate than Fe^{3+} formation.

Table 5.8: Dissolved Fe in the 12.5 *mM* $MgSO_4$ solutions

AC_$MgSO_4$	**Fe_{Tot}[a]**	**Fe^{2+}**	**Fe^{3+}**	**Fe^{3+}/Fe_{Tot}**
Day 1	5.48	4.60 (± 9.9E-04)[b]	0.84 (± 7.10E-03)	0.15
Day 20	5.63	4.60 (± 1.1E-03)	0.99 (± 4.90E-03)	0.17
Day 120	7.92	6.40 (± 2.4E-02)	1.48 (± 2.10E-02)	0.18
Day 145	7.83	7.80 (± 1.1E-02)	0.07 (± 1.80E-03)	0.01
ALK_$MgSO_4$	**Fe_{Tot}**	**Fe^{2+}**	**Fe^{3+}**	**Fe^{3+}/Fe_{Tot}**
Day 1	7.92	5.56 (± 3.10E-03)	2.36 (± 6.80E-03)	0.29
Day 20	8.52	5.60 (± 4.10E-03)	2.92 (± 1.20E-02)	0.34
Day 120	9.40	6.88 (± 3.60E-02)	2.52 (± 3.50E-02)	0.27
Day 145	9.61	9.00 (± 3.60E-03)	0.61 (± 1.20E-03)	0.06

a = Fe_{Tot}, Fe^{2+} and Fe^{3+} reported in mmol kg^{-1}.

b = Value in brackets is standard deviation of samples.

Figure 5.27a & 5.27b showed that with an increase in Mg sorption there was a direct increase in dissolved Fe, for the AC_$MgSO_4$ solution and the ALK_$MgSO_4$ solution. This suggested that the presence of Mg caused higher corrosion rates that led to increased dissolved Fe^{2+} concentrations. The total dissolved iron in the comparative $CaSO_4$ solutions were much less at 1.38 - 1.47 mmol kg^{-1} for the AC_CaSO4 solution and 0.73 - 0.79 mmol kg^{-1} for the ALK_CaSO4. Mg therefore corroded ZVI's surface at a higher rate compared to Ca. The correlation between S & Mg sorption and dissolved Fe^{2+} for the AC_$MgSO_4$ solution also supported pyrite precipitation. For the AC_$MgSO_4$ solution Fe^{3+} did not play a role in S and Mg sorption, however, the ALK_$MgSO_4$ solution shows that pyrite formation was less dominant.

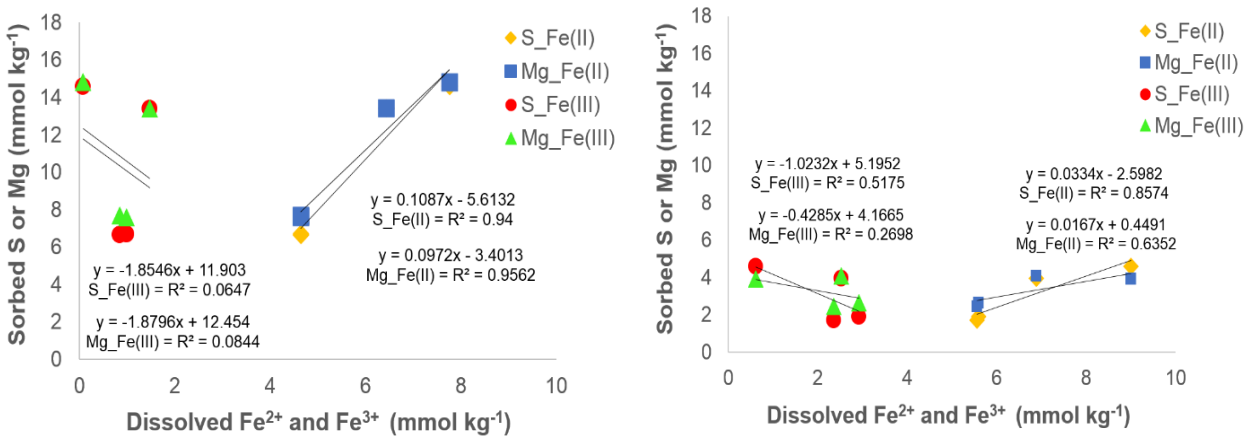

a **b**

Figure 5.27: Sorption of S & Mg vs dissolved Fe^{2+} and Fe^{3+} for the (a) AC_$MgSO_4$ and (b) ALK_$MgSO_4$ solution

5.3.1.5 The Ca-$MgSO_4$ solution at 12.5 mM

The combination of Ca and Mg in the sulfate solutions produced the lowest redox potentials (Chapter 4) and so it was expected that the combination of Ca and Mg would show greater corrosion of ZVI's surface compared to the individual solutions containing only Ca or Mg. Figure 5.28a & 5.28b showed the decrease of S, Ca and Mg, in the AC_Ca-$MgSO_4$ and ALK_Ca-$MgSO_4$ solutions respectively, during the experiment. Furthermore, Table 5.9 showed the sorption of S, Ca and Mg by ZVI in the AC_Ca-$MgSO_4$ and ALK_Ca-$MgSO_4$ solutions. Both sulfate, Ca and Mg removal was more substantial for the AC_Ca-$MgSO_4$ solution than the ALK_Ca-$MgSO_4$ solution and showed tendencies similar to the AC_$MgSO_4$ solution.

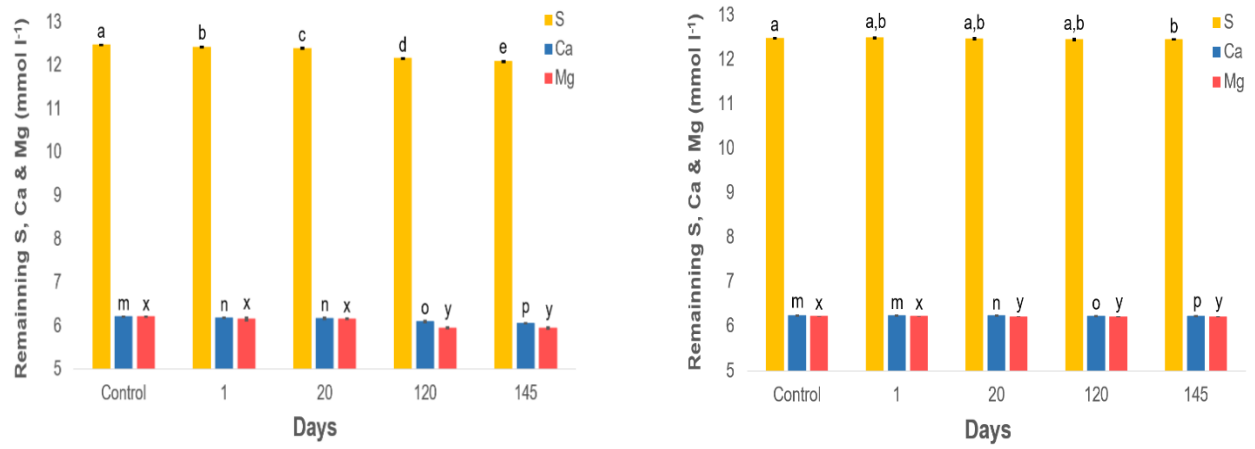

a **b**

Figure 5.28: Change in aqueous S, Ca & Mg in the AC_Ca-$MgSO_4$ solutions. The least significant difference of S, Ca & Mg for (a) are 0.02, 0.02 & 0.02 and for (b) are 0.04, 0.003 & 0.004 at a confidence level of 95% (α = 0.05). Error bars represent standard deviations and the letters represent the significant differences between experimental days

Table 5.9: Sorption of S, Ca and Mg for the 12.5 *mM* Ca-$MgSO_4$ solutions

AC_Ca-$MgSO_4$ Sorbed (mmol kg^{-1})							**ALK_Ca-$MgSO_4$ Sorbed (mmol kg^{-1})**						
Day	**S**	**Ca**	**Mg**	**S/[Ca+Mg]**	**pH**	**E_h[a]**	**Day**	**S**	**Ca**	**Mg**	**S/[Ca+Mg]**	**pH**	**E_h**
1	2.28	1.13	2.01	0.73	6.86	-222	**1**	0.00	0.11	0.04	0.00	8.21	-312
20	3.15	1.52	1.90	0.92	6.57	-348	**20**	0.55	0.36	0.26	0.89	7.12	-363
120	12.4	4.21	10.2	0.86	6.28	-388	**120**	1.00	0.61	0.36	1.03	7.55	-374
145	15.4	5.93	10.7	0.93	6.16	-355	**145**	1.15	0.74	0.36	1.05	7.87	-421

a = Redox potentials reported in mV.

For the AC_Ca-$MgSO_4$ solution, Mg sorption was greater than Ca sorption (Fig. 5.28a & Table 5.9) suggesting that Mg sorption had preference above Ca in the slightly acidic solution. The sorption of [Ca + Mg] was greater than S sorption after day 1, 20 and 120 but came close to unity after day 145 ($\sum Cation_{sorp} = \sum Anion_{sorp}$). The initial pH of 4 increased to 6.86 after 24 hours and was buffered between 6 and 7. There was a strong correlation between the decrease in pH and experimental days (Fig. C4, Appendix C) and only the AC_Ca-$MgSO_4$ solution had this decreasing trend in pH. Furthermore, the redox potential decreased to -222 mV within 24 hours, and further decreased below -300 mV during the rest of the experiment. Just like for the $MgSO_4$ solutions, the same sorption mechanisms were proposed for sulfate sorption, reduction and pyrite precipitation (Eqs. 5.3 & 5.4) supported by the Pourbaix diagram (Fig. 5.29).

Followed by the subsequent sorption of Ca^{2+} and Mg^{2+} on the pyrite surfaces (Equations 5.14a and 5.14b);

$$>Fe^{II}\text{-}S_2^{1.67-}{}_{(surf)} + Ca^{2+}{}_{(aq)} \leftrightarrows >Fe^{II}\text{-}S_2\text{-}Ca^{0.33+}{}_{(surf)} \quad (5.14a)$$

$$>Fe^{II}\text{-}S_2^{1.67-}{}_{(surf)} + Mg^{2+}{}_{(aq)} \leftrightarrows >Fe^{II}\text{-}S_2\text{-}Mg^{0.33+}{}_{(surf)} \quad (5.14b)$$

Followed by the sorption of SO_4^{2-} (Equations 5.15a and/or 5.15b), however $CaSO_4$ will not be stable (Eq. 5.15a) and $MgSO_4$ will be even less stable (Eq. 15b);

$$>Fe^{II}\text{-}S_2\text{-}Ca^{0.33+}{}_{(surf)} + SO_4^{2-}{}_{(aq)} \leftrightarrows >Fe^{II}\text{-}S_2\text{-}Ca\text{-}SO_4^{1.67-}{}_{(surf)} \quad (5.15a)$$

$$>Fe^{II}\text{-}S_2\text{-}Mg^{0.33+}{}_{(surf)} + SO_4^{2-}{}_{(aq)} \leftrightarrows >Fe^{II}\text{-}S_2\text{-}Mg\text{-}SO_4^{1.67-}{}_{(surf)} \quad (5.15b)$$

However, with rising pH, the following will also occur if iron oxides were present (Equations 5.16a, 5.16b, 5.16c and/or 5.16d);

$$>Fe^{II}\text{-}OH^{0.33-}{}_{(surf)} + Ca^{2+}{}_{(aq)} \leftrightarrows >Fe^{II}\text{-}OH\text{-}Ca^{1.67+}{}_{(surf)} \quad (5.16a)$$

$$>Fe^{III}\text{-}OH^{0.5-}{}_{(surf)} + Ca^{2+}{}_{(aq)} \leftrightarrows >Fe^{III}\text{-}OH\text{-}Ca^{1.5+}{}_{(surf)} \quad (5.16b)$$

$$>Fe^{II}\text{-}OH^{0.33-}{}_{(surf)} + Mg^{2+}{}_{(aq)} \leftrightarrows >Fe^{II}\text{-}OH\text{-}Mg^{1.67+}{}_{(surf)} \quad (5.16c)$$

$$>Fe^{III}\text{-}OH^{0.5-}{}_{(surf)} + Mg^{2+}{}_{(aq)} \leftrightarrows >Fe^{III}\text{-}OH\text{-}Mg^{1.5+}{}_{(surf)} \quad (5.16d)$$

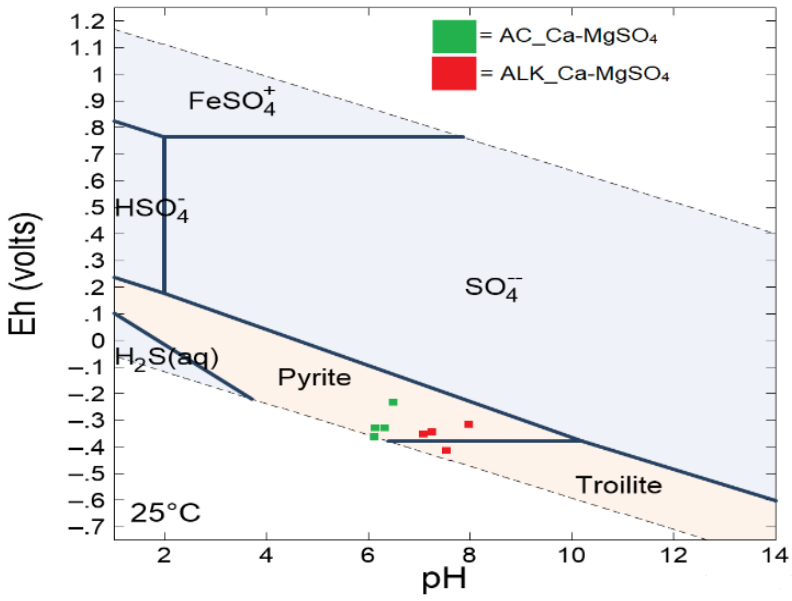

Figure 5.29: The redox and pH data, (green and red points represent data for day 1, 20, 120 & 145), of the AC_Ca-$MgSO_4$ and ALK_Ca-$MgSO_4$ superimposed on a E_h-pH (Pourbaix) diagram for the Fe-Ca-Mg-S system. The predominance areas for the various sulfur phases in the E_h–pH diagram is based for the following conditions: soluble Fe^{2+} activity is 10^{-5}; SO_4^{2-} activity is 10^{-3}; Ca^{2+} activity is 10^{-3}; Mg^{2+} activity is 10^{-3}; activity of H_2O is unity; T = 25°C; and P = 0.101 MPa. Activities were modelled using the Geochemist Workbench software

There was a strong correlation between the sorption of S, Ca & Mg and the increase in pH in the AC_Ca-$MgSO_4$ solution (Fig. 5.30a). Surprisingly, however, there was not strong correlations between the sorption of S, Ca & Mg and decrease in E_h (Fig. 5.30b). This suggested that the sorption of S, Ca and Mg was indirectly related to pH and not E_h. Figure 5.31 showed a strong correlation between the sorption of S, Ca & Mg and the S/[Ca+Mg] ratios were close to unity during the experiment (Table 5.9). This suggested that there was a stoichiometric decrease in S, Ca and Mg during the experiment.

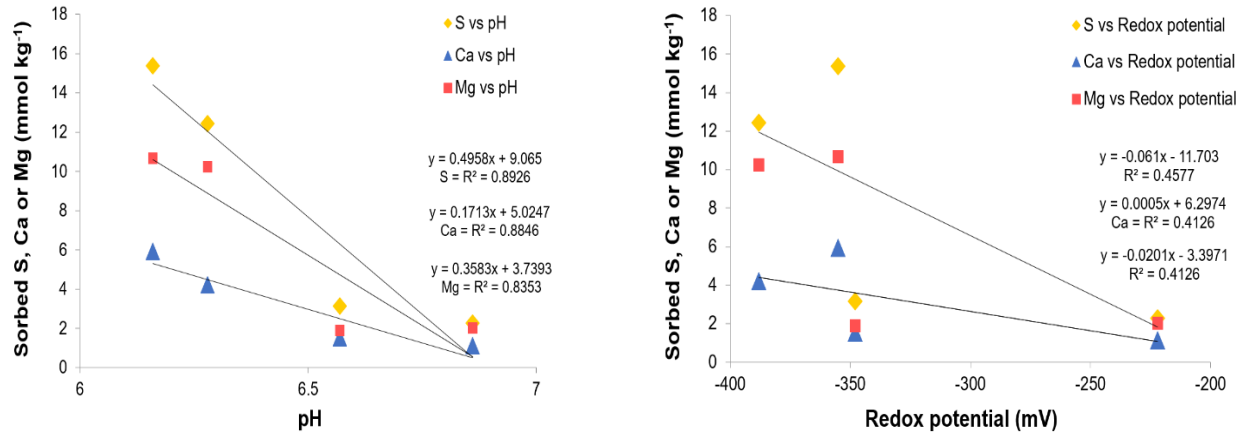

a **b**

Figure 5.30: Correlation of S, Ca and Mg sorption as a function of (a) pH and (b) redox potential for the AC_Ca-$MgSO_4$ solution

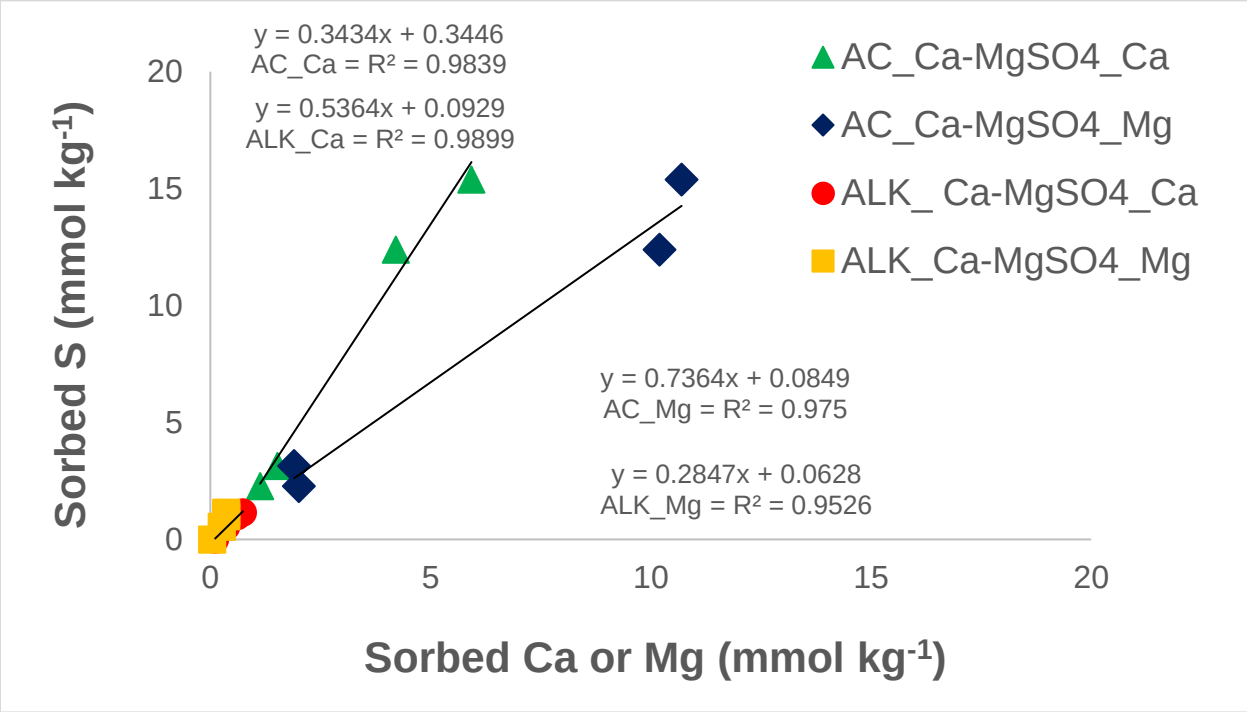

Figure 5.31: The correlation between S, Ca and Mg sorption for the AC_Ca-$MgSO_4$ and ALK_Ca-$MgSO_4$ solutions

For the ALK_Ca-$MgSO_4$ solution, the sorption of S was less than the combined sorption of Ca and Mg, after day 1 and 20 (Fig. 5.28b and Table 5.9). However, after day 120 S sorption surpassed the combined sorption of Ca and Mg. The pH increased slightly from 8 to 8.21 after day 1 and was buffered between 7 and 8.5 during the rest of the experimentation. The E_h decreased well below -300 mV and remained below this redox potential during the experiment. The conditions created were ideal for pyrite precipitation, as well (Fig. 5.29). The mechanisms likely responsible for the sorption/removal of S, Ca and Mg can also be attributed to sulfate sorption/reduction and surface precipitation of pyrite (Eqs. 5.4 & 5.5), followed by Ca and Mg sorption (Eqs. 5.13 & 5.14).

There were poor correlations between the sorption of S, Ca & Mg and the increase in pH for the ALK_Ca-$MgSO_4$ solution (Fig. 5.32a). However, there were strong correlations between the sorption in S, Ca & Mg and decrease in E_h (Fig. 5.32b). This suggested that the sorption of S, Ca and Mg was related to E_h. Figure 5.31 showed a positive correlation between the sorption of S, Ca & Mg, and the S/[Ca+Mg] ratios were also close to unity

during the experiment (Table 5.9). This suggested that for the ALK_Ca-$MgSO_4$ solution there was also stoichiometric decrease in S, Ca and Mg during the experiment.

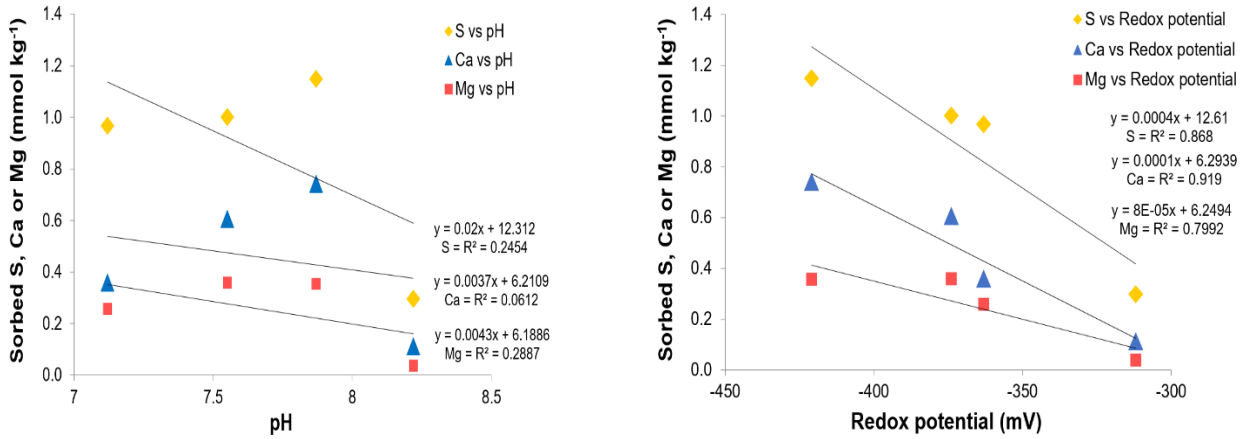

a **b**

Figure 5.32: Correlation of S, Ca and Mg sorption as a function of (a) pH and (b) redox potential for the ALK_Ca-$MgSO_4$ solution

In the AC_Ca-$MgSO_4$ solution Mg sorption was greater than Ca sorption and was opposite to the sorption of Ca and Mg for the ALK_Ca-$MgSO_4$ solution. Furthermore, only for the AC_Ca-$MgSO_4$ solution did the pH continuously decrease after day 1. The sorption of S, Ca and Mg in the solutions that were initially acidic was 13 times greater than for the solution that was initially alkaline.

Table 5.10 showed that in both Ca-$MgSO_4$ solutions Fe^0 rapidly dissolved and oxidized to Fe^{2+} after day 1. Oxidation of Fe^{2+} to Fe^{3+} also occurred after the first day, however, the reduced conditions in both solutions prevented further oxidation of Fe^{2+}. The dissolved Fe concentration in the AC_$CaMgSO_4$ solution was greater than the ALK_Ca-$MgSO_4$ solution and was attributed to its initial acidity before 24 hours. The Fe^{3+}/Fe_{Tot} ratios for the AC_Ca-$MgSO_4$ solution was at and below 0.13 during the experimentation, suggesting that Fe^{2+} rich minerals such as pyrite were likely to precipitate. The Fe^{3+}/Fe_{Tot} ratio for the ALK_Ca-$MgSO_4$ solution, however, ranged between 0.17 and 0.29, suggesting that Fe^{2+}:Fe^{3+} rich minerals such as magnetite and green rust also could have precipitated.

Table 5.10: Dissolved Fe in the 12.5 *mM* Ca-$MgSO_4$ solutions

AC_Ca-$MgSO_4$	Fe_{Tot}[a]	Fe^{2+}	Fe^{3+}	Fe^{3+}/Fe_{Tot}
Day 1	14.2	12.8 (± 6.50E-04)[b]	1.42 (± 2.40E-03)	0.09
Day 20	14.9	12.8 (± 9.90E-04)	2.05 (± 1.50E-02)	0.13
Day 120	15.9	14.8 (± 9.70E-04)	1.13 (± 9.10E-04)	0.07
Day 145	16.1	15.4 (± 4.10E-03)	0.77 (± 1.10E-02)	0.05
ALK_Ca-$MgSO_4$	Fe_{Tot}	Fe^{2+}	Fe^{3+}	Fe^{3+}/Fe_{Tot}
Day 1	4.24	3.42 (± 1.10E-03)	0.82 (± 1.70E-03)	0.19
Day 20	4.88	3.46 (± 6.50E-04)	1.42 (± 2.80E-03)	0.29
Day 120	5.04	3.73 (± 3.20E-03)	1.30 (± 2.30E-03)	0.26
Day 145	5.18	4.28 (± 7.50E-04)	0.90 (± 1.50E-03)	0.17

a = Fe_{Tot}, Fe^{2+} and Fe^{3+} reported in mmol kg^{-1}.

b = Value in brackets is standard deviation of samples.

Mg and Ca corroded ZVI's surface at a higher rate compared to individual $CaSO_4$ or $MgSO_4$ solutions (Table 5.10 versus Table 5.4 & 5.8). There were strong correlations between S, & Mg sorption and dissolved Fe^{2+} (Fig. 5.33a) suggesting a co-sorption occurred, similar to that of the $MgSO_4$ treatments at 3.12 *mM* and 12.5 *mM* (Fig. 5.15 & 5.20).

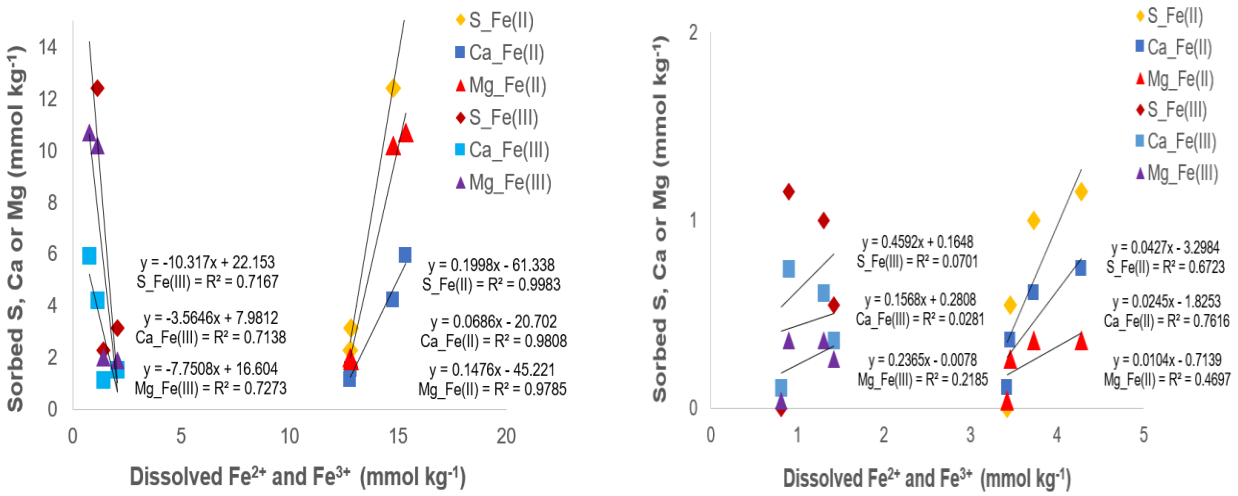

a **b**

Figure 5.33: Sorption of S, Ca & Mg vs dissolved Fe^{2+} in solution of the (a) AC_Ca-$MgSO_4$ and (b) ALK_Ca-$MgSO_4$ solution

XRD showed that a variety of Fe phases formed in the AC_Ca-$MgSO_4$ solution (Fig. 5.34), showing that the system was not at a thermodynamic equilibrium. Pyrite was identified at XRD peaks of 24°, 52° and 67° which related to XRD data of natural pyrite presented by Fathinia et al., (2015). Other phases that precipitated on the ZVI's surface were identified as goethite, magnetite and $Ca(OH)_2$ based on the d-spacing reported by (Furukawa et al., 2002; Filip et al., 2014; Fujioka et al., 2016; Ghica et al., 2016; Mu et al., 2017).

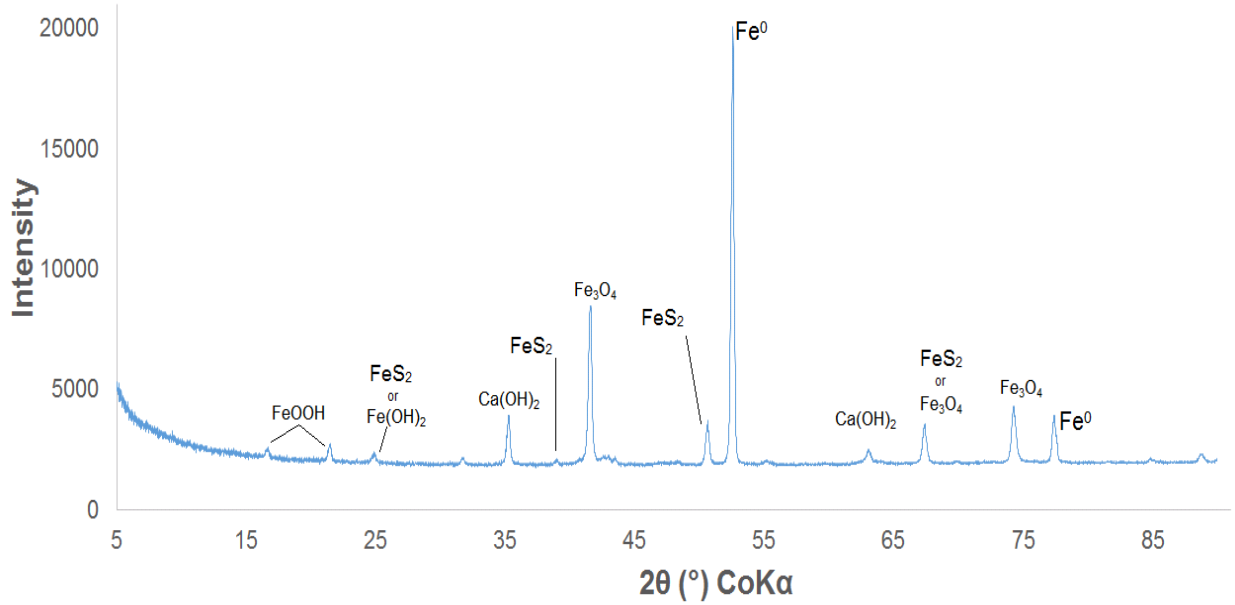

Figure 5.34: XRD of mZVI powder, taken from the AC_Ca-$MgSO_4$ solution after 145 days

5.4 Conclusion

Micro-ZVI was able to create optimal conditions for the reduction of sulfate (S^{VI}) to sulfide (S^{I-}), in the form of pyrite (FeS_2), for the solutions containing Ca, Mg or a combination of Ca and Mg. Furthermore, ZVI was able to remove S, Ca & Mg from each solution, where the ALK_$CaSO_4$ solution showed the greatest sorption of S (19.58 mmol kg^{-1}) and Ca (17.87 mmol kg^{-1}). Followed by the AC_Ca-$MgSO_4$ solution's sorption of S (15.37 mmol kg^{-1}), Ca (5.93 mmol kg^{-1}) and Mg (10.68 mmol kg^{-1}). Lastly, the AC_$MgSO_4$ solution showed the third biggest sorption of S (14.57 mmol kg^{-1}) and Mg (14.76 mmol kg^{-1}).

This suggested that Ca removal, by ZVI, worked better in alkaline solutions. For $MgSO_4$ and Ca-$MgSO_4$ solutions, removal of Mg worked better in acidic solutions. Dissolved Fe

concentrations were found to be the highest in solutions that were initially acidic, especially when they contained Mg or the combination of Ca and Mg. Furthermore, solutions containing Mg also showed lower ratios of Fe^{3+}/Fe_{Tot} compared to solutions that contained Ca.

CHAPTER 6: SYNTHESIS

6.1 Summary

ZVI is a reductant for SO_4^{2-} in the absence of stronger electron acceptors such as oxygen and so the experimental set-up also needed to keep oxygen ingress during the experiment low. Literature detailing the methodology on Ar purging was sparse. This study therefore started-off with a revisit of the methodology for oxygen purging with Ar. This also established a detailed understanding of oxygen solubility and the impact of Ca^{2+} and Mg^{2+} in different salt solutions ($CaSO_4$, $MgSO_4$ & Ca-$MgSO_4$) used in this study. The method was quite effective and was able to remove 98% DO from de-ionized water and sulfate solutions. In Chapter 4, the aim was to investigate whether desired experimental conditions of low redox potentials could be created and maintained for the various sulfate solutions. It was verified that purging DO from a solution decreased the E_h for ZVI-sulfate systems. The reduced conditions created ranged between -200 mV and -500 mV, which was an important requirement for SO_4^{2-} reduction. Zero-valent iron is a strong reducing agent and in a small and isolated system, without DO, it would quickly induce low redox potentials. The benefit of purging DO beforehand was restricted to the first 6 hours, also a result of the small volumes used. Furthermore, ZVI increased and buffered the pH for the DWs at 10, however, the pH of the $CaSO_4$, $MgSO_4$ and Ca-$MgSO_4$ solutions were buffered close to neutral conditions regardless of the solutions E_h (≤ -200 mV).

The goal of Chapter 5 was to investigate the removal of S and its counter ions, Ca and Mg. Furthermore, the conditions (pH & EC) created by ZVI were also investigated. Broadly the ac and AC solutions, regardless of containing Ca^{2+}, Mg^{2+} or [Ca^{2+}+Mg^{2+}], at 3.12 *mM* and 12.5 *mM* ZVI were characterized by rapidly increasing pH (initial pH of 4) within 24 hours. Typically, the pH for the $MgSO_4$ solutions and the Ca-$MgSO_4$ solution, were buffered between 6 and 7, while the $CaSO_4$ solutions were buffered between 7 and 8.2. The redox potentials for the $CaSO_4$ solutions, within the first 24 hours, were low (-400 mV to -387 mV) but increased throughout the experiment (-330 mV to -228 mV), but conditions were still conducive of SO_4^{2-} reduction. The redox potentials for the $MgSO_4$ solutions and the Ca-$MgSO_4$ solutions decreased below -300 mV and continued to decrease when the eventual buffered pH was reached. S sorption, for the $MgSO_4$ and

Ca-$MgSO_4$ solutions, were less than Ca or Mg sorption in the first 20 days but was similar to Ca and/or Mg sorption, or surpassed Ca and/or Mg sorption, after day 120. For the solutions at 3.12 *mM*, S sorption was lower than for the solutions at 12.5 *mM*. Ca sorption was greater than Mg sorption for solutions at 3.12 *mM*, however, the opposite was observed for the solutions at 12.5 *mM*.

The highest concentrations of dissolved Fe with the lowest Fe^{3+}/Fe_{tot} ratios were generally found for the ac and AC solutions. The fundamental difference between the ac and AC was that the dissolved Fe^{2+} concentration was far greater for the AC solutions because of the higher concentration of electron acceptors. XRD analyses showed pyrite was the only mineral detected on mZVI's surfaces for the AC_$MgSO_4$ solution. However, on mZVI's surfaces from the AC_Ca-$MgSO_4$ and the ALK_$CaSO_4$ solution, both containing Ca, there was magnetite and goethite identified together with pyrite. XRD analyses were only performed on the ALK_$CaSO_4$, AC_$MgSO_4$, and AC_Ca-$MgSO_4$ solutions because they showed the highest sorption of S, Ca and Mg.

The alk and ALK solutions, regardless of containing Ca, Mg or [Ca^{2+}+Mg^{2+}], at 3.12 and 12.5 *mM*, also showed an increase in pH (initial pH of 8) in the first 24 hours. The pH for the $MgSO_4$ solutions and the Ca-$MgSO_4$ solution was buffered in the same range (7 - 8.2), while the $CaSO_4$ solutions were buffered between 8 and 9. The buffered pH for the alk and ALK solutions were more or less one unit higher than the ac and AC solutions during experimentation. The $CaSO_4$ solutions also reached low redox potentials (-318 mV to -314 mV) which were also higher for the corresponding ac and AC solutions, within the first 24 hours, and increased throughout the experiment (-298 mV to -258 mV). However, conditions were still conducive for SO_4^{2-} reduction. This increase in redox potential was also observed for the ac_$CaSO_4$ and AC_$CaSO_4$ solutions. The redox potentials for the $MgSO_4$ solutions and the Ca-$MgSO_4$ solution decreased below -300 mV at the eventual buffered pH and was conducive of SO_4^{2-} reduction. The ALK solutions containing Mg achieved the lowest redox potentials, with the ALK_Ca-$MgSO_4$ solution obtaining a redox potential of -421 mV.

S sorption occurred at equimolar rates to Ca and/or Mg sorption for the alk and ALK solutions. However, for the solution at 3.12 *mM*, S sorption was lower than for the solutions at 12.5 *mM*. Ca sorption was greater than Mg sorption in the 3.12 *mM* and 12.5 *mM* solutions. Over-all, the alk and ALK solutions showed higher S sorption compared to the ac and AC solutions, except for the alk and ALK solutions containing Mg, which showed the lowest removal of S.

Generally, the alk and ALK solutions contained the lowest concentrations of dissolved Fe compared to the ac and AC solutions, however, the alk and ALK solutions had the highest Fe^{3+}/Fe_{tot} ratios. Previously stated, XRD analyses were only performed on the ALK_$CaSO_4$, AC_$MgSO_4$, and AC_Ca-$MgSO_4$ solutions and so it cannot be definitively stated that Mg inhibited Fe oxide formation. However, with $Ca(OH)_2$ reported (XRD analyses) it appears that Ca complexes lead to hydroxide stabilisation and Fe oxide precipitation while Mg complexes are too labile.

When focussing on the $CaSO_4$, $MgSO_4$ and Ca-$MgSO_4$ solutions, the following solution specific properties were observed. Over-all, for the $CaSO_4$ solutions, the pH increased to more alkaline conditions (above 7), within 24 hours, and after 145 days the pH was near or at 9. The lowest potential (-330 mV) was recorded for the AC_$CaSO_4$ solution and the ac_ $CaSO_4$ had the highest potential (-228 mV). The rise in pH and increase in E_h was owed to Ca precipitating on ZVI's surface, slowly pacifying ZVI. Both S and Ca sorption in the $CaSO_4$ solutions were mainly influenced by the initial alkalinity and concentration and was shown in decreasing order; ALK_$CaSO_4$ > AC_$CaSO_4$ > alk_$CaSO_4$ > ac_$CaSO_4$.

The $MgSO_4$ solutions' pH (initially acidic or alkaline) stabilised between 6 and 8. The redox potentials in the $MgSO_4$ solutions, after day 1, were close to or below -300 mV and decreased. After experimentation, the ALK_$MgSO_4$ solution had the lowest redox potential (-385 mV). While both the ac_ $MgSO_4$ and AC_ $MgSO_4$ solutions recorded the highest potentials (approximately -340 mV). The pH was buffered between 6 and 8 and decrease in E_h was owed to Mg forming more soluble complexes on ZVI's surface than

Ca, leaving ZVI more reactive. Both S and Mg sorption for the $MgSO_4$ solutions were mainly influenced by the initial acidity and concentration and was shown in decreasing order; AC_$MgSO_4$ > ALK_$MgSO_4$ > ac_$MgSO_4$ > alk_$MgSO_4$.

For the AC_Ca-$MgSO_4$ solution the pH was buffered between 6 and 7, more or less one unit lower than ALK_Ca-$MgSO_4$ solution. Furthermore, the AC_Ca-$MgSO_4$ solution was the only solution where the pH continuously decreased, after its initial increase. The redox potential of the AC_Ca-$MgSO_4$ solution, after day 1, was below -200 mV and the ALK_Ca-$MgSO_4$ solution was below -300 mV. Irrespective of Ca in solution, the redox potential of both Ca-$MgSO_4$ solutions continued to decrease during experimentation. Furthermore, the ALK_Ca-$MgSO_4$ solution produced the lowest redox potential (-421 mV) and had over-all the lowest redox potential compared to all the treatments. S sorption, by ZVI, for the AC_Ca-$MgSO_4$ solution was 13 times greater than for the ALK_Ca-$MgSO_4$ solution because pyrite precipitation occurred at a higher rate, followed by Mg sorption. S sorption was shown in decreasing order; AC_Ca-$MgSO_4$ > ALK_Ca-$MgSO_4$. Mg sorption was greater than Ca sorption in the AC_Ca-$MgSO_4$ solution, benefited by the initial acidity in the solution and in the ALK_Ca-$MgSO_4$ solution Ca sorption was greater than Mg sorption. The sorption of S, for all the solutions, were shown in decreasing order. Followed by Ca sorption in decreasing order, and lastly, Mg sorption (Table 6.1).

Table 6.1: Sorption behaviour of S, Ca, and Mg in the different solutions investigated

Element	Decreasing Trend
S	ALK_$CaSO_4$>AC_Ca-$MgSO_4$>AC_$MgSO_4$>AC_$CaSO_4$>alk_$CaSO_4$> ac_$CaSO_4$>ALK_$MgSO_4$>ac_$MgSO_4$>alk_$MgSO_4$>ALK_Ca-$MgSO_4$
Ca	ALK_$CaSO_4$>AC_$CaSO_4$>alk_$CaSO_4$>AC_Ca-$MgSO_4$>ac_$CaSO_4$> ALK_Ca-$MgSO_4$
Mg	AC_$MgSO_4$>AC_Ca-$MgSO_4$>ALK_$MgSO_4$>ac_$MgSO_4$>alk_$MgSO_4$> ALK_Ca-$MgSO_4$

6.2 Practical Simulation

Sorption data from the Ca-$MgSO_4$ solutions were used to determine how much ZVI would be needed to remove 5%, 10% and 20% S, Ca, and Mg from a cubic meter of saline mine water (1000 l) (Table 6.1). These percentages were chosen because in practice low removal rates are more likely to be expected. This was the best way to conclude how effective S, Ca and Mg sorption by mZVI would be, using calculations presented by Equations 6.1 and 6.2;

$$C_{target} = [C_{solx}*(C_{\%}/100)]*1000 \quad (6.1)$$

$$ZVI_{req} = C_{target}/ZVI_{sorbcap} \quad (6.2)$$

Where C_{target} is the concentration (mmol m^{-3}) of S, Ca or Mg to be removed by ZVI. C_{solx} is the solution's initial concentration (mmol l^{-1}) of S, Ca or Mg and $C_{\%}$ is the percentages of S, Ca and Mg that needs to be removed. The ZVI required (ZVI_{req}) to remove the percentages of S, Ca and Mg is calculated by dividing C_{target} by the sorption capacity of ZVI ($ZVI_{sorbcap}$), which was the sorbed concentration of S, Ca or Mg (mmol kg^{-1} ZVI) after 20 days and 145 days. The Ca:Mg molar ratio is 1:1 and was best suited for simulating mine water as it is closest to the current water quality. Furthermore, data from day 20 and day 145 was used to compare a short period of the treatment to a longer period. Lastly, there were no ac_Ca-$MgSO_4$ and alk_Ca-$MgSO_4$ solutions created as the combination of a Ca-Mg sulfate solution at 3.12 *mM* was not in the scope of this study.

Table 6.2: Zero-valent iron (tonnes m^{-3}) required to remove S, Ca, and Mg per m^{-3}

	Day 20			Day 145		
AC_Ca-MgSO$_4$						
	S	**Ca**	**Mg**	**S**	**Ca**	**Mg**
5%	1.98E-01	2.05E-01	1.64E-01	4.00E-02	5.20E-02	2.90E-02
10%	3.96E-01	4.11E-01	3.28E-01	8.10E-02	1.05E-01	5.80E-02
20%	7.93E-01	8.22E-01	6.57E-01	1.62E-02	2.10 E-01	1.16E-01
ALK_Ca-MgSO$_4$						
	S	**Ca**	**Mg**	**S**	**Ca**	**Mg**
5%	1.136	8.68E-01	1.202	5.43E-01	4.22E-01	8.68E-01
10%	2.273	1.736	2.404	1.087	8.44E-01	1.736
20%	4.546	3.472	4.808	2.174	1.689	3.472

For the AC_Ca-MgSO$_4$ solution it was calculated that 198 to 793 kg ZVI per cubic meter of water is required to remove 5 to 20% S, in 20 days. More ZVI was required to remove Ca (205 to 822 kg ZVI m^{-3}) compared to S, and less ZVI was required to remove Mg (164 to 657 kg ZVI m^{-3}). Removing 5 to 20% S in 145 days, however, required far less ZVI (40 to 162 kg ZVI m^{-3}). ZVI required to remove Ca (52 to 210 kg ZVI m^{-3}) and Mg (29 to 116 kg ZVI m^{-3}) over a longer period (145 days) was also less. For the ALK_Ca-MgSO$_4$ solution it was calculated that 1.136 to 4.546 tonnes of ZVI will be required to remove 5% to 20% S, in 20 days. Removing Ca at these percentages requires less ZVI (868 kg to 3.472 tonnes ZVI m^{-3}). Removing Mg at 5%, 10% or 20% requires slightly more ZVI (1.202 to 4.808 tonnes ZVI m^{-3}) than for S. Removing 5 to 20% S at a longer period (145 days) also required far less ZVI (543 kg to 2.174 tonnes ZVI m^{-3}), just like the AC_Ca-MgSO$_4$. ZVI required to remove Ca (422 kg to 1.689 tonnes ZVI m^{-3}) and Mg (868 kg to 3.472 tonnes ZVI m^{-3}) over this period was also less. The difference between 20 days and 145 days for both AC and ALK solutions showed mZVI removed S, Ca and Mg more efficiently at longer periods (145 days) compared to shorter period (20 days) underlining the efficacy of ZVI for passive treatments. Over-all, ZVI in a solution that starts at pH = 4 will be more effective, especially if the aim is to remove Mg. For solution starting at pH = 8, the removal of S, Ca and Mg will require appreciably more ZVI per cubic meter of water.

6.3 Conclusions and Recommendations

The data shows that salinity of mine water might be enough to decrease oxygen levels in water if there is no active oxidation such as water flow. The $CaSO_4$, $MgSO_4$ and Ca-$MgSO_4$ solutions attained different minimum redox potentials. Ca precipitation restricted low redox potentials and Mg did not. However, the combination of Ca and Mg was responsible for, and maintained the lowest redox potentials in the solutions.

Micro-ZVI was able to create optimal conditions for the reduction of sulfate (S^{VI}) to presumably sulfide (S^{II-}), in the form of pyrite. XRD analyses performed on selected samples, showed that pyrite was visible on ZVI's surface, together with magnetite, goethite, and calcium hydroxide. However, pyrite was the only mineral detected for the AC_$MgSO_4$ solution.

Ca removal by mZVI, at higher concentrations (6 *mM* to 12.5 *mM*), would be more effective in slightly alkaline to alkaline mine water. While Mg sorption (6 *mM* to 12.5 *mM*) would be more beneficial for slightly acidic to acidic mine water. Sulfate can be easily reduced by biological activities, together with ZVI to precipitate FeS_2. The ZVI can be washed and de-pacified with an acid solution to be re-used. The acidity of the washed solution can be decreased to safer levels and used for irrigation water in soils with acidic subsoils.

The next step, after the experiments performed, is to test the effectiveness of ZVI for S removal in real mine water samples. Increasing the scale of the experiment, where mine water flows through ZVI columns, quantifying the removal of constituents.

REFERENCES

AKCIL, A., & KOLDAS, S. 2006. Acid Mine Drainage (AMD): causes, treatment and case studies. *Journal of Cleaner Production*, *14*(12), 1139-1145.

ANNANDALE, J.G., JOVANOVIC, N.Z., HODGSON F.D.I., USHER, B.H., AKEN, M.E., VAN DER WESTHUIZEN, A.M., BRISTOW, K.L. & STEYN, J.M. 2006. Prediction of the environmental impact and sustainability of large-scale irrigation with gypsiferous mine-water on groundwater resources. *Water SA*, *32*(1), 21-28.

BENSON, B. B., & KRAUSE, D. 1984. The concentration and isotopic fractionation of oxygen dissolved in freshwater and seawater in equilibrium with the atmosphere1. *Limnology and Oceanography*, *29*(3), 620-632.

BIGGS, H. C., CLIFFORD-HOLMES, J. K., FREITAG, S., VENTER, F. J., & VENTER, J. 2017. Cross-scale governance and ecosystem service delivery: A case narrative from the Olifants River in north-eastern South Africa. *Ecosystem Services*, *28*(B), 173-184.

BLOWES, D. W., PTACEK, C. J., BENNER, S. G., MCRAE, C. W. T., BENNETT, T. A., & PULS, R. W. 2000. Treatment of inorganic contaminants using permeable reactive barriers. *Journal of Contaminant Hydrology*, *45*(1), 123-137.

BOWELL, R., DILL, S., COWAN, J., & WOOD, A. 2004. A review of sulfate removal options for mine waters. *Proceedings of mine water*, 75-88.

BROG, J,, CHANEZ, C., CROCHET, A., & FROMM KM. 2013. Polymorphism, what it is and how to identify it: a systematic review. *RSC Advances*, *3*(38), 16905.

BROWN, T. L., LEMAY JR, E., BURSTEN, B. E., LANGFORD, S. J., SAGATYS, D. S., & DUFFY, D. N. 2006. *Chemistry, The Central Science: A Broad Perspective*. Pearson Australia Group, pp 398-441.

BUTLER, I. B., & RICKARD, D. 2000. Framboidal pyrite formation via the oxidation of iron (II) monosulfide by hydrogen sulphide. *Geochimica et Cosmochimica Acta*, *64*(15), 2665-2672.

CHANG, R. 2008. *General Chemistry: The essential concepts.* The McGraw-Hill Companies, Inc., pp 6, 10, 133-159.

CHEKLI, L., BAYATSARMADI, B., SEKINE, R., SARKAR, B., SHEN, A. M., SCHECKEL, K. G., SKINNER, W., NAIDU, R., SHON, H. K., LOMBI, E., & DONNER, E. 2016. Analytical characterisation of nanoscale zero-valent iron: A methodological review. *Analytica Chimica Acta*, *903*, 13-35.

COLEMAN, T., & SOUTH AFRICA. WATER RESEARCH, C. 2011. *Prediction of how different management options will affect drainage water quality and quantity in the Mpumalanga coal mines up to 2080 : report to the Water Research Commission*. WRC Report No. 1628/1/11: 33-51.

DELUANE, R.D., & REDDY, K.R. 2005. *Redox potential*. Elsevier Ltd., 366-371.

DENIS, L., MARAT, T., DMITRY, A., ELIZAVETA, P., EVGENY, K., & DENIS, K. 2019. Effect of Initial Salt Composition on Physicochemical and Structural Characteristics of Zero-Valent Iron Nanopowders Obtained by Borohydride Reduction. *Processes*, *10*, 769.

DWS (Department: Water and Sanitation). 2013. Surface water quality analysis of rivers in South Africa (1992 – 2012). http://www.dws.gov.za.

DOU, W., ZHOU, Z., JIANG, L.-M., JIANG, A., HUANG, R., TIAN, X., ZHANG, W., & CHEN, D. 2017. Sulfate removal from wastewater using ettringite precipitation: Magnesium ion inhibition and process optimization. *Journal of Environmental Management*, *196*, 518-526.

EATON, A. D., CLESCERI, L. S., GREENBERG, A. E., FRANSON, M. A. H., AMERICAN PUBLIC HEALTH, A., AMERICAN WATER WORKS, A., & WATER ENVIRONMENT, F. 1998. *Standard methods for the examination of water and wastewater* (20th ed. 1998. ed.). American Public Health Association.

ELLIOTT, D. W., & ZHANG, W. X. 2001. Field assessment of nanoscale bimetallic particles for groundwater treatment. *Environmental science & technology*, *35*(24), 4922-4926.

ESSINGTON, M. E. 2004. *Soil and water chemistry : an integrative approach*. Boca Raton: CRC Press, pp 448.

FATHINIA, S., FATHINIA, M., RAHMANI, A. A., & KHATAEE, A. 2015. Preparation of natural pyrite nanoparticles by high energy planetary ball milling as a nanocatalyst for heterogeneous Fenton process. *Applied Surface Science*, *327*, 190-200.

FILIP, J., KARLICKÝ, F. E., MARUŠÁK, Z. K., LAZAR, P., ČERNÍK, M., OTYEPKA, M., & ZBOŘIL, R. 2014. Anaerobic Reaction of Nanoscale Zerovalent Iron with Water: Mechanism and Kinetics. *The Journal of Physical Chemistry C*, *118*(25), 13817-13825.

FU, F., DIONYSIOU, D. D., & LIU, H. 2014. The use of zero-valent iron for groundwater remediation and wastewater treatment: A review. *Journal of Hazardous Materials*, *267*, 194-205.

FUJIOKA, N., SUZUKI, M., KUROSU, S., & KAWASE, Y. 2016. Linkage of iron elution and dissolved oxygen consumption with removal of organic pollutants by nanoscale zero-valent iron: Effects of pH on iron dissolution and formation of iron oxide/hydroxide layer. *Chemosphere*, *144*, 1738-1746.

FURUKAWA, Y., KIM, J. W., WATKINS, J., & WILKIN, R. T. 2002. Formation of ferrihydrite and associated iron corrosion products in permeable reactive barriers of zero-valent iron. *Environmental science & technology*, *36*(24), 5469-5475.

GARCIA, H. E., & GORDON, L. I. 1992. Oxygen solubility in seawater: Better fitting equations. *Limnology and Oceanography*, *37*(6), 1307-1312.

GELDENHUYS, A.J., MAREE, J.P., DE BEER, M., & HLABELA P. 2003. An integrated limestone/lime process for partial sulphate removal. *Journal of the Southern African Institute of Mining and Metallurgy*, *103*(6), 345-353.

GENG, M., & DUAN, Z. 2010. Prediction of oxygen solubility in pure water and brines up to high temperatures and pressures. *Geochimica et Cosmochimica Acta*, *74*(19), 5631-5640.

GHICA, D., VLAICU, I. D., STEFAN, M., NISTOR, L. C., & NISTOR, S. V. 2016. On the agent role of Mn2+ in redirecting the synthesis of Zn(OH)2 towards nano-ZnO with variable morphology Electronic supplementary information (ESI) available. See DOI: 10.1039/c6ra23065b. *RSC Advances*, *6*(108), 106732-106741.

GORSKI, C. A., NURMI, J. T., TRATNYEK, P. G., HOFSTETTER, T. B., & SCHERER, M. M. 2010. Redox behavior of magnetite: implications for contaminant reduction. *Environmental science & technology*, *44*(1), 55-60.

GUAN, X., SUN, Y., QIN, H., LI, J., LO, I. M., HE, D., & DONG, H. 2015. The limitations of applying zero-valent iron technology in contaminants sequestration and the corresponding countermeasures: The development in zero-valent iron technology in the last two decades (1994-2014). *Water research.*, *75*, 224-248.

HAMME, R. C., & EMERSON, S. R. 2004. The solubility of neon, nitrogen and argon in distilled water and seawater. *Deep-Sea Research Part I*, *51*(11), 1517-1528.

INEICH, T., DEGREVE, C., KARAMOUTSOS, S., & DU PLESSIS, C. 2017. Utilization efficiency of lime consumption during magnesium sulfate precipitation. *Hydrometallurgy*, *173*, 241-249.

JANSEN, H., & LANCASTER, J. 2012. Kriel Colliery Amended EMP for borehole drilling In the proposed Opencast area. SRK Consulting. Report Number 410173/Borehole EMP: 1-42.

JEFFREY, L. S. 2005. Characterization of the coal resources of South Africa. *Journal of the South African Institute of Mining and Metallurgy: SAIMM*, *105*(2), 95-102.

JOHNSON, M., VAN VUUREN, C., HEGENBERGER, W., KEY, R., & SHOW, U. 1996. Stratigraphy of the Karoo Supergroup in southern Africa: an overview. *Journal of African Earth Sciences*, *23*(1), 3-15.

JOLIVET, J., CHANÉAC, C., & TRONC, E. 2004. Iron oxide chemistry. From molecular clusters to extended solid networks. *Chemical Communications*, *2004*(5), 477-483.

JONES, A. M., GRIFFIN, P. J., COLLINS, R. N., & WAITE, T. D. 2014. Ferrous iron oxidation under acidic conditions - The effect of ferric oxide surfaces. *Geochimica et Cosmochimica Acta*, *145*, 1-12.

KADLEC, R. H., & WALLACE, S. D. 2009. *Treatment wetlands, Second Edition*. CRC Press, pp 150.

KARRI, S., SIERRA-ALVAREZ, R., & FIELD, J. A. 2005. Zero valent iron as an electron-donor for methanogenesis and sulfate reduction in anaerobic sludge. *Biotechnology and Bioengineering*, *92*(7), 810-819.

KEENAN, C. R., & SEDLAK, D. L. 2008. Factors affecting the yield of oxidants from the reaction of nanoparticulate zero-valent iron and oxygen. *Environmental science & technology*, *42*(4), 1262-1267.

LANCASTER, J., & CANDY, B. 2012. Kriel Colliery beneficiation plant environmental management programme: Final scoping report. SRK Consulting. Report no. 436368/FSR: 1 - 112.

LEE, H., LEE, H.J., KIM, H.E., KWEON, J., LEE, B.D., & LEE, C. 2014. Oxidant production from corrosion of nano- and microparticulate zero-valent iron in the presence of oxygen: A comparative study. *Journal of Hazardous Materials*, *265*, 201-207.

LI, H., WAN, J., MA, Y., HUANG, M., WANG, Y., & CHEN, Y. 2014. New insights into the role of zero-valent iron surface oxidation layers in persulfate oxidation of dibutyl phthalate solutions. *Chemical Engineering Journal*, *250*, 137-147.

LIMPER, D., FELLINGER, G.P., EKOLU, S.O. 2018. Evaluation and microanalytical study of ZVI/zeolite substrate mixtures for treating acid mine drainage using reactive barriers - removal mechanisms. *Journal of Environmental Chemical Engineering, 6*(5), 6184-6193.

LING, L., PAN, B., & ZHANG, W. 2015. Removal of selenium from water with nanoscale zero-valent iron: Mechanisms of intraparticle reduction of Se(IV). *Water research.*, *71*, 274-281.

LIU, T., LI, X., & WAITE, T. D. 2013a. Depassivation of aged Fe0 by ferrous ions: implications to contaminant degradation. *Environmental science & technology*, *47*(23), 13712-13720.

LIU, T., LI, X., & WAITE, T. D. 2013b. Depassivation of aged Fe0 by inorganic salts: implications to contaminant degradation in seawater. *Environmental science & technology*, *47*(13), 7350-7356.

LIU, T., LI, X., & WAITE, T. D. 2014. Depassivation of aged Fe0 by divalent cations: Correlation between contaminant degradation and surface complexation constants. *Environmental Science and Technology*, *48*(24), 14564-14571.

LIU, Y., ZHANG, Y., & NI, B.J. 2015. Zero valent iron simultaneously enhances methane production and sulfate reduction in anaerobic granular sludge reactors. *Water Research*, *75*, 292-300.

MANSOUR, C., LEFÈVRE, G., PAVAGEAU, E. M., CATALETTE, H., FÉDOROFF, M., & ZANNA, S. 2009. Sorption of sulfate ions onto magnetite. *Journal of Colloid And Interface Science*, *331*(1), 77-82.

MCCARTHY, T. S., & PRETORIUS, K. 2009. Coal mining on the Highveld and its implications for future water quality in the Vaal River system. International Mine Water Conference. Proceedings ISBN Number: 978-0-9802623-5-3 Pretoria, South Africa. Produced by: Document Transformation Technologies, 56-65.

MHLONGO, S. P., MATIVENGA, P. T., & MARNEWICK, A. 2018. Water quality in a mining and water-stressed region. *Journal of Cleaner Production*, *171*, 446-456.

MIAO, Z., BRUSSEAU, M. L., CARROLL, K. C., CARREON-DIAZCONTI, C., JOHNSON, B., & PACIFIC NORTHWEST NATIONAL LAB, R. W. A. 2012. Sulfate Reduction in Groundwater: Characterization and Applications for Remediation. *Environmental Geochemistry and Health*, *34*(4).

MIZUTANI, N., IWASAKI, T., WATANO, S., YANAGIDA, T., TANAKA, H., & KAWAI, T. 2008. Effect of ferrous/ferric ions molar ratio on reaction mechanism for hydrothermal synthesis of magnetite nanoparticles. *Bulletin of Materials Science*, *31*(5), 713-717.

MKWELO, S. T., & VILLIERS, S. D. 2009. Has monitoring failed the Olifants River, Mpumalanga? *Water SA*, *35*(5), 671-676.

MU, Y., JIA, F., AI, Z., & ZHANG, L. 2017. Iron oxide shell mediated environmental remediation properties of nano zero-valent iron. *Environmental Science: Nano*, *4*(1), 27-45.

NOUBACTEP, C. 2008. A critical review on the process of contaminant removal in Fe0-H2O systems. *Environmental technology*, *29*(8), 909-920.

NOUBACTEP, C. 2009a. An analysis of the evolution of reactive species in Fe0/H2O systems. *Journal of Hazardous Materials*, *168*(2-3), 1626-1631.

NOUBACTEP, C. 2009b. Metallic iron for environmental remediation: learning from the Becher process. *Journal of Hazardous Materials*, *168*(2-3), 1609-1612.

NOUBACTEP, C. 2015. Metallic iron for environmental remediation: A review of reviews. *Water research.*, *85*, 114-123.

OBERHOLSTER, P. J., & ASHTON, P. J. 2008. State of the nation report: An overview of the current status of water quality and eutrophication in South African rivers and reservoirs. *Parliamentary Grant Deliverable. Pretoria: Council for Scientific and Industrial Research (CSIR)*.

PLESSL, K., RUSS, A., & VOLLPRECHT, D. 2022. Application and development of zero-valent iron (ZVI) for groundwater and wastewater treatment. *International Journal of Environmental Science and Technology*, 1-16.

PELSER, M. 2003. *The control of calcium and magnesium in a base metal sulphate leach solution* Stellenbosch: University of Stellenbosch]. Thesis submitted in partial fulfilment of the requirements for the degree *Of* MASTER OF SCIENCE IN ENGINEERING (EXTRACTIVE METALLURGICAL ENGINEERING) in the Department of Chemical Engineering at the University of Stellenbosch, 18-37.

PULLIN, H., SPRINGELL, R., PARRY, S., & SCOTT, T. 2017. The effect of aqueous corrosion on the structure and reactivity of zero-valent iron nanoparticles. *Chemical Engineering Journal*, *308*, 568-577.

RUBY, C., AÏSSA, R., GÉHIN, A., CORTOT, J., ABDELMOULA, M., & GÉNIN, J.M. 2006. Green rusts synthesis by coprecipitation of FeII-FeIII ions and mass-balance diagram. *Comptes rendus - Géoscience*, *338*(6-7), 420-432.

SPARKS, D. L. 2003. *Environmental soil chemistry, Second Edition*. California: Academic Press, pp 133-185, 247-248.

TANG, C., HUANG, Y. H., ZENG, H., & ZHANG, Z. 2014. Reductive removal of selenate by zero-valent iron: The roles of aqueous Fe2+ and corrosion products, and selenate removal mechanisms. *Water Research*, *67*, 166-174.

TRISZCZ, J. M., PORTA, A., & EINSCHLAG, F. S. G. 2009. Effect of operating conditions on iron corrosion rates in zero-valent iron systems for arsenic removal. *Chemical Engineering Journal*, *150*(2-3), 431-439.

VALDERRAMA, J. O., CAMPUSANO, R. A., & FORERO, L. A. 2016. A new generalized Henry-Setschenow equation for predicting the solubility of air gases (oxygen, nitrogen and argon) in seawater and saline solutions. *Journal of Molecular Liquids*, *222*, 1218-1227.

VAN ZYL, H.C., MAREE, J.P., VAN NIEKERK, A.M., VAN TONDER, G.J. & NAIDOO, C. 2001. Collection, treatment and re-use of mine water in the Olifants River Catchment. *Journal of the Southern African Institute of Mining and Metallurgy*, *101*(1), 41-46.

VELIMIROVIC, M., CARNIATO, L., SIMONS, Q., SCHOUPS, G., SEUNTJENS, P., & BASTIAENS, L. 2014. Corrosion rate estimations of microscale zerovalent iron particles via direct hydrogen production measurements. *Journal of Hazardous Materials*, *270*, 18-26.

WACLAWEK, S., NOSEK, J., CÁDROVÁ, L., ANTOS, V., & CERNIK, M. 2015. Use of various zero valent irons for degradation of chlorinated ethenes and ethanes. *Ecological Chemistry and Engineering*, *22*(4), 577.

WANG, C.B., & ZHANG, W.X. 1997. Synthesizing Nanoscale Iron Particles for Rapid and Complete Dechlorination of TCE and PCBs. *Environmental science & technology*, *31*(7), 2154-2156.

WANG, C.M., BAER, D.R., THOMAS, L.E., AMONETTE, J.E., ANTONY, J., QIANG, Y., & DUSCHER, G. 2005. Void Formation during Early Stages of Passivation: Initial Oxidation of Iron Nanoparticles at Room Temperature. *Journal of Applied Physics*, *98*(9).

WEERASOORIYA, R., & TOBSCHALL, H. J. 2005. Pyrite-water interactions: Effects of pH and pFe on surface charge. *Colloids and Surfaces A: Physicochemical and Engineering Aspects*, *264*(1), 68-74.

WORLD HEALTH ORGANISATION (WHO). 2004a. Fluoride in drinking-water. WHO/SDE/WSH/03.04/96.

WORLD HEALTH ORGANISATION (WHO). 2004b. Sulfate in drinking-water. WHO/SDE/WSH/03.04/114.

XIE, Y. Q. 1994. Electronic structure and properties of pure iron. *Acta Metallurgica et Materialia; (United States)*, *42*(11), 3705-3715.

YAN, W., HERZING, A. A., KIELY, C. J., & ZHANG, W. X. 2010. Nanoscale zero-valent iron (nZVI): aspects of the core-shell structure and reactions with inorganic species in water. *Journal of Contaminant Hydrology*, *118*(3-4), 96-104.

YU, J.Y., HEO, B., CHOI, I.K., CHO, J.P., & CHANG, H.W. 1999. Apparent solubilities of schwertmannite and ferrihydrite in natural stream waters polluted by mine drainage. *Geochimica et Cosmochimica Acta*, *63*(19-20).

ZAGURY, G. J., KULNIEKS, V. I., & NECULITA, C. M. 2006. Characterization and reactivity assessment of organic substrates for sulphate-reducing bacteria in acid mine drainage treatment. *Chemosphere*, *64*(6), 944-954.

ZHANG, T. C., & HUANG, Y. H. 2006. Profiling iron corrosion coating on iron grains in a zerovalent iron system under the influence of dissolved oxygen. *Water Research*, *40*(12), 2311-2320.

APPENDIX A: SUPPLEMENTARY DATA FOR CHAPTER 3

A1: Purging material

a

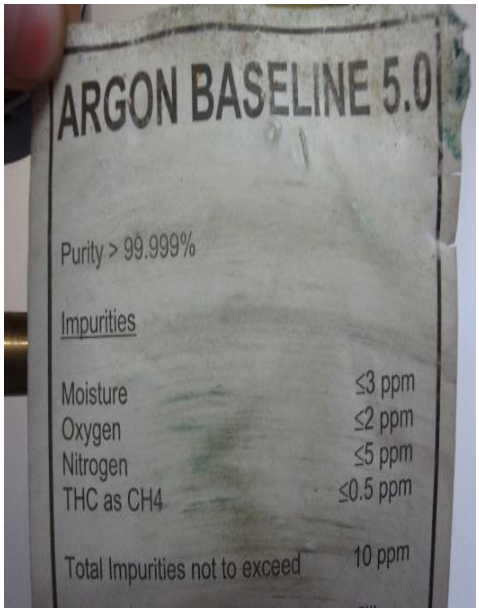

b

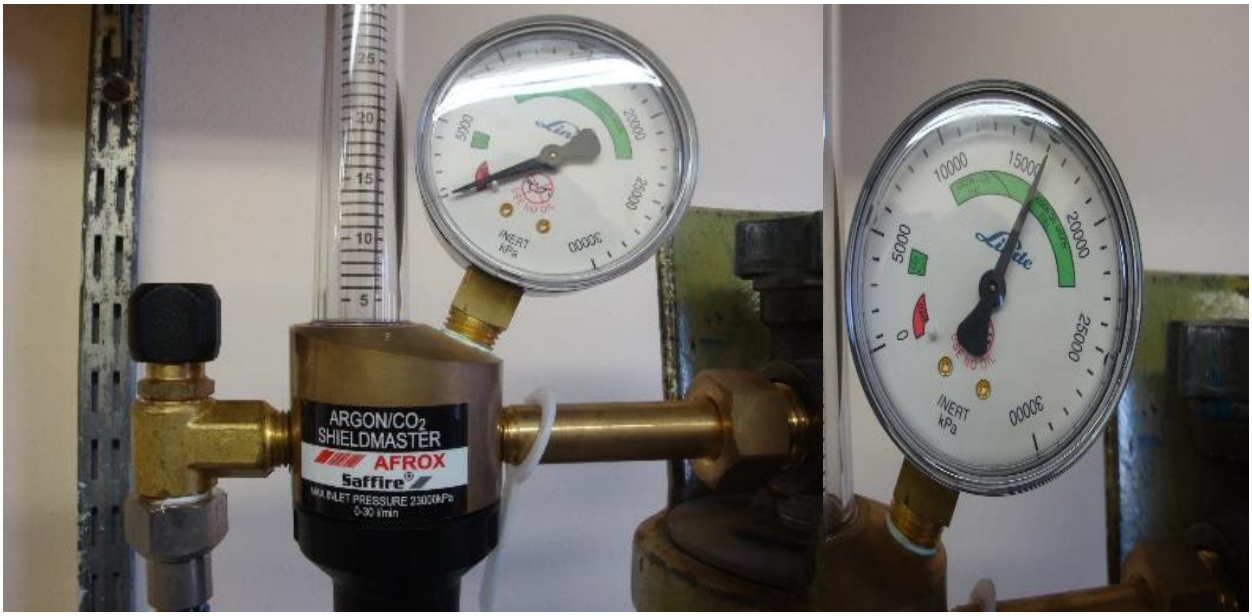

c

Figure 1: The (a) argon gas cylinder, (b) Ar-gas information sheet and (c) pressure gauge

a

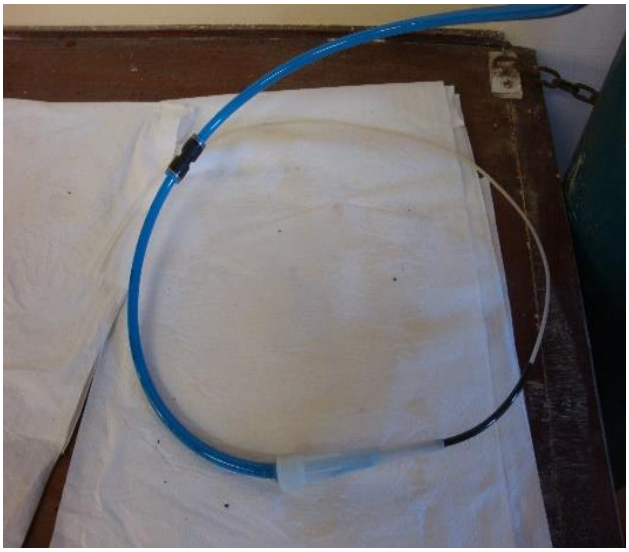

b

c

Figure 2: Experimental set-up (a) used for purging DO with (b) the coupling and tubing connections, where (c) is close-up view of the purging nozzle

a

b

c

Figure 3: Data loggers and probes used to measure; (a) redox potentials, (b) DO and (b) pH & EC

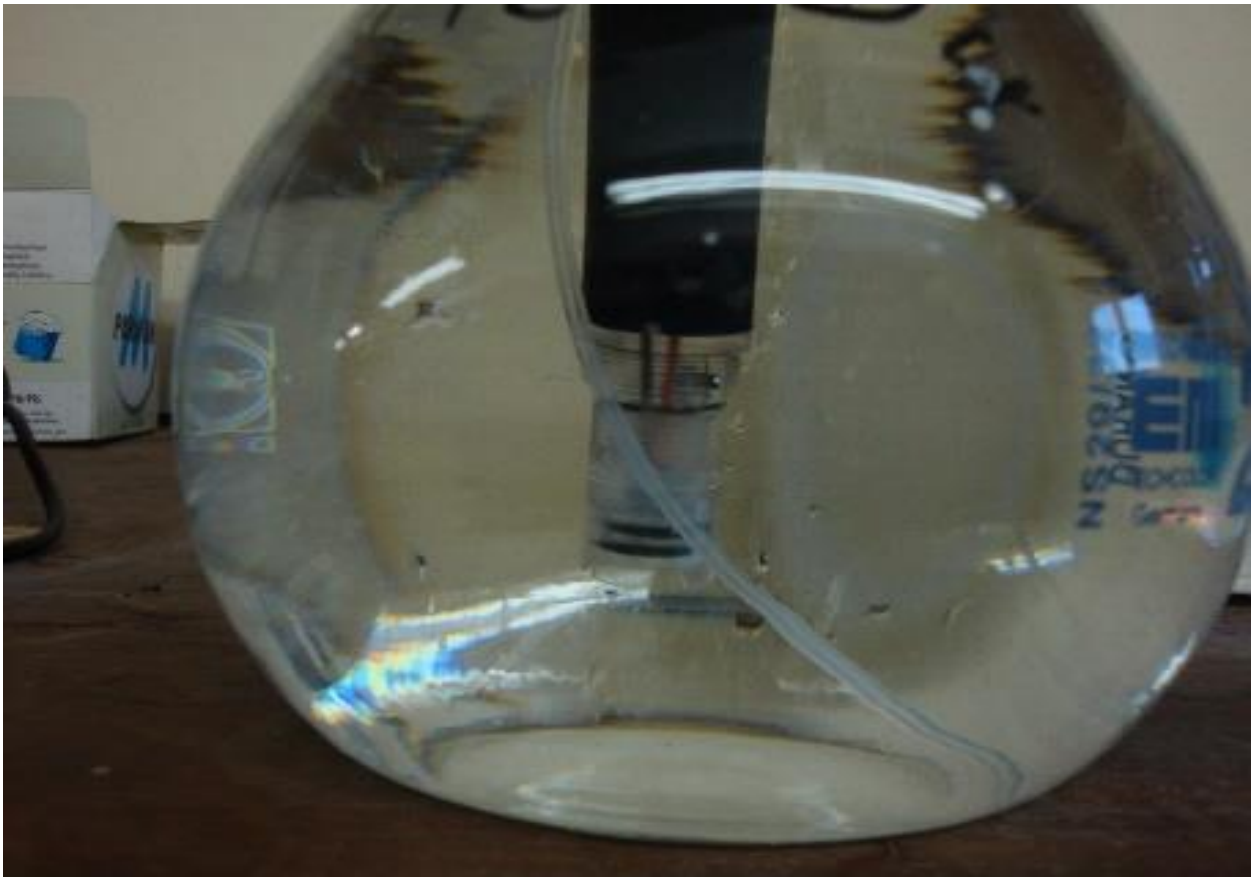

Figure 4: Simultaneous purging and measuring of DO

B2: Statistical analyses of data

Table 1: Results of purging DO from de-ionized water and various sulfate solutions

		Before purge						After purge					
					Average	Standard dev.	CV				Average	Standard dev.	CV
Deionized water	pH	7.10	6.94	6.93	6.99	0.10	1.36	7.12	7.23	7.22	7.19	0.06	0.85
CaSO4	pH	6.34	6.27	6.28	6.30	0.04	0.60	5.86	5.89	5.88	5.88	0.02	0.26
MgSO4	pH	6.03	6.06	6.05	6.05	0.02	0.25	5.92	5.79	5.83	5.85	0.07	1.14
CMS	pH	6.23	6.11	6.27	6.20	0.08	1.34	5.91	5.60	5.60	5.70	0.18	3.14
Deionized water	DO (mg/l)	6.40	6.20	6.40	6.33	0.12	1.82	0.10	0.10	0.10	0.10	0.00	0.00
CaSO4	DO (mg/l)	4.10	3.90	4.20	4.07	0.15	3.76	0.10	0.10	0.10	0.10	0.00	0.00
MgSO4	DO (mg/l)	4.10	4.30	4.10	4.17	0.12	2.77	0.10	0.10	0.10	0.10	0.00	0.00
CMS	DO (mg/l)	4.20	4.00	4.30	4.17	0.15	3.67	0.10	0.10	0.10	0.10	0.00	0.00
Deionized water	EC (µs/cm)	1.09	1.44	1.18	1.24	0.18	14.70	1.45	2.21	0.92	1.53	0.65	42.47
CaSO4	EC (µs/cm)	1829.00	1847.00	1847.00	1841.00	10.39	0.56	1865.00	1887.00	1844.00	1865.33	21.50	1.15
MgSO4	EC (µs/cm)	1861.00	1855.00	1854.00	1856.67	3.79	0.20	1843.00	1850.00	1849.00	1847.33	3.79	0.20
CMS	EC (µs/cm)	1885.00	1882.00	1886.00	1884.33	2.08	0.11	1870.00	1869.00	1871.00	1870.00	1.00	0.05
				1.24									
Deionized water	REDOX (mV)	241.00	244.00	234.00	239.67	5.13	2.14	178.00	181.00	150.00	169.67	17.10	10.08
CaSO4	REDOX (mV)	280.00	279.00	270.00	276.33	5.51	1.99	279.00	294.00	242.00	271.67	26.76	9.85
MgSO4	REDOX (mV)	323.00	328.00	320.00	323.67	4.04	1.25	320.00	330.00	316.00	322.00	7.21	2.24
CMS	REDOX (mV)	327.00	342.00	328.00	332.33	8.39	2.52	318.00	335.00	319.00	324.00	9.54	2.94

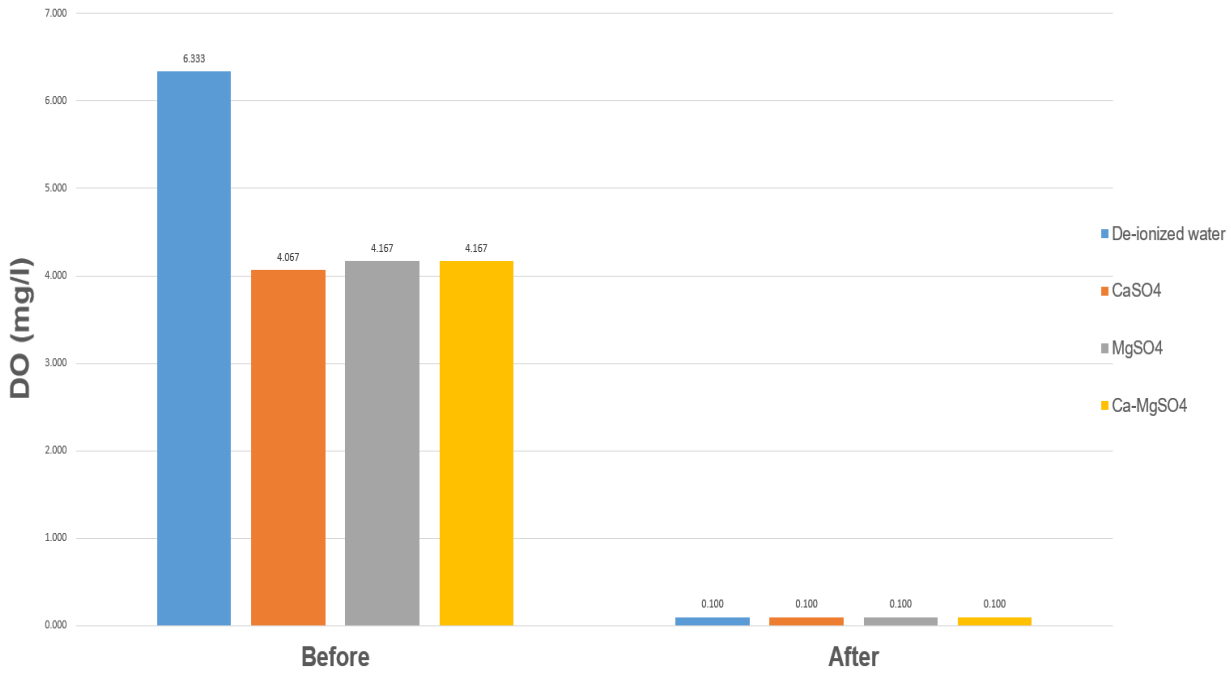

Figure 5: Simplified representation of DO purged from solutions

APPENDIX B: SUPPLEMENTARY DATA FOR CHAPTER 4

B1: Preparation of samples

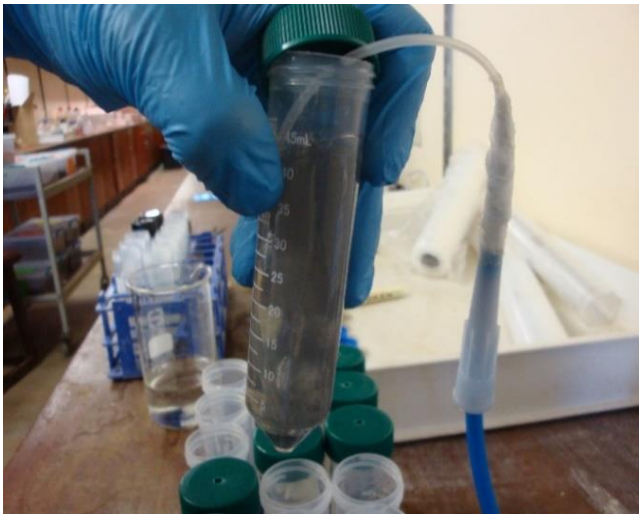

a

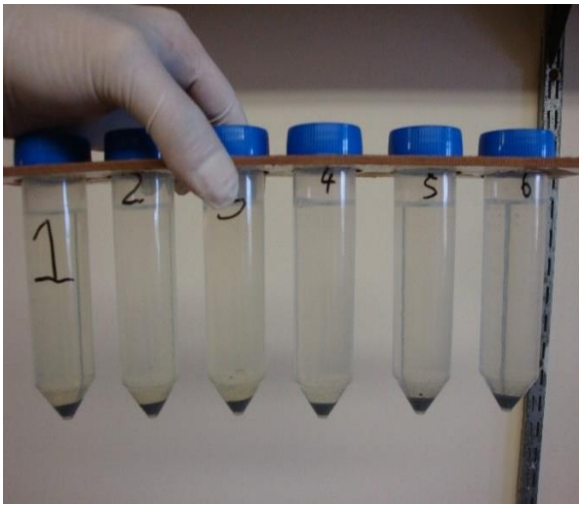

b

c

d

Figure 1: Summarized illustrations of purging (a), arranging (b) vacuum sealing (c) and storing sulfate solutions in batch sorption incubation experiments

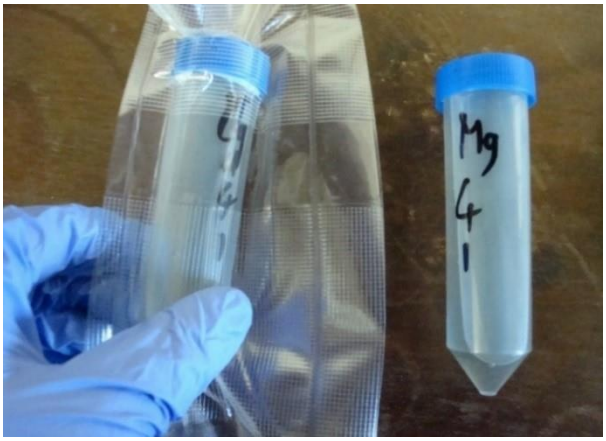

a **b**

Figure 2: The (a) purged, vacuum sealed samples and the (b) unpurged, unsealed samples

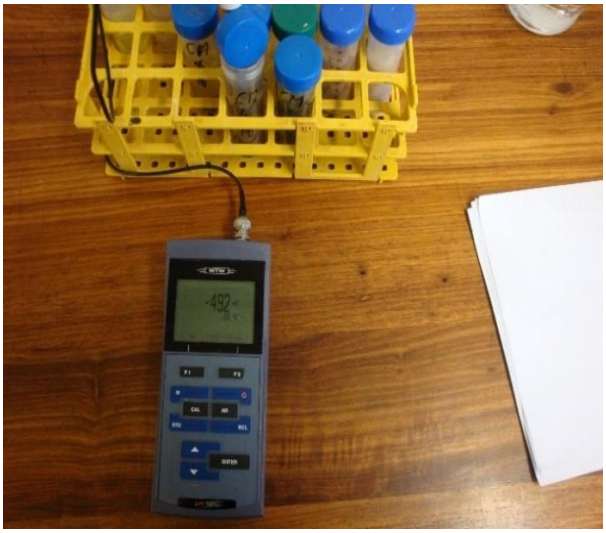

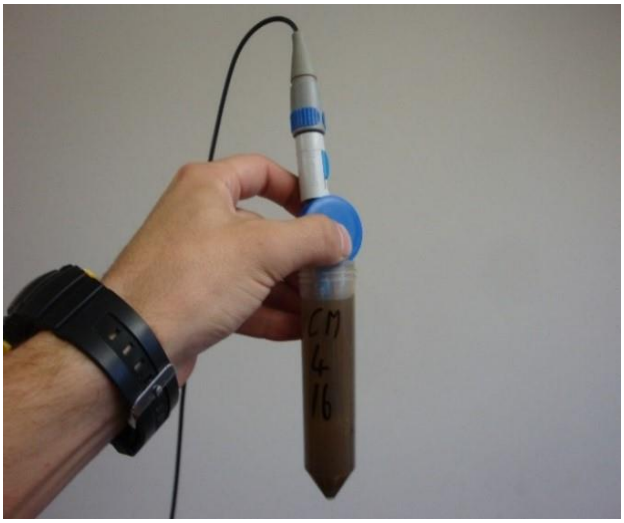

a **b**

Figure 3: Reduction potentials logged by (a) WTW pH 3310 with (b) Sentix Redox probe

B2: Qualitative assessment of pH change under oxic and anoxic mZVI reduction

The change of initial pH of sulfate solutions through mZVI buffering and reduction was investigated and measured. The pH was tested after 6 hours, and again after 30 days. Chapter 4 investigated the evolution of reduction potentials of sulfate solutions over 16 days with the pH only taken on the 16th day. This experiment investigated the behaviour of the sulfate solutions over 30 days (double the incubation period of Chapter 4) to observe how the pH was affected by the buffering capacity of mZVI as it was predicted that mZVI would buffer and maintain the pH of each solutions between 6 and 9.

The same experimental procedure for chapter 4 was followed to prepare sulfate solutions with DO and without DO. Forty millilitres of each sulfate solution, with and without DO was dispensed into 50 ml centrifuge tubes where each sample was adjusted to individual pH values of 2 to 11 with 0.1 M HCl and 0.1 M NaOH respectively. Three sulfate solutions at ten different pH values with DO (retested over 2 days) comprised of 30 solutions. The sulfate solutions, of pH 2 to 11, without DO were individually prepared for each day, and comprised of 60 solutions. Each solution was duplicated producing a total of 180 samples.

Table 1: pH values from unpurged sulfate solutions mixed with mZVI

$CaSO_4$				**$MgSO_4$**			**Ca-$MgSO_4$**		
					PERIOD (DAYS)				
	0	**0.25**	**30**	**0**	**0.25**	**30**	**0**	**0.25**	**30**
pH	2	5.39	5.62	2	7.03	6.20	2	5.58	6.52
	3	5.66	5.95	3	7.09	6.30	3	5.86	6.86
	4	8.57	7.87	4	7.10	6.52	4	7.08	6.61
	5	9.26	7.87	5	8.12	6.65	5	8.34	6.45
	6	9.42	8.17	6	8.18	6.78	6	8.53	6.90
	7	8.71	8.24	7	8.55	6.90	7	8.72	6.39
	8	9.45	8.36	8	9.37	7.07	8	9.65	7.21
	9	9.90	8.72	9	9.36	8.30	9	9.74	8.55
	10	10.48	9.33	10	10.42	9.28	10	10.28	9.40
	11	10.81	10.44	11	10.67	10.52	11	9.34	8.69

Table 2: pH values of purged sulfate solutions mixed with mZVI

$CaSO_4$				$MgSO_4$			Ca-$MgSO_4$		
				PERIOD (DAYS)					
	0	**0.25**	**30**	**0**	**0.25**	**30**	**0**	**0.25**	**30**
pH	2	5.39	5.61	2	7.11	6.18	2	5.57	6.43
	3	5.66	5.95	3	7.03	6.22	3	5.81	6.54
	4	8.56	7.76	4	7.14	6.18	4	7.01	6.32
	5	9.16	7.92	5	8.07	6.28	5	8.21	6.44
	6	9.32	8.09	6	8.13	6.74	6	8.41	6.86
	7	9	8.3	7	8.4	6.3	7	8.53	6.34
	8	9.29	8.42	8	9.21	7.14	8	9.32	7.14
	9	9.68	8.68	9	9.48	8.25	9	9.67	8.47
	10	10.27	9.31	10	10.43	9.32	10	10.27	9.27
	11	10.71	10.44	11	10.67	10.52	11	10.54	10.65

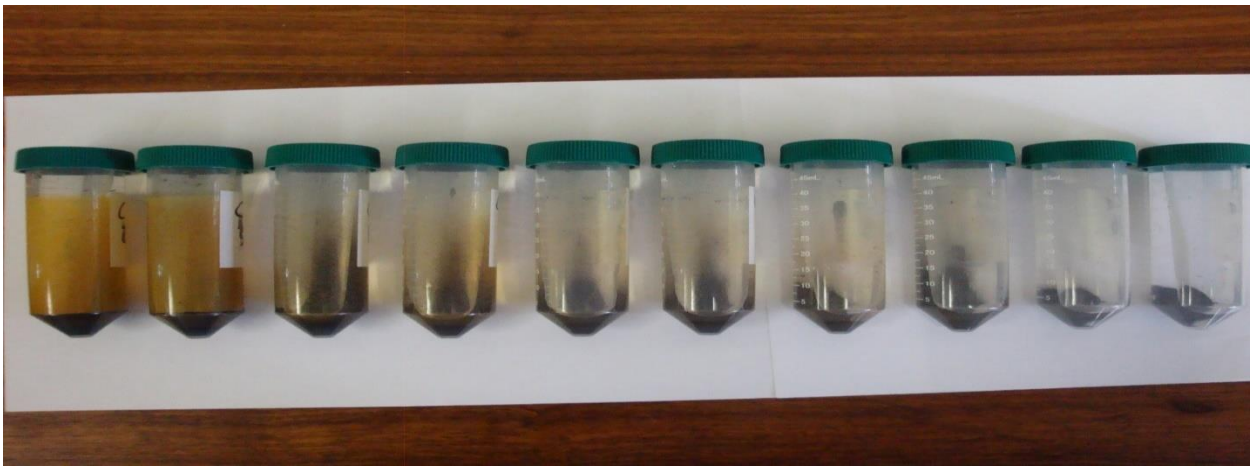

a

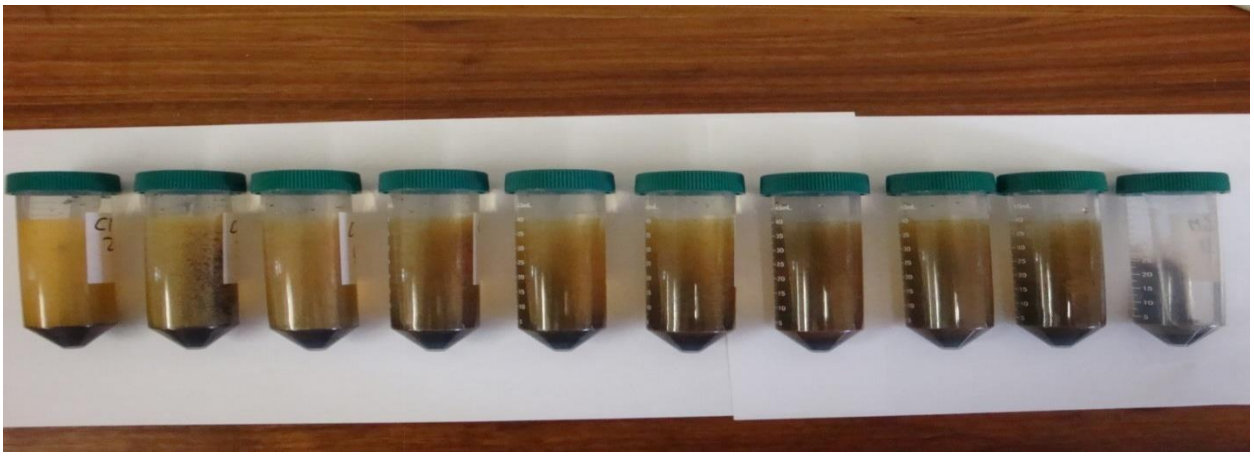

b

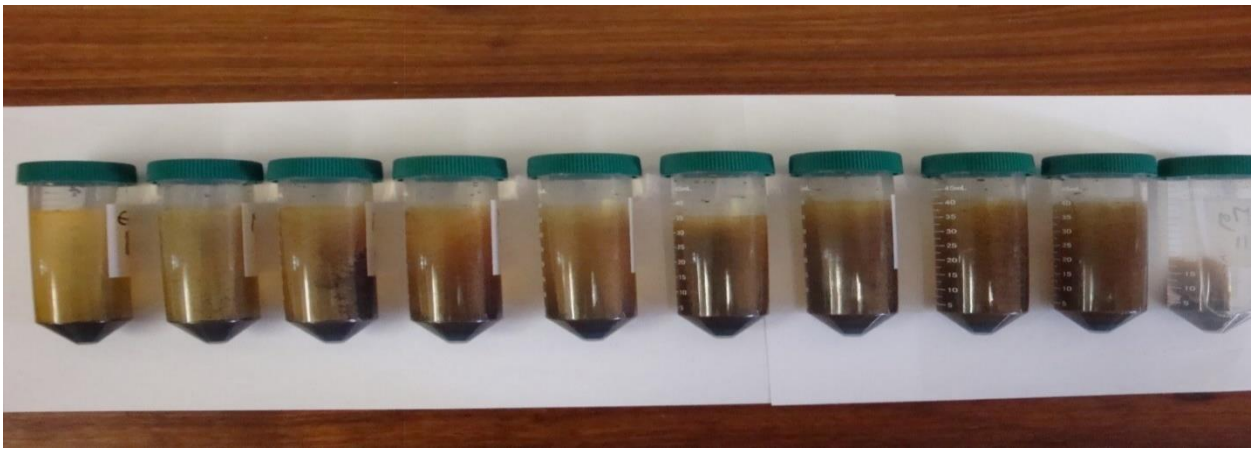

c

Figure 4: The effect of mZVI in a pH range of 2 to 11 (left to right) for (a) $CaSO_4$, (b) $MgSO_4$ and (c) Ca-MgSO4 after 30 days

Table 3: Residual DO concentrations of all sulfate solutions & FeDW with means and standard deviations

DO																							
																						32	
	Ca sulfate			CTRL						6 hours							16						
		4		mg/l	Mean	Std.Dev.	mmol/l	Mean	Std. Dev.	mg/l	Mean	Std.Dev.	mmol/l	Mean	Std. Dev.		mg/l	Mean	Std.Dev.	mmol/l	Mean	Std. Dev.
		Oxic		4.1			0.1281			0.6			0.0188				0.5			0.0156		
				4.2	4.1333	0.0577	0.1313	0.1292	0.0018	0.3	0.4000	0.1732	0.0094	0.0125	0.0054		0.4	0.3667	0.1528	0.0125	0.0115	0.0048
				4.1			0.1281			0.3			0.0094				0.2			0.0063		
		Anoxic		0.8			0.0250			0.3			0.0094				0.2			0.0063		
				0.5	0.6000	0.1732	0.0156	0.0188	0.0054	0.3	0.3333	0.0577	0.0094	0.0104	0.0018		0.3	0.3000	0.1000	0.0094	0.0094	0.0031
				0.5			0.0156			0.4			0.0125				0.4			0.0125		
		8																					
		Oxic		4.2			0.1313			0.3			0.0094				0.6			0.0188		
				4.3	4.2000	0.1000	0.1344	0.1313	0.0031	0.8	0.5000	0.2646	0.0250	0.0156	0.0083		0.2	0.3667	0.2082	0.0063	0.0115	0.0065
				4.1			0.1281			0.4			0.0125				0.3			0.0094		
		Anoxic		0.6			0.0188			0.8			0.0250				0.7			0.0219		
				0.4	0.4333	0.1528	0.0125	0.0135	0.0048	0.3	0.4333	0.3215	0.0094	0.0135	0.0100		0.5	0.5667	0.1155	0.0156	0.0177	0.0036
				0.3			0.0094			0.2			0.0063				0.5			0.0156		
	Mg sulfate																						
		4																					
		Oxic		4.1			0.1281			0.3			0.0094				0.3			0.0094		
				3.8	4.0667	0.1528	0.1219	0.1271	0.0048	0.5	0.4000	0.1000	0.0156	0.0125	0.0031		0.4	0.3000	0.1000	0.0125	0.0094	0.0031
				4.2			0.1313			0.4			0.0125				0.2			0.0063		
		Anoxic		0.5			0.0156			0.2			0.0063				0.5			0.0156		
				0.4	0.5333	0.1528	0.0125	0.0167	0.0048	0.3	0.2667	0.0577	0.0094	0.0083	0.0018		0.2	0.3000	0.1732	0.0063	0.0094	0.0054
				0.7			0.0219			0.3			0.0094				0.2			0.0063		
		8																					
		Oxic		4.2			0.1313			0.2			0.0063				0.3			0.0094		
				4.5	4.3000	0.1732	0.1406	0.1344	0.0054	0.3	0.3000	0.1000	0.0094	0.0094	0.0031		0.4	0.5000	0.2646	0.0125	0.0156	0.0083
				4.2			0.1313			0.4			0.0125				0.8			0.0250		
		Anoxic		0.6			0.0188			0.3			0.0094				0.3			0.0094		
				0.3	0.4333	0.1528	0.0094	0.0135	0.0048	0.3	0.4000	0.1732	0.0094	0.0125	0.0054		0.3	0.4000	0.1732	0.0094	0.0125	0.0054
				0.4			0.0125			0.6			0.0188				0.6			0.0188		
	Ca-Mg sulfate																						
		4																					
		Oxic		4.2			0.1313			0.8			0.0250				0.8			0.0250		
				4.3	4.2333	0.0577	0.1344	0.1323	0.0018	0.3	0.5000	0.2646	0.0094	0.0156	0.0083		0.2	0.4667	0.3055	0.0063	0.0146	0.0095
				4.2			0.1313			0.4			0.0125				0.4			0.0125		
		Anoxic		0.8			0.0250			0.4			0.0125				0.3			0.0094		
				0.4	0.5000	0.2646	0.0125	0.0156	0.0083	0.3	0.3667	0.0577	0.0094	0.0115	0.0018		0.5	0.3667	0.1155	0.0156	0.0115	0.0036
				0.3			0.0094			0.4			0.0125				0.3			0.0094		
		8																					
		Oxic		4.1			0.1281			0.3			0.0094				0.2			0.0063		
				4.3	4.2000	0.1000	0.1344	0.1313	0.0031	0.2	0.3667	0.2082	0.0063	0.0115	0.0065		0.3	0.4000	0.2646	0.0094	0.0125	0.0083
				4.2			0.1313			0.6			0.0188				0.7			0.0219		
		Anoxic		0.3			0.0094			0.3			0.0094				0.4			0.0125		
				0.8	0.5000	0.2646	0.0250	0.0156	0.0083	0.4	0.4333	0.1528	0.0125	0.0135	0.0048		0.3	0.3000	0.1000	0.0094	0.0094	0.0031
				0.4			0.0125			0.6			0.0188				0.2			0.0063		
	FeDW																						
		4		6.3			0.1969			0.4			0.0125				0.4			0.0125		
		Oxic		6.3	6.3667	0.1155	0.1969	0.1990	0.0036	0.2	0.3667	0.1528	0.0063	0.0115	0.0048		0.4	0.5333	0.2309	0.0125	0.0167	0.0072
				6.5			0.2031			0.5			0.0156				0.8			0.0250		
		Anoxic		0.4			0.0125			0.8			0.0250				0.3			0.0094		
				0.3	0.4667	0.2082	0.0094	0.0146	0.0065	0.3	0.5000	0.2646	0.0094	0.0156	0.0083		0.3	0.2667	0.0577	0.0094	0.0083	0.0018
				0.7			0.0219			0.4			0.0125				0.2			0.0063		
		8		6.5			0.2031			0.4			0.0125				0.3			0.0094		
		Oxic		6.4	6.4333	0.0577	0.2000	0.2010	0.0018	0.5	0.4000	0.1000	0.0156	0.0125	0.0031		0.5	0.5333	0.2517	0.0156	0.0167	0.0079
				6.4			0.2000			0.3			0.0094				0.8			0.0250		
		Anoxic		0.5			0.0156			0.3			0.0094				0.5			0.0156		
				0.4	0.5000	0.1000	0.0125	0.0156	0.0031	0.5	0.3667	0.1155	0.0156	0.0115	0.0036		0.4	0.3667	0.1528	0.0125	0.0115	0.0048
				0.6			0.0188			0.3			0.0094				0.2			0.0063		

APPENDIX C: SUPPLEMENTARY DATA FOR CHAPTER 5

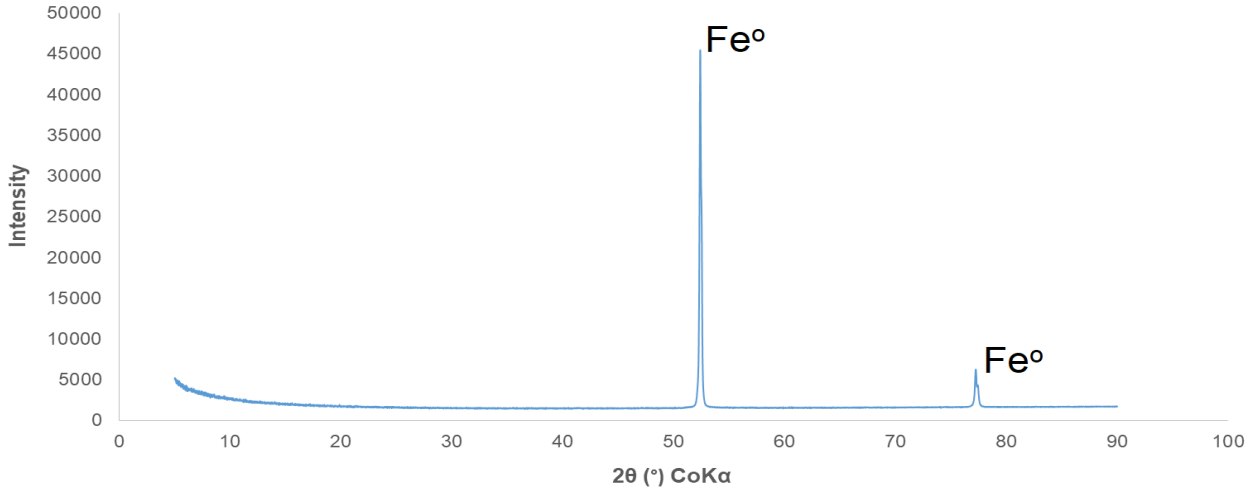

Figure C.1 Diffractogram of mZVI powder, of de-ionized water after 20 minutes

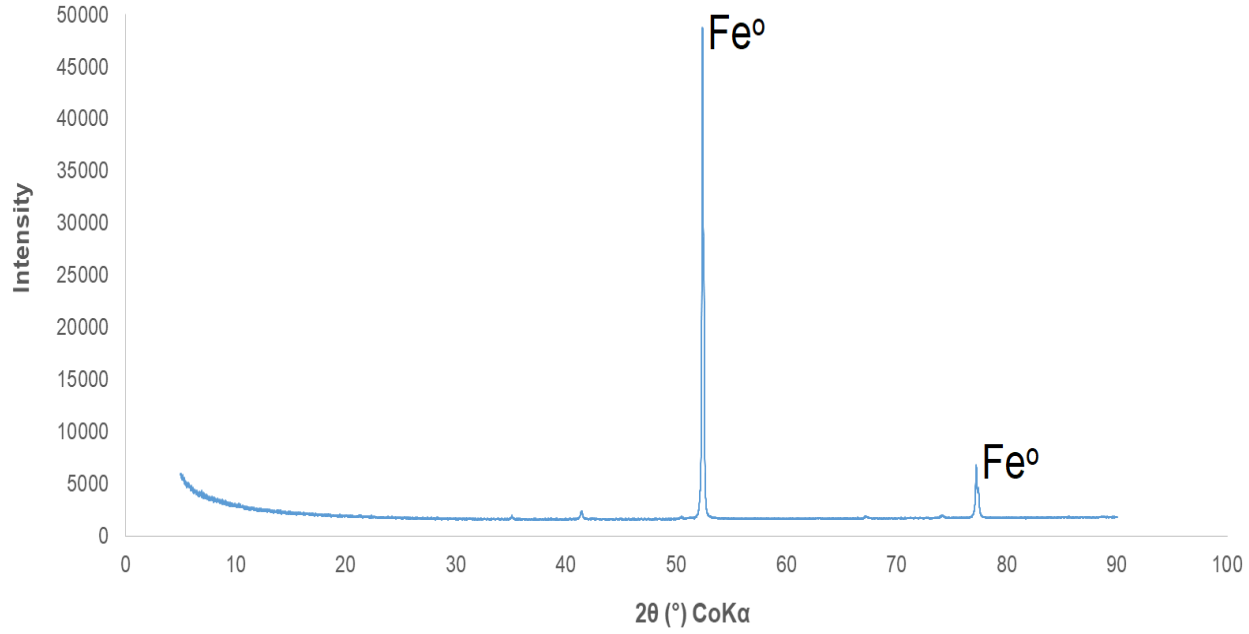

Figure C.2 Diffractogram of mZVI powder, of de-ionized water after 145 days

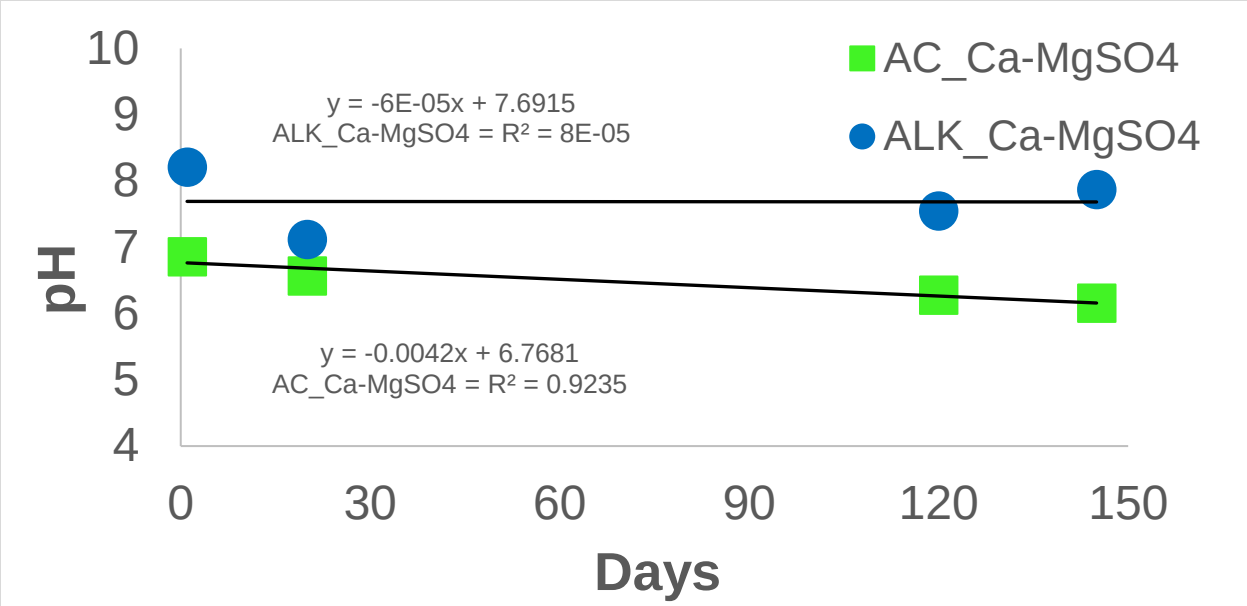

Figure C3: Correlation between pH and experimental days for the AC_Ca-$MgSO_4$ solution and AC_Ca-$MgSO_4$

Table 1: The GLM procedure, t Tests (LSD) of S concentrations.

ac_$CaSO_4$	
Alpha	0.05
Error Degrees of Freedom	10
Error Mean Square	0.0002
Critical Value of t	2.22814
Least Significant Difference	0.0257
alk_$CaSO_4$	
Alpha	0.05
Error Degrees of Freedom	10
Error Mean Square	0.000143
Critical Value of t	2.22814
Least Significant Difference	0.0218
AC_$CaSO_4$	
Alpha	0.05
Error Degrees of Freedom	10
Error Mean Square	0.000451
Critical Value of t	2.22814
Least Significant Difference	0.0386
ALK_$CaSO_4$	
Alpha	0.05
Error Degrees of Freedom	10
Error Mean Square	0.000204
Critical Value of t	2.22814
Least Significant Difference	0.026
ac_$MgSO_4$	
Alpha	0.05
Error Degrees of Freedom	10

Error Mean Square	0.000102
Critical Value of t	2.22814
Least Significant Difference	0.0184
alk_MaSO$_4$	
Alpha	0.05
Error Degrees of Freedom	10
Error Mean Square	0.000019
Critical Value of t	2.22814
Least Significant Difference	0.0079
AC_MgSO$_4$	
Alpha	0.05
Error Degrees of Freedom	10
Error Mean Square	0.000126
Critical Value of t	2.22814
Least Significant Difference	0.0204
ALK_MgSO$_4$	
Alpha	0.05
Error Degrees of Freedom	10
Error Mean Square	0.000427
Critical Value of t	2.22814
Least Significant Difference	0.0376
AC_Ca-MgSO$_4$	
Alpha	0.05
Error Degrees of Freedom	10
Error Mean Square	0.000076
Critical Value of t	2.22814
Least Significant Difference	0.0159
ALK_Ca-MgSO$_4$	
Alpha	0.05
Error Degrees of Freedom	10
Error Mean Square	0.000452
Critical Value of t	2.22814
Least Significant Difference	0.0387

Table 2: The GLM procedure, t Tests (LSD) for Ca, Mg & Ca-Mg concentrations

ac_CaSO$_4$	
Alpha	0.05
Error Degrees of Freedom	10
Error Mean Square	0.000107
Critical Value of t	2.22814
Least Significant Difference	0.0188
alk_CaSO$_4$	
Alpha	0.05
Error Degrees of Freedom	10
Error Mean Square	0.000213
Critical Value of t	2.22814
Least Significant Difference	0.0266
AC_CaSO$_4$	
Alpha	0.05
Error Degrees of Freedom	10
Error Mean Square	0.00018

Critical Value of t	2.22814
Least Significant Difference	0.0244
ALK_$CaSO_4$	
Alpha	0.05
Error Degrees of Freedom	10
Error Mean Square	0.000463
Critical Value of t	2.22814
Least Significant Difference	0.0391
ac_$MgSO_4$	
Alpha	0.05
Error Degrees of Freedom	10
Error Mean Square	4.617E-6
Critical Value of t	2.22814
Least Significant Difference	0.0039
alk_$MaSO_4$	
Alpha	0.05
Error Degrees of Freedom	10
Error Mean Square	0.000081
Critical Value of t	2.22814
Least Significant Difference	0.0163
AC_$MgSO_4$	
Alpha	0.05
Error Degrees of Freedom	10
Error Mean Square	0.000581
Critical Value of t	2.22814
Least Significant Difference	0.0439
ALK_$MgSO_4$	
Alpha	0.05
Error Degrees of Freedom	10
Error Mean Square	0.000435
Critical Value of t	2.22814
Least Significant Difference	0.0379
AC_Ca-$MgSO_4$	
Alpha	0.05
Error Degrees of Freedom	10
Error Mean Square	0.000068
Critical Value of t	2.22814
Least Significant Difference	0.015
ALK_Ca-$MgSO_4$	
Alpha	0.05
Error Degrees of Freedom	10
Error Mean Square	3.288E-6
Critical Value of t	2.22814
Least Significant Difference	0.0033

APPENDIX D: DATA FROM PHREEQCi FOR CHAPTER 5

Table D.1: Calculated mineral phases in equilibrium with the $CaSO_4$ solutions (3.12 *mM*)

	Saturation Index (SI)							
Day	**1**		**20**		**120**		**145**	
	ac	**alk**	**ac**	**alk**	**ac**	**alk**	**ac**	**alk**
Anhydrite	-1.6	-1.6	-1.6	-1.63	-1.61	-1.64	-1.62	-1.64
$Fe_2(OH)_2$	-5.10	-1.21	-4.6	-2.73	-3.36	-2.03	-3.22	-2.11
$Fe_2(SO_4)_3$	-37.7	-47.4	-38.7	-42.5	-41.6	-44.9	-41.3	-45.1
$Fe_3(OH)_8$	-0.36	4.20	0.66	2.69	2.79	2.96	3.62	2.49
Ferrihydrite	2.51	2.84	2.77	2.85	3.22	2.63	3.56	2.44
Goethite	5.21	5.54	5.47	5.55	5.92	5.33	6.26	5.14
Gypsum	-1.35	-1.36	-1.35	-1.38	-1.36	-1.39	-1.37	-1.39
H-Jarosite	-6.04	-11.9	-6.26	-8.64	-7.41	-10.7	-6.68	-11.04
Hematite	12.8	13.5	13.3	13.5	14.2	13.1	14.9	12.7
Lepidocrocite	4.33	4.66	4.59	4.67	5.04	4.45	5.38	4.26
Lime	21.0	-17.6	-20.5	-19.3	-19.3	-18.6	-19.2	-18.7
Maghemite	5.01	5.67	5.53	5.69	6.43	5.27	7.12	4.88
Magnetite	16.5	21.0	17.4	19.5	19.6	19.8	20.4	19.3
Melanterite	-6.9	-6.49	-6.95	-6.39	-6.96	-6.37	-6.97	-6.36
$O_{2(g)}$	-80.9	-68.9	-79.7	-71.9	-67.6	-68.1	-66.2	-67.3
Portlandite	-11.2	-7.7	-10.7	-9.36	-9.41	-8.69	-9.27	-8.79
Pyrite								
Schwertmannite	7.40	4.54	8.69	7.22	10.3	4.43	12.8	3.02

Table D.2: Calculated mineral phases in equilibrium with the $CaSO_4$ solutions (12.5 *mM*)

	Saturation Index (SI)							
Day	**1**		**20**		**120**		**145**	
	AC	**ALK**	**AC**	**ALK**	**AC**	**ALK**	**AC**	**ALK**
Anhydrite	-0.77	-0.78	-0.77	-0.78	-0.81	-0.78	-0.77	-0.78
$Fe_2(OH)_2$	-4.34	-1.07	-3.8	-2.55	-2.4	-1.69	-2.35	-1.77
$Fe_2(SO_4)_3$	-34.2	-44.5	-35.2	-40.4	-38.8	-42.7	-39.1	-43.2
$Fe_3(OH)_8$	2.47	5.98	3.29	3.95	5.52	5.03	5.54	4.09
Ferrihydrite	3.54	3.66	3.68	3.39	4.10	3.5	4.08	3.07
Goethite	6.24	6.36	6.38	6.09	6.80	6.2	6.78	5.77
Gypsum	-0.52	-0.53	-0.52	-0.53	-0.56	-0.53	-0.52	-0.53

H-Jarosite	-1.97	-8.61	-2.61	-6.36	-4.09	-7.71	-4.3	-8.76
Hematite	14.8	15.1	15.2	14.6	15.9	14.8	15.9	13.9
Lepidocrocite	5.36	5.48	5.5	5.21	5.92	5.32	5.9	4.89
Lime	-20.7	-17.2	-20.2	-18.7	-18.8	-17.9	-18.7	-18
Maghemite	7.08	7.31	7.36	6.77	8.19	7	8.16	6.13
Magnetite	19.3	22.8	20.1	20.8	22.3	21.9	22.4	20.9
Melanterite	-5.7	-5.92	-5.7	-5.87	-5.65	-5.86	-5.69	-5.82
$O_{2(g)}$	-82.1	-69.4	-79.8	-71.8	-72.9	-70	-73.3	-71.9
Portlandite	-10.8	-7.31	-10.3	-8.84	-8.94	-8	-8.83	-8.13
Pyrite								
Schwertmannite	16.5	11.8	16.7	12.1	17.9	11.6	17.6	8.36

Table D.3: Calculated mineral phases in equilibrium with the $MgSO_4$ solutions (3.12 *mM*)

	Saturation Index (SI)							
Day	**1**		**20**		**120**		**145**	
	ac	**alk**	**ac**	**alk**	**ac**	**alk**	**ac**	**alk**
Brucite	-5.83	-3.77	-6.52	-5.48	-5.77	-5.16	-5.53	-5.1
Epsomite	-3.81	-3.81	-3.82	-3.81	-3.82	-3.82	-3.83	-3.82
$Fe_2(OH)_2$	-4.75	-2.83	-5.43	-4.51	-4.36	-4	-4.09	-3.8
$Fe_2(SO_4)_3$	-33.2	-38.4	-31.8	-34.6	-33.8	-35.6	-34.2	-37
$Fe_3(OH)_8$	2.55	-5.45	1.21	2.46	2.57	2.88	3.1	1.85
Ferrihydrite	3.78	4.27	3.46	3.62	3.6	3.58	3.73	2.96
Goethite	6.48	6.97	6.16	6.32	6.3	6.28	6.43	5.66
H-Jarosite	-0.88	-3.52	-0.5	-2.07	-1.58	-2.84	-1.68	-4.81
Hematite	15.4	16.4	14.7	15	15	15	15.3	13.7
Lepidocrocite	5.6	6.09	5.28	5.44	5.42	5.4	5.55	4.78
Maghemite	7.57	8.54	6.91	7.24	7.2	7.15	7.46	5.92
Magnesioferrite	8.11	11.1	6.76	8.13	7.8	8.36	8.3	7.18
Magnetite	19.4	22.3	18	19.3	19.4	19.7	19.9	18.7
Melanterite	-5.93	-6.06	-5.93	-6.04	-5.61	-5.85	-5.59	-5.71
Mg(OH)(active)	-7.78	-5.72	-8.47	-7.43	-7.72	-7.11	-7.48	-7.05
$O_{2(g)}$	-77.2	-74.8	-78.6	-77.6	-77.4	-77.5	-78.4	-78.7
Periclase	-10.6	-8.51	-11.3	-10.2	-10.5	-9.9	-10.3	-9.84
Pyrite								
Schwertmannite	18.7	19.3	17.1	16.8	17.1	16	17.7	10.9

Table D.4: Calculated mineral phases in equilibrium with the $MgSO_4$ solutions (12.5 *mM*)

Saturation Index (SI)								
Day	**1**		**20**		**120**		**145**	
	AC	**ALK**	**AC**	**ALK**	**AC**	**ALK**	**AC**	**ALK**
Brucite	-5.52	-3.67	-4.3	-2.87	-5.58	-4.83	-5.29	-4.77
Epsomite	-2.97	-2.97	-2.97	-2.96	-2.97	-2.96	-2.98	-2.97
$Fe_2(OH)_2$	-4.33	-2.42	-3.12	-1.63	-4.25	-3.49	-3.87	-3.31
$Fe_2(SO_4)_3$	-32.3	-35.4	-34.9	-37.4	-31.7	-32.8	-35	-34.1
$Fe_3(OH)_8$	2.23	6.58	4.53	7.78	2.75	4.66	0.73	3.66
Ferrihydrite	3.42	4.64	3.96	4.84	3.64	4.21	2.44	3.62
Goethite	6.12	7.34	6.66	7.54	6.34	6.91	5.14	6.32
H-Jarosite	-0.9	-0.93	-1.71	-1.91	-0.14	0.1	-4.33	-1.79
Hematite	14.6	17.1	15.7	17.5	15.1	16.2	12.7	15
Lepidocrocite	5.24	6.46	5.78	6.66	5.46	6.03	4.26	5.44
Maghemite	6.84	9.27	7.92	9.68	7.27	8.42	4.87	7.24
Magnesioferrite	7.69	12	9.99	13.2	8.06	9.95	5.96	8.84
Magnetite	19.1	23.4	21.3	24.6	19.6	21.5	17.6	20.5
Melanterite	-4.98	-4.91	-4.98	-4.91	-4.84	-4.81	-4.76	-4.7
Mg(OH)(active)	-7.47	-5.62	-6.25	-4.82	-7.53	-6.78	-7.24	-6.72
$O_{2(g)}$	-76.2	-74.9	-79.8	-76.9	-78.5	-79.5	-79	-80.9
Periclase	-10.3	-8.41	-9.04	-7.61	-10.3	-9.57	-10	-9.51
Pyrite								
Schwertmannite	16.6	23.4	19	23.8	18.4	21.9	8.38	17

Table D.5: Calculated mineral phases in equilibrium with the Ca-$MgSO_4$ solutions (12.5 *mM*)

Saturation Index (SI)								
Day	**1**		**20**		**120**		**145**	
	AC	**ALK**	**AC**	**ALK**	**AC**	**ALK**	**AC**	**ALK**
Anhydrite	-1.06	-1.05	-1.06	-1.05	-1.06	-1.05	-1.07	-1.05
Brucite	-5.66	-2.94	-6.24	-5.13	-6.83	-4.27	-7 .08	-3.64
Epsomite	-3.82	-3.27	-3.28	-3.27	-3.28	-3.27	-3.3	-3.27
$Fe(OH)_2$	-3.74	-1.61	-4.31	-3.79	-4.84	-2.89	-5.06	-2.2
$Fe_2(SO_4)_3$	-32.2	-39	-30.7	-33.3	-30	-35.3	-29.9	-37.1
$Fe_3(OH)_8$	3.43	6.95	2.62	3.86	1	5.39	0.21	6.16
Ferrihydrite	3.72	4.42	3.6	3.96	3.06	4.28	2.77	4.32
Goethite	6.42	7.12	6.3	6.66	5.76	6.98	5.47	7.02

Gypsum	-0.81	-0.8	-0.81	-0.8	-0.81	-0.8	-0.82	-0.8
H-Jarosite	-0.35	-3.68	0.46	-0.67	-0.01	-1.45	-0.39	-2.58
Hematite	15.2	16.6	15	15.7	13.9	16.4	13.4	16.4
Lepidocrocite	5.54	6.24	5.42	5.78	4.88	6.1	4.59	6.14
Lime	-21.5	-18.8	-22.1	-21	-22.7	-20.2	-22.9	-19.5
Maghemite	7.44	8.83	7.2	7.91	6.11	8.55	5.54	8.63
Magnesioferrite	8.15	12.3	7.33	9.15	5.65	10.7	4.84	11.4
Magnetite	20.3	23.8	19.4	20.7	17.8	22.2	17	23
Melanterite	-4.55	-5.14	-4.55	-5.12	-4.5	-5.09	-4.48	-5.03
Mg(OH)(active)	-7.61	-4.89	-8.19	-7.08	-8.78	-6.22	-9.03	-5.59
$O_{2(g)}$	-70.9	-71.6	-80.3	-79.2	-84.2	-78.2	-82.8	-80.5
Periclase	-10.4	-7.68	-11	-9.87	-11.6	-9.01	-11.8	-8.38
Portlandite	-11.6	-8.91	-12.2	-11.1	-12.8	-10.2	-13.4	-9.61
Pyrite								
Schwertmannite	18.7	20	18.7	19.8	15.3	21	13.4	20.3

Table D.6: Data used in PHREEQCi for the 3.12 *mM* $CaSO_4$ solution. (Input of other solutions's data followed the same procedure)

```
TITLE ac_CaSO4
SOLUTION 1 ac_CaSO4
            units       ppm
            pH          8.123
            redox       pe
            pe          -3.91149971
            density     1.023
            temp        25
            Ca          123.480
            S(6)        299.7914767
            Fe(2)       0.1159
            Fe(3)       0.164621304
PHASES
      Anhydrite
            CaSO4 = Ca+2 + SO4-2
            log_k -4.36
      Fe(OH)2
            Fe(OH)2 + 2H+ = Fe+2 + 2H2O
            log_k 13.564
```

```
Fe2(SO4)3
      Fe2(SO4)3 = 2Fe+3 + 3SO4-2
      log_k -3.7343
Fe3(OH)8
      Fe3(OH)8 + 8H+ = 2Fe+3 + Fe+2 + 8H2O
      log_k 20.222
Ferrihydrite
      Fe(OH)3 + 3H+ = Fe+3 + 3H2O
      log_k 3.191
Goethite
      FeOOH + 3H+ = Fe+3 + 2H2O
      log_k 0.491
Gypsum
      CaSO4:2H2O = Ca+2 + SO4-2 + 2H2O
      log_k -4.61
H-Jarosite
      (H3O)Fe3(SO4)2(OH)6 + 5H+ = 3Fe+3 + 2SO4-2 + 7H2O
      log_k -12.1
Hematite
      Fe2O3 + 6H+ = 2Fe+3 + 3H2O
      log_k -1.418
Lepidocrocite
      FeOOH + 3H+ = Fe+3 + 2H2O
      log_k 1.371
Lime
      CaO + 2H+ = Ca+2 + H2O
      log_k 32.6993
Maghemite
      Fe2O3 + 6H+ = 2Fe+3 + 3H2O
      log_k 6.386
Magnetite
      Fe3O4 + 8H+ = 2Fe+3 + Fe+2 + 4H2O
      log_k 3.4028
Melanterite
      FeSO4:7H2O = Fe+2 + SO4-2 + 7H2O
      log_k -2.209
Portlandite
      Ca(OH)2 + 2H+ = Ca+2 + 2H2O
```

```
            log_k 22.804
      Schwertmannite
            Fe8O8(OH)4.8(SO4)1.6 + 20.8H+ = 8Fe+3 + 12.8H2O + 1.6SO4-2
            log_k 10
USE Solution 1
EQUILIBRIUM_PHASES 1
      Anhydrite         0.0   0.0
      Fe(OH)2           0.0   0.0
      Fe2(SO4)3         0.0   0.0
      Fe3(OH)8          0.0   0.0
      Ferrihydrite      0.0   0.0
      Goethite          0.0   0.0
      Gypsum            0.0   0.0
      H-Jarosite        0.0   0.0
      Hematite          0.0   0.0
      Lepidocrocite     0.0   0.0
      Lime              0.0   0.0
      Maghemite         0.0   0.0
      Magnetite         0.0   0.0
      Melanterite       0.0   0.0
      Portlandite       0.0   0.0
      Schwertmannite    0.0   0.0
END

TITLE alk_CaSO4
SOLUTION 1 alk_CaSO4
            units       ppm
            pH          8.37
            pe          -4.431889292
            redox       pe
            density     1.023
            temp        20.6
            Ca          124.806
            S(6)        299.7914767
            Fe(2)       0.490
            Fe(3)       0.011
PHASES
      Anhydrite
```

```
      CaSO4 = Ca+2 + SO4-2
      log_k -4.36
Fe(OH)2
      Fe(OH)2 + 2H+ = Fe+2 + 2H2O
      log_k 13.564
Fe2(SO4)3
      Fe2(SO4)3 = 2Fe+3 + 3SO4-2
      log_k -3.7343
Fe3(OH)8
      Fe3(OH)8 + 8H+ = 2Fe+3 + Fe+2 + 8H2O
      log_k 20.222
Ferrihydrite
      Fe(OH)3 + 3H+ = Fe+3 + 3H2O
      log_k 3.191
Goethite
      FeOOH + 3H+ = Fe+3 + 2H2O
      log_k 0.491
Gypsum
      CaSO4:2H2O = Ca+2 + SO4-2 + 2H2O
      log_k -4.61
H-Jarosite
      (H3O)Fe3(SO4)2(OH)6 + 5H+ = 3Fe+3 + 2SO4-2 + 7H2O
      log_k -12.1
Hematite
      Fe2O3 + 6H+ = 2Fe+3 + 3H2O
      log_k -1.418
Lepidocrocite
      FeOOH + 3H+ = Fe+3 + 2H2O
      log_k 1.371
Lime
      CaO + 2H+ = Ca+2 + H2O
      log_k 32.6993
Maghemite
      Fe2O3 + 6H+ = 2Fe+3 + 3H2O
      log_k 6.386
Magnetite
      Fe3O4 + 8H+ = 2Fe+3 + Fe+2 + 4H2O
      log_k 3.4028
```

```
      Melanterite
            FeSO4:7H2O = Fe+2 + SO4-2 + 7H2O
            log_k -2.209
      Portlandite
            Ca(OH)2 + 2H+ = Ca+2 + 2H2O
            log_k 22.804
      Schwertmannite
            Fe8O8(OH)4.8(SO4)1.6 + 20.8H+ = 8Fe+3 + 12.8H2O + 1.6SO4-2
            log_k 10
USE Solution 1
EQUILIBRIUM_PHASES 1
      Anhydrite         0.0   0.0
      Fe(OH)2           0.0   0.0
      Fe2(SO4)3         0.0   0.0
      Fe3(OH)8          0.0   0.0
      Ferrihydrite      0.0   0.0
      Goethite          0.0   0.0
      Gypsum            0.0   0.0
      H-Jarosite        0.0   0.0
      Hematite          0.0   0.0
      Lepidocrocite     0.0   0.0
      Lime              0.0   0.0
      Maghemite         0.0   0.0
      Magnetite         0.0   0.0
      Melanterite       0.0   0.0
      Portlandite       0.0   0.0
      Schwertmannite    0.0   0.0
END
```